Intrinsic and extrinsic spin-orbit torques from first principles

Guillaume Géranton

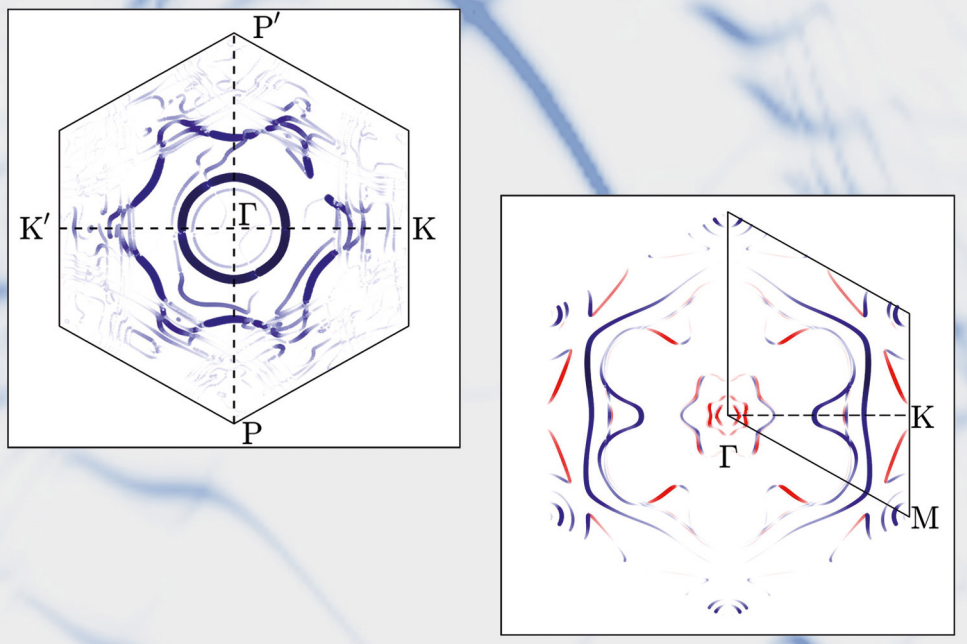

Member of the Helmholtz Association

Schlüsseltechnologien / Key Technologies
Band / Volume 141
ISBN 978-3-95806-213-9

JÜLICH FORSCHUNGSZENTRUM

Schriften des Forschungszentrums Jülich
Reihe Schlüsseltechnologien / Key Technologies Band / Volume 141

Forschungszentrum Jülich GmbH
Peter Grünberg Institute (PGI)
Quantum Theory of Materials (PGI-1 / IAS-1)

Intrinsic and extrinsic spin-orbit torques from first principles

Guillaume Géranton

Schriften des Forschungszentrums Jülich
Reihe Schlüsseltechnologien / Key Technologies Band / Volume 141

ISSN 1866-1807 ISBN 978-3-95806-213-9

Bibliographic information published by the Deutsche Nationalbibliothek.
The Deutsche Nationalbibliothek lists this publication in the Deutsche Nationalbibliografie; detailed bibliographic data are available in the Internet at http://dnb.d-nb.de.

Publisher and Distributor: Forschungszentrum Jülich GmbH
Zentralbibliothek
52425 Jülich
Tel: +49 2461 61-5368
Fax: +49 2461 61-6103
Email: zb-publikation@fz-juelich.de
www.fz-juelich.de/zb

Cover Design: Grafische Medien, Forschungszentrum Jülich GmbH

Printer: Grafische Medien, Forschungszentrum Jülich GmbH

Copyright: Forschungszentrum Jülich 2017

Schriften des Forschungszentrums Jülich
Reihe Schlüsseltechnologien / Key Technologies, Band / Volume 141

D 82 (Diss. RWTH Aachen University, 2017)

ISSN 1866-1807
ISBN 978-3-95806-213-9

The complete volume is freely available on the Internet on the Jülicher Open Access Server (JuSER) at www.fz-juelich.de/zb/openaccess.

This is an Open Access publication distributed under the terms of the Creative Commons Attribution License 4.0, which permits unrestricted use, distribution, and reproduction in any medium, provided the original work is properly cited.

À mes parents

Abstract

This thesis attempts to shed light on the microscopic mechanisms underlying the current-induced magnetic torques in ferromagnetic heterostructures. We have developed first principles methods aiming at the accurate and efficient calculation of the so-called spin-orbit torques (SOTs) in magnetic thin films. The emphasis of this work is on the impurity-driven extrinsic SOTs.

The main part of this thesis is dedicated to the development of a formalism for the calculation of the SOTs within the Korringa-Kohn-Rostoker (KKR) method. The impurity-induced transitions rates are obtained from first principles and their effect on transport properties is treated within the Boltzmann formalism. The developed formalism provides a mean to compute the SOTs beyond the conventional constant relaxation time approximation.

We first apply our formalism to the investigation of FePt/Pt and Co/Cu bilayers in the presence of defects and impurities. Our results hint at a crucial dependence of the torque on the type of disorder present in the films, which we explain by a complex interplay of several competing Fermi surface contributions to the SOT. Astonishingly, specific defect distributions or doping elements lead respectively to an increase or a sign change of the torque, which can not be explained on the basis of simple models. We also compute the intrinsic SOT induced by electrical and thermal currents within the full potential linearized augmented plane-wave method.

Motivated by recent experimental works, we then investigate the microscopic origin of the SOT in a Ag_2Bi-terminated Ag film grown on ferromagnetic Fe(110). We find that the torque in that system can not be explained solely by the spin-orbit coupling in the Ag_2Bi alloy, and instead results from the spin-orbit coupling in all regions of the film.

Finally, we predict a large SOT in Fe/Ge bilayers and suggest that semiconductor substrates might be a promising alternative to heavy metals for the development of SOT-based magnetic random access memories. We show the strong dependence of the SOT on the stacking direction, thereby providing important guidelines for future experimental works. We also compute the sublattice-resolved SOTs in an antiferromagnetic Fe/Ge thin film and find a large anisotropy of the torkance tensor.

Notations and Abbreviations

In this thesis, we use the following notations:

Not.	Meaning	Not.	Meaning
μ_B	Bohr magneton	e	positive elementary charge
a_0	Bohr radius	$\boldsymbol{e}_i$	unit vector in i direction
ε_0	permittivity of free space		

The following abbreviations are used:

Abbr.	Meaning	Abbr.	Meaning
2DEG	two-dimensional electron gas	LLG	Landau-Lifshitz-Gilbert
ASA	atomic sphere approximation	MLWF	maximally localized Wannier function
bcc	body-centered cubic		
BZ	Brillouin zone	SHC	spin Hall conductivity
CPU	central processing unit	SHE	spin Hall effect
DFT	density functional theory	SNE	spin Nernst effect
DOS	density of states	SOC	spin-orbit coupling
fcc	face-centered cubic	SOI	spin-orbit interaction
FLAPW	full potential linearized augmented plane-wave (method)	SOT	spin-orbit torque
		SRA	scalar-relativistic approximation
FS	Fermi surface		
GGA	generalized gradient approximation	STT	spin-transfer torque
IBZ	irreducible part of the BZ	T-SOT	thermal spin-orbit torque
KKR	Korringa-Kohn-Rostoker	VWN	Vosko-Wilk-Nusair
LDA	local density approzimation	XC	exchange-correlation

Contents

1. Introduction **11**

2. Spin-orbit torques **15**
2.1. Phenomenology of SOTs . . . 15
2.2. Discussion of the mechanisms . . . 17
2.2.1. Spin Hall effect . . . 17
2.2.2. Interfacial spin-orbit torques . . . 19
2.3. Kubo formalism . . . 21
2.4. Thermal spin-orbit torques . . . 24

3. SOTs in the FLAPW method **27**
3.1. Density Functional Theory (DFT) . . . 27
3.1.1. The many body problem . . . 27
3.1.2. Hohenberg-Kohn theorem . . . 28
3.1.3. Kohn-Sham equation . . . 29
3.2. FLAPW method . . . 30
3.3. Wannier functions . . . 31
3.3.1. Definition . . . 32
3.3.2. Maximally localized Wannier functions . . . 33
3.3.3. Strategy for parallelization . . . 37
3.3.4. Wannier interpolation . . . 39
3.4. Kubo formalism . . . 41

4. Impurity-driven SOTs in the KKR method **43**
4.1. Green functions in physics . . . 43
4.2. KKR method . . . 44
4.2.1. Voronoi construction . . . 45
4.2.2. Single-site Green function . . . 46
4.2.3. Multiple scattering theory . . . 50
4.2.4. Generalization to multiple atoms in the unit cell . . . 54
4.2.5. Scattering off impurities . . . 55
4.3. KKR representation of operators . . . 57
4.3.1. Spin operator . . . 58
4.3.2. Torque operator . . . 58
4.3.3. Spin flux operator . . . 60
4.3.4. Relativistic velocity operator (α-matrix) . . . 60

4.4. Boltzmann formalism for the torque 62
4.4.1. Finite temperature 65

5. Results **67**
5.1. SOTs induced by electrical and thermal currents in $L1_0$-FePt/Pt films 67
5.1.1. Spin-orbit torques driven by electrical currents 67
5.1.2. Thermal spin-orbit torques 71
5.1.3. Impurity driven spin-orbit torques 73
5.2. Influence of doping by various impurities in Co/Cu films 83
5.3. Contributions from the Rashba effect to the SOT in Ag_2Bi/Ag/Fe . . 90
5.3.1. Electronic structure 90
5.3.2. Torkance at the true Fermi energy 94
5.3.3. Torkance at a shifted Fermi energy 95
5.4. SOTs in semiconductor-based thin films: example of Fe/Ge bilayers . 98
5.4.1. SOTs in ferromagnetic Fe/Ge(111) 98
5.4.2. SOTs in ferromagnetic Fe/Ge(001) 101
5.4.3. SOTs in antiferromagnetic Fe/Ge(111) 103

6. Conclusion **107**

A. Perspectives: Kubo formalism for the torque in KKR **109**

Bibliography **113**

List of Publications **119**

List of Figures **121**

1 Introduction

From the early age of information technologies there has been a constant dichotomy between volatile and non-volatile memories. On the one hand, storing the astronomic and ever growing amount of information generated by private users, companies and public administrations requires memory devices that are able to store data for an indefinitely long time. The market of this non-volatile type of memories has been historically dominated by magnetic memories generally called *hard disks*. On the other hand, the very fast processing of data allowed by modern computer processing units (CPUs) requires a correspondingly fast access to the stored information and short writing times. This need for high performances has led to the development of very efficient but volatile transistor-based memories known as static and dynamic *random-access memories* (SRAM and DRAM respectively).

The development of non-volatile magnetic random access memories (MRAMs) has brought a new paradigm in the field of information technologies. The fact that MRAMs are intrinsically non-volatile and never require a refresh drastically reduces power consumption as compared to SRAM and DRAM. With the development of electrically switchable MRAMs based on spin-transfer torques (STTs), STT-MRAMs might become a *universal memory* that combines non-volatility, high performance and high density. However, the very large writing current density flowing through the tunnel barrier of STT-MRAMs is currently limiting the performance and the reliability of this type of memories [1].

The recent discovery of spin-orbit torques (SOTs) provides an alternative writing scheme where the read and write paths can be fully decoupled. In the so-called SOT-MRAMs, the writing current is injected in the plane of the storage layer, which circumvents the problems due to the heating of the tunnel barrier in STT-MRAMs. This discovery paves the way to the development of a *universal memory*, which combines the advantages of non-volatile memories with the scalability and performance of SRAM and DRAM [2].

Spin-orbit torques are a class of magnetic torques that rely on the transfer of angular momentum from the crystal lattice to the magnetization [3–5]. They differ from the conventional spin-transfer torques in that they do not imply a transfer of spins

between two regions of different magnetization direction and they can be observed in any non-centrosymmetric magnetic system with sizeable spin-orbit interaction (SOI) [6, 7]. Spin-orbit torques have been intensively studied in the last years and it has been shown that they can lead to the reversal of the ferromagnetic magnetization without the help of an additional polarizing layer [8–10].

The microscopic origin of SOTs has been a matter of intense debate. However, the numerous experimental results that have been obtained over the last few years suggest that two mechanisms play a central role in giving rise to the SOTs in ferromagnetic/heavy metal bilayers. The first mechanism is the generation of a spin current in the heavy metal by the spin Hall effect (SHE) [11, 12] , which injects a net spin angular momentum into the ferromagnetic layer, where it ultimately gives rise to a torque on the magnetization [9, 10, 13]. The second mechanism arises from the SOI-induced spin polarization of the conduction electrons [4, 5, 13–15] at the interface between the ferromagnetic and the heavy metal layer, where magnetism, spin-orbit coupling and broken inversion symmetry coexist. While the magnitude of the SHE-induced SOT can be to some extent estimated from the value of the spin Hall conductivity of the substrate, the second contribution to the SOT has a pure interfacial character and can not be easily related to the bulk properties of the individual materials. The sensitivity of the SOT on the atomistic details of the interface makes the application of simple models such as the Rashba model very questionable.

The density functional theory (DFT) offers a systematic and accurate manner to compute the electronic properties of solids from first principles. The development of very efficient methods such as the full potential augmented plane-wave (FLAPW) and the Korringa-Kohn-Rostoker (KKR) methods, combined with state of the art high performance computing (HPC), has made possible the investigation of transport properties in large systems of many atoms in the unit cell. This thesis is dedicated to the development and the application of highly efficient first principles methods for the investigation of SOTs in ferromagnetic bilayers. We focus in particular on the importance of atomistic details such as layer thickness, disorder strength and scattering on impurities, which can not be accessed from model approaches.

A large part of this thesis is dedicated to the implementation of a formalism for the calculation of extrinsic SOTs within the KKR method. Our motivations for the use of the KKR formalism are twofold. First, the KKR method can easily be applied to very large systems because it uses a minimal basis set and it scales linearly with the number of atoms in its tight-binding formulation. Second, the KKR formalism is a Green function method based on scattering theory, in which it is very natural to obtain the scattering properties of impurities. Therefore, the KKR method is an ideal choice for the development of a highly scalable code to compute extrinsic SOTs in thin films.

This thesis is structured as follows: Chapter 2 gives an introduction about spin-

orbit torques in thin films from the phenomenological aspects to the microscopic mechanisms. We show how the SOT can be formally separated into even and odd components with respect to magnetization direction and discuss their relation to the underlying mechanisms. The spin-orbit torques induced by thermal gradients (T-SOT) are also discussed on the basis of the Mott relation.

In Chapter 3, we present the implementation of the Kubo formalism for the SOT within the full potential augmented plane-wave method. We first give an introduction about density functional theory and the FLAPW basis set. Then, we discuss the Wannier interpolation technique and present the parallelization scheme that was developed as part of this thesis for the calculation of the maximally localized Wannier functions. Finally, we give the formal Kubo expression that we use to compute the SOT within the FLAPW method.

Chapter 4 presents the KKR method and its application to the calculation of the scattering properties of impurities in otherwise periodic crystals. Then, we discuss the implementation of the torque and spin flux operators within the Jülich KKR code, which was achieved as a part of this thesis. Finally, we show how the scattering properties of impurities can be incorporated into the Boltzmann transport formalism for the calculation of impurity-driven extrinsic spin-orbit torques.

We proceed in Chapter 5 with the application of the FLAPW and KKR formalisms to calculate the SOTs in various types of ferromagnetic thin films. We first compute in Section 5.1 the SOTs induced by electric fields and thermal gradients in $L1_0$-FePt/Pt thin films. We discuss in detail the mechanisms giving rise to intrinsic and extrinsic SOTs in this system. We then investigate in Section 5.2 the SOT in Co/Cu thin films, where spin-orbit interaction is small compared to most bilayers previously investigated with respect to SOTs. We find a sizeable torque and discuss the crucial role of doping by impurities in that system. Next, we present in Section 5.3 the first ab initio calculations of SOTs in a Ag_2Bi-terminated Ag film grown on ferromagnetic Fe(110). Our study provides deep insight into recent experimental and theoretical works on similar systems. Finally, we conclude this thesis in Section 5.4 with the investigation of the SOT in Fe/Ge bilayers, where we discuss the advantages of using semiconductor substrates. We also consider the case of an antiferromagnetic Fe layer deposited on a Ge substrate.

2 Spin-orbit torques

The possibility of manipulating the magnetization of a ferromagnet by mean of electric currents was first pointed out by Berger [16] and Slonczewski [17]. Their original idea was based on the current-mediated exchange of spin angular momentum between two ferromagnetic layers of different magnetization directions: an electric current acquires a net spin polarization when it flows through a first layer (polarizer) and then exerts a magnetic torque on a second layer (analyser) by exchange interaction.

While the conventional spin-transfer torques (STTs) rely on the exchange of spin angular momentum between two ferromagnetic layers, the so-called spin-orbit torques (SOTs) discussed in this thesis rely on the spin-orbit-mediated exchange of angular momentum between the crystal lattice and the magnetization [3–5, 8, 9]. Beside the difference in the microscopic origin of the torques, the SOTs differ from the STTs in that they also exist in collinear magnetic systems as long as inversion symmetry is broken [6, 7], while the STTs require the magnetization to vary in space.

The goal of this section is to give an insight into the phenomenology of current-induced SOTs and discuss shortly the underlying mechanisms. First, we show how the phenomenological Landau-Lifshitz-Gilbert (LLG) equation is modified to account for current-induced SOTs and we discuss basic symmetry properties. Then, we discuss the microscopic origins of the SOTs in a simplified manner based on the spin Hall effect (SHE) and the Rashba model. After that, we give a short introduction into the linear response theory for the torque and discuss the different contributions on a more formal level. Finally, we show how the SOTs induced by thermal gradients are related to the SOTs induced by electrical currents.

2.1. Phenomenology of SOTs

A magnetic torque is by definition a rate of change of the spin angular momentum in a magnetic system. The discussion of magnetic torques, in particular of SOTs, is therefore closely related to the problem of describing the magnetization dynamics. The dynamics of the electrons spin in a magnetic material is quite different from the dynamics of an isolated spin in that there can be dissipation and exchange of angular momentum with the crystal lattice. The description of the magnetization dynamics

in a solid is usually based on the phenomenological LLG equation, where dissipation and magnetocrystalline anisotropy can be accounted for in a satisfying manner based on empirical parameters [18].

The LLG equation for a magnetization $\boldsymbol{M}$ in the presence of spin-orbit torques reads

$$\frac{d\hat{\boldsymbol{M}}}{dt} = -|\gamma|\hat{\boldsymbol{M}} \times \boldsymbol{S}^{eff} + \alpha\hat{\boldsymbol{M}} \times \frac{d\hat{\boldsymbol{M}}}{dt} - \frac{|\gamma|}{\mu_0 MV}\boldsymbol{T}(\boldsymbol{E}), \tag{2.1}$$

where $\hat{\boldsymbol{M}}$ and M are respectively the direction and the magnitude of the magnetization. The factor $|\gamma|$ is the gyromagnetic ratio of the electrons and α is the damping factor. Also the permeability constant μ_0 and the volume of the unit cell V (if the torque $\boldsymbol{T}$ is defined for a unit cell) enter the LLG equation. The first term on the right hand side of Eq. 2.1 describes the precession of the magnetization around the effective field $\boldsymbol{S}^{eff}$, which contains the effect of external magnetic fields and magnetocrystalline anisotropy. The second term is a dissipative term that tends to align the magnetization with the effective field $\boldsymbol{S}^{eff}$. The last term describes the effect on the magnetization of the electric field-induced spin-orbit torque $\boldsymbol{T}(\boldsymbol{E})$.

We consider in this work the linear regime where the SOT is related to the electric field $\boldsymbol{E}$ by the equation

$$\boldsymbol{T}(\boldsymbol{E}) = \boldsymbol{t}\boldsymbol{E}, \tag{2.2}$$

where $\boldsymbol{t}$ is the so-called torkance tensor [19].

A finite response of the torque to the electric field, i.e., a non zero torkance tensor, is possible only in a non-centrosymmetric system. To justify this let us observe how the torque, the electric field and the torkance entering Eq. 2.2 transform under inversion operation $\mathcal{I}$. The torque is a pseudovector since it relates to a change of magnetization and therefore is invariant under inversion: $\mathcal{I}[\boldsymbol{T}] = \boldsymbol{T}$. The electric field is a polar vector that changes sign under inversion: $\mathcal{I}[\boldsymbol{E}] = -\boldsymbol{E}$. The torkance tensor can be seen as a function of the position of the particles in the system $\{\boldsymbol{R}_i\}$ and be written as $\boldsymbol{t}(\{\boldsymbol{R}_i\})$. Inversion means that a particle at position $\boldsymbol{R}_i$ is moved to $\mathcal{I}[\boldsymbol{R}_i] = -\boldsymbol{R}_i$ (if the origin is chosen at the inversion center) and vice versa. If the system is centrosymmetric, the same particle is found at $\boldsymbol{R}_i$ and $-\boldsymbol{R}_i$, which implies $\mathcal{I}[\boldsymbol{t}] = \boldsymbol{t}$. Inversion symmetry therefore enforces that $\boldsymbol{t}\boldsymbol{E} = -\boldsymbol{t}\boldsymbol{E}$, which means that the linear response of the torque to the electric field has to vanish in a centrosymmetric system. Furthermore, it is clear that the torque in a collinear ferromagnetic system can only arise from spin-orbit coupling: conservation of total angular momentum implies that the spin angular momentum transferred to the magnetization is taken from the lattice.

We focus in this work on bilayer systems where inversion symmetry is structurally broken by having a ferromagnetic layer sandwiched between vacuum on one side and

a non-magnetic layer on the other side[1] (see Figs. 2.1b and 2.1c). The formalisms that are presented in this thesis in Sections 3 and 4 aim at computing from first principles the torkance tensor, i.e., the response of the torque to an external electric field. The motivations for this are twofold. First, the amplitude of the torkance computed for a typical value of current density, along with its symmetry, gives a good indication whether the system under consideration is a good candidate for an electrically switchable memory device. Second, among all parameters entering Eq. 2.1, the torkance is the only one with a pure interfacial character: it is a property of a stack of layers of different materials but is not easily related to the bulk properties of individual materials (unless the ferromagnetic material is itself non-centrosymetric). This is in contrast to the gyromagnetic ratio that deviates at surfaces from the bulk value by only a few percents, and to the damping factor that converges to the bulk value for thick ferromagnetic layers. This interfacial character of the torque, along with its strong sensitivity to the atomistic details of the interface, makes first principles calculations of the torkance tensor very valuable.

2.2. Discussion of the mechanisms

The origin of current-induced spin polarization and spin-orbit torques have been a matter of intense debate in the last years. Overall, the numerous experimental and theoretical investigations of SOTs in ferromagnetic bilayers suggest a classification of the torques according to two categories: the SOTs arising from the spin Hall effect (SHE) [9, 10] in the substrate and the SOTs due to interfacial spin-orbit coupling [3, 5, 6, 14]. The torques arising from the SHE rely on a transfer of spin angular momentum from the substrate to the ferromagnetic layer. It differs from the conventional spin transfer torque (STT) only by the origin of the spin current, which is in the present case generated by the spin-orbit interaction (SOI). The other type of torque does not rely on a spin Hall current but rather on the peculiar electronic structure of the interfacial region where SOI, magnetism and broken inversion symmetry coexist. These interfacial contributions to the torque are often discussed in the framework of the Rashba model. In this section we show how the origin and the symmetry of the different types of torques can be understood based on simplified approaches.

2.2.1. Spin Hall effect

The spin Hall effect (SHE) is a tool to generate a transverse spin current by applying an external electric field [11, 12]. In bilayers where a ferromagnetic thin film is deposited on a heavy metal (HM) substrate, the spin Hall current generated in the HM is injected into the ferromagnetic layer and thereby exerts a torque on the magnetization [9, 10]. This torque has in common with the conventional spin-transfer torque (STT) used in STT-MRAMs that it relies on the injection of a spin current into the ferromagnetic

[1] In fact there exist also bulk crystals that are themselves non-centrosymmetric and where a net torque is also induced by an external electric field, but they are not the focus of this work.

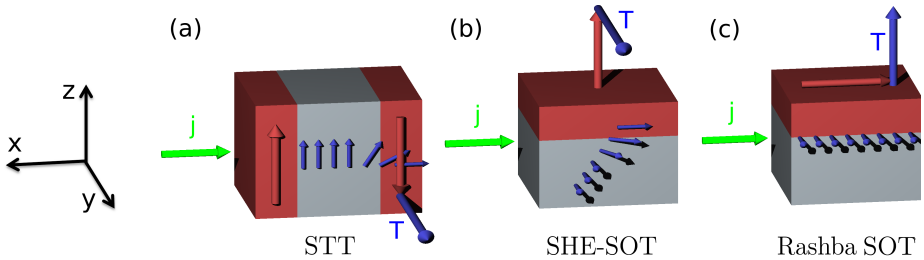

Figure 2.1.: (a) Conventional STT in a spin valve device. The left and right layers have the roles of the polarizer and the analyzer, respectively. (b) SOTs generated by the spin Hall effect in the heavy metal substrate according to Eq. 2.3. (c) SOTs generated by the interfacial spin-orbit coupling in the ferromagnetic Rashba model, see Eq. 2.10. The small blue arrows are an illustration of the spin currents and the induced spin accumulation. The large blue and green arrows give the direction of the torque $\boldsymbol{T}$ and the charge current $\boldsymbol{j}$, respectively. Red arrows show the direction of the local magnetization.

layer, but differs by the origin of the spin current. In the case of the conventional STT an electric current is polarized by an external polarizer (Fig. 2.1a) while in the case of the SHE-SOT the spin current originates from the spin-orbit coupling in the heavy metal substrate (Fig. 2.1b)[2].

The magnitude of the SOT arising from the SHE is closely related to the value of the spin Hall conductivity $\boldsymbol{\sigma}^s$ of the material used as a substrate. Assuming that (a) there are no other spin-flip processes taking place in the ferromagnet than those due to the exchange interaction and (b) there is no reflexion of the spin current at the interface, one finds a simple expression for the SHE-SOT:

$$\boldsymbol{T}^{\mathrm{SHE}} = \frac{2\mu_B}{\hbar M_S l_{FM}} \sum_{sj} \hat{\boldsymbol{M}} \times (\hat{\boldsymbol{e}}_s \times \hat{\boldsymbol{M}}) \sigma^s_{zj} E_j, \tag{2.3}$$

where σ^s_{zj} is the spin Hall conductivity of the substrate, the indices s and j are x or y and $\hat{\boldsymbol{e}}_s$ is a unit vector pointing in the s-direction. We also used the saturation magnetization M_S and the thickness of the ferromagnetic layer l_{FM}.

The torque defined by Eq. 2.3 is clearly an even function of the magnetization direction. This is a consequence of the spin continuity equation written under the assumption (a) that exchange interaction is the only source of spin-flip processes in the ferromagnet. If other sources of spin-flip processes exist in the ferromagnetic layer, such as spin-orbit interaction, the torque may also have an odd component.

[2]For the development of electrically switchable MRAMs, it is highly desirable to inject the writing current in the plane of the storage layer, as the read and write paths can then be fully decoupled.

However, exchange interaction is typically the dominant mechanism of spin-loss in the ferromagnet so that the odd part of the SHE-SOT is normally small compared to the even part.

Because the assumption (b) that there is no reflexion of the spin current at the interface is in general not valid, the amplitude of the SHE-SOT might be significantly smaller than suggested by Eq. 2.3. We define the SHE-to-SOT efficiency

$$\xi = \frac{|\boldsymbol{T}|}{|\boldsymbol{T}^{\mathbf{SHE}}|} \tag{2.4}$$

as the ratio of the actual torque $|\boldsymbol{T}|$ to the ideal torque $|\boldsymbol{T}^{\mathrm{SHE}}|$. The ideal SHE-SOT defined by Eq. 2.3 can be easily computed from the knowledge of the spin Hall conductivity $\boldsymbol{\sigma}^s$ of the material used as a substrate, which can be obtained from a bulk calculation. However, there is no general method to obtain the SHE-to-SOT efficiency for a given system. In fact, the SHE-to-SOT efficiency might strongly depend on the quality of the interface and the stacking direction, which makes the use of first principles calculations the method of choice for quantitative predictions of the torque.

2.2.2. Interfacial spin-orbit torques

The coexistence of spin-orbit coupling, magnetism and broken inversion symmetry yields a very peculiar electronic structure in the interfacial region of ferromagnetic bilayers. This property of the interface leads to new contributions to the torque that are not related to the spin Hall effect in the substrate. In order to illustrate the mechanisms that are involved in this type of interfacial torques, it is very instructive to consider the Rashba model, where the electronic states at the interface are modelled by a two-dimensional electron gas (2DEG) sandwiched between two different media.

Let us consider a 2DEG that models the valence electrons at the interface between two materials. A simple way to model the asymmetric environment seen by the 2DEG is to introduce an out-of-plane electric field $\boldsymbol{E} = E\boldsymbol{e}_z$ that is felt by the electrons. In the frame of the moving electrons the electric field transforms into a magnetic field $\boldsymbol{B} = -(\boldsymbol{p}/m \times \boldsymbol{E})/c^2$ according to the relativistic Lorentz transformation, where $\boldsymbol{p}$ is the electron momentum. This magnetic field interacts with the spin of the electrons, which leads to a spin-orbit coupling Hamitonian of the form[3]

$$H^{\mathrm{SO}} = \alpha(\boldsymbol{p} \times \hat{\boldsymbol{e}}_z) \cdot \boldsymbol{\sigma}, \tag{2.5}$$

where $\alpha = \mu_B g E/2mc^2$ is the so-called Rashba coupling constant.

The full Hamiltonian for a 2DEG in the presence of Rashba spin-orbit coupling

[3]This form can also be obtained from the general spin-orbit coupling Hamiltonian $H^{\mathrm{SO}} = \mu_{\mathrm{B}} g/2mc^2(\boldsymbol{p} \times \boldsymbol{E}) \cdot \boldsymbol{\sigma}$ for the special case $\boldsymbol{E} = E\hat{\boldsymbol{e}}_z$.

then reads

$$H(\boldsymbol{k}) = \frac{\hbar^2|\boldsymbol{k}|^2}{2m} + \alpha\hbar(\hat{\boldsymbol{e}}_z \times \boldsymbol{k}) \cdot \boldsymbol{\sigma}, \tag{2.6}$$

where the first term is the kinetic energy of free electrons. The second term is the Rashba spin-orbit coupling, which can be understood in terms of so-called k-dependent spin-orbit fields

$$\boldsymbol{B}^{\mathrm{SO}}(\boldsymbol{k}) = -\frac{\alpha\hbar}{\mu_{\mathrm{B}}}(\hat{\boldsymbol{e}}_z \times \boldsymbol{k}) \tag{2.7}$$

acting on the spin of the electrons. The spin-orbit fields lift the spin degeneracy of the 2DEG, which yields the very peculiar two-band electronic structure shown in Fig. 2.2a. For both bands the spin of the states is locked to the wave vector $\boldsymbol{k}$, but it is rotating clockwise in the one case and anticlockwise in the other case (Fig. 2.2b). The popularity of the Rashba model in the field of spintronics relies on the fact that the symmetry of the spin-orbit fields in k-space for real surfaces or interfaces is often well described by Eq. 2.7. Therefore, much of the transport properties of interfaces can be qualitatively understood based on this model. This is in particular true for current-induced spin polarization and SOTs, which is the main focus of this thesis.

We discuss now the spin polarization induced by an external in-plane electric field within the Rashba model. When an external electric field is applied to the system, the states with $\boldsymbol{k} \cdot \boldsymbol{E} < 0$ are populated while the ones with $\boldsymbol{k} \cdot \boldsymbol{E} > 0$ are depopulated. This yields a net spin polarization of different sign for each band, as shown in Fig. 2.2c. Because the two bands have different radii and density of states, the sum of the spin polarization has a finite value. It has been shown by Edelstein [14] that within the Rashba model the total current-induced spin polarization reads

$$\boldsymbol{s} = \frac{2\alpha m}{e\hbar\varepsilon_{\mathrm{F}}}(\boldsymbol{j} \times \hat{\boldsymbol{e}}_z), \tag{2.8}$$

where $\boldsymbol{j}$ is the charge current density and ε_{F} is the Fermi energy.

In a ferromagnetic system Eq. 2.6 has to be modified to account for the strong exchange interaction that couples the conduction electrons to the local magnetic moments. This yields the Hamiltonian

$$H(\boldsymbol{k}) = \frac{\hbar^2|\boldsymbol{k}|^2}{2m} + \alpha\hbar(\boldsymbol{k} \times \boldsymbol{e}_z) \cdot \boldsymbol{\sigma} + J_{\mathrm{ex}}\, \boldsymbol{\sigma} \cdot \hat{\boldsymbol{M}}, \tag{2.9}$$

where J_{ex} is the strength of the exchange interaction and $\hat{\boldsymbol{M}} = \boldsymbol{M}/|\boldsymbol{M}|$ is the magnetization direction. Since the exchange interaction is normally much stronger than the spin-orbit coupling, the spin of the electrons is essentially parallel to the magnetization direction while the spin-orbit field acts as a small perturbation. For simplicity we will focus on the case where magnetization lies in the plane of the film, which we illustrate in Fig. 2.2d.

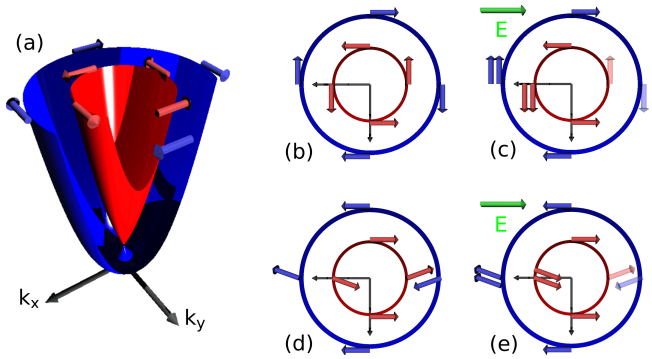

Figure 2.2.: (a) Band structure of the Rashba Hamiltonian defined by Eq. 2.6. (b) Spin expectation value of the states at the Fermi energy. (c) Illustration of the redistribution of the electrons when an external electric field is applied.(d) Spin expectation value of the states at the Fermi energy for the ferromagnetic Rashba Hamiltonian (Eq. 2.9) (e) Illustration of the redistribution of the electrons when an external electric field is applied for the ferromagnetic Rashba Hamiltonian (Eq. 2.9).

As previously, an external electric field applied in the plane of the field populates the states with $\boldsymbol{k} \cdot \boldsymbol{E} < 0$ and depopulates those with $\boldsymbol{k} \cdot \boldsymbol{E} > 0$, as shown in Fig. 2.2e. The spin accumulation thereby created in the ferromagnetic Rashba model yields a torque [6, 20]

$$\boldsymbol{T}^{\mathrm{R}} = \frac{2\alpha m J_{\mathrm{ex}}}{e\hbar^2 \varepsilon_{\mathrm{F}}} j(\hat{\boldsymbol{M}} \cdot \hat{\boldsymbol{E}})\hat{\boldsymbol{e}}_z \tag{2.10}$$

acting on the magnetization of the ferromagnetic layer, as shown in Fig. 2.1c.

The torque defined by Eq. 2.10 is clearly an odd function of magnetization direction. This is a consequence of the fact that the direction of the spin-orbit field felt by the electronic states is predominantly determined by the direction of the wave vector $\boldsymbol{k}$, but does not depend primarily on the magnetization direction.

2.3. Kubo formalism

In the following we present the formal linear response expressions for the torque that will be used in Section 3, and which ultimately leads to the Boltzmann description pursued in Section 4. We show that two qualitatively different types of torques can be identified in terms of their symmetries and discuss their relation to the SHE-SOT and interfacial SOT introduced in the previous chapter.

Within linear response theory the torkance tensor $\boldsymbol{t}$ defined by Eq. 2.2 has three

contributions [19]:

$$
\begin{aligned}
t_{ij}^{\mathrm{I(a)}} &= -\frac{e}{h}\int_{-\infty}^{\infty} d\varepsilon \frac{df(\varepsilon)}{d\varepsilon} \quad \mathrm{Tr}\langle \mathcal{T}_i G^{\mathrm{R}}(\varepsilon) v_j G^{\mathrm{A}}(\varepsilon)\rangle, \\
t_{ij}^{\mathrm{I(b)}} &= \frac{e}{h}\int_{-\infty}^{\infty} d\varepsilon \frac{df(\varepsilon)}{d\varepsilon} \Re\mathrm{Tr}\langle \mathcal{T}_i G^{\mathrm{R}}(\varepsilon) v_j G^{\mathrm{R}}(\varepsilon)\rangle, \\
t_{ij}^{\mathrm{II}} &= \frac{e}{h}\int_{-\infty}^{\infty} d\varepsilon f(\varepsilon) \quad \Re\mathrm{Tr}\langle \mathcal{T}_i G^{\mathrm{R}}(\varepsilon) v_j \frac{dG^{\mathrm{R}}(\varepsilon)}{d\varepsilon} \\
&\qquad - \mathcal{T}_i \frac{dG^{\mathrm{R}}(\varepsilon)}{d\varepsilon} v_j G^{\mathrm{R}}(\varepsilon)\rangle,
\end{aligned}
\tag{2.11}
$$

where $G^{\mathrm{R}}(\varepsilon)$ and $G^{\mathrm{A}}(\varepsilon)$ are the retarded and advanced Green functions, v_j is the jth Cartesian component of the velocity operator, $\mathcal{T}_i$ is the ith Cartesian component of the torque operator and $f(\varepsilon)$ is the Fermi-Dirac distribution function. The first two terms in Eq. 2.11 require the knowledge of the Green functions at the Fermi energy only because the derivative of the Fermi-Dirac distribution function $df(\varepsilon)/d\varepsilon$ reduces to a Dirac distribution in the zero temperature limit. These contributions are referred to as *Fermi surface* terms. The third term requires to integrate up to the Fermi level and is called the *Fermi sea* term.

The torque operator used in Eq. 2.11 is defined by

$$
\boldsymbol{\mathcal{T}}(\boldsymbol{r}) = -\mu_B \boldsymbol{\sigma} \times \boldsymbol{B}^{\mathrm{xc}}(\boldsymbol{r}) \tag{2.12}
$$

where $\boldsymbol{\sigma}$ is the vector of Pauli spin matrices. The exchange field $\boldsymbol{B}^{\mathrm{xc}}(\boldsymbol{r})$ varies rapidly at the atomic scale, analogously to the electrostatic potential, and its accurate description requires the use of *ab initio* calculations. The naive approximation of a constant exchange field $\bar{\boldsymbol{B}}^{\mathrm{xc}}$ would greatly simplify the formalism, since the knowledge of the spin $\langle\boldsymbol{\sigma}\rangle$ of the electron would suffice to determine the exerted torque $\langle\boldsymbol{\mathcal{T}}\rangle = -\mu_B\langle\boldsymbol{\sigma}\rangle \times \bar{\boldsymbol{B}}^{\mathrm{xc}}$. However, this usually gives a poor estimate of the torque, and it is necessary to account for the inhomogeneity of the exchange field to obtain accurate results.

At this step, we model the influence of disorder in the system by a constant effective band broadening Γ, which is equivalent to a constant relaxation time approximation. Within this model the retarded and advanced Green functions are given by $G^{\mathrm{R}}(\varepsilon) = \hbar[\varepsilon - H + i\Gamma]^{-1}$ and $G^{\mathrm{A}}(\varepsilon) = \hbar[\varepsilon - H - i\Gamma]^{-1}$, where the parameter Γ characterizes the disorder strength and H is the Hamiltonian describing the electrons in the potential of the nuclei. This model offers two advantages from the technical point of view. First, the expansion of the Green function for the disordered system in terms of eigen states of the Hamiltonian H is straightforward within this model, see Eqs. 3.63 and 3.65. Second, it is possible to derive insightful analytical expressions for the clean system by taking the limit $\Gamma \to 0$. In the following we discuss in details this so-called clean limit.

It is very instructive to decompose the torkance tensor $\boldsymbol{t}$ into even and odd components with respect to the direction of magnetization: $t_{ij} = t_{ij}^{\text{even}} + t_{ij}^{\text{odd}}$. In the clean limit we obtain:

$$t_{ij}^{\text{even}} = \frac{2e}{\mathcal{N}} \hat{\boldsymbol{e}}_i \cdot \sum_{\boldsymbol{k},n} f(\varepsilon_{\boldsymbol{k}n}) \left[\hat{\boldsymbol{M}} \times \Im \left\langle \frac{\partial u_{\boldsymbol{k}n}}{\partial \hat{\boldsymbol{M}}} \middle| \frac{\partial u_{\boldsymbol{k}n}}{\partial k_j} \right\rangle \right], \tag{2.13}$$

and

$$t_{ij}^{\text{odd}} = -\frac{e\hbar}{2\Gamma\mathcal{N}} \sum_{\boldsymbol{k}n} \langle \psi_{\boldsymbol{k}n} | \mathcal{T}_i | \psi_{\boldsymbol{k}n} \rangle \langle \psi_{\boldsymbol{k}n} | v_j | \psi_{\boldsymbol{k}n} \rangle \frac{\partial f(\varepsilon_{\boldsymbol{k}n})}{\partial \varepsilon}, \tag{2.14}$$

where $\mathcal{N}$ is the number of $\boldsymbol{k}$-points in the Brillouin zone, n is a band index, $\varepsilon_{\boldsymbol{k}n}$ are the eigenenergies of the system, $\psi_{\boldsymbol{k}n}$ and $u_{\boldsymbol{k}n}$ are the Bloch states and their lattice-periodic parts, and $\hat{\boldsymbol{e}}_i$ is a unit vector along the ith Cartesian direction. The even torkance has the form of a Berry curvature and it is independent of Γ in the clean limit. It constitutes the intrinsic contribution to the torkance, and it is analogous to the intrinsic spin Hall conductivity [21]. The odd part of the torkance, on the other hand, has the form of a Fermi surface integral and diverges like $1/\Gamma$, i.e., it is proportional to the quasi-particle lifetime. It reduces to the Boltzmann response function in the limit $T \to 0$ and it is governed by the change of the distribution function induced by the external electric field. We will discuss in Section 4 how it is possible to treat the odd torkance beyond the constant relaxation time approximation by taking explicitly into account the effect of impurity scattering.

It is important to note that, while the even torkance defined by Eq. 2.13 is formulated as an intraband contribution (there is only one band index), the derivatives of $u_{\boldsymbol{k}n}$ with respect to $\hat{\boldsymbol{M}}$ and k_j have to be expanded into eigen states of different energies. This yields an alternative expression for the even torkance in the clean limit [19]:

$$t_{ij}^{\text{even}} = \frac{2e\hbar}{\mathcal{N}} \sum_{\boldsymbol{k}} \sum_{n}^{\text{occ}} \sum_{m \neq n} \text{Im} \left[\frac{\langle \psi_{\boldsymbol{k}n} | \mathcal{T}_i | \psi_{\boldsymbol{k}m} \rangle \langle \psi_{\boldsymbol{k}m} | v_j | \psi_{\boldsymbol{k}n} \rangle}{(\varepsilon_{\boldsymbol{k}m} - \varepsilon_{\boldsymbol{k}n})^2} \right], \tag{2.15}$$

in which the off-diagonal elements of the torque and velocity operators enter explicitly, and where two band indices are used. It is immediately clear from Eq. 2.15 that the intrinsic torkance arising from the Berry curvature is related to interband transitions from the point of view of Eq. 2.11. This is in sharp contrast to the odd torkance, which is a pure intraband contribution and is governed by the change of the distribution function induced by the external electric field.

It is useful to discuss how the even and odd torkances defined by Eqs. 2.13 and 2.14 relate to the different mechanisms presented in Section 2.2. The predominant even parity predicted in Section 2.2.1 for the SHE-SOT suggests that this mechanism enters mostly the even torkance. This is strongly supported by the intrinsic character of both the even torkance and the spin-Hall conductivity in the clean limit. The interfacial SOT discussed in Section 2.2.2, on the other hand, is an odd function of magnetization

direction. It diverges like $1/\Gamma$ in the limit of small Γ, similarly to the odd torkance defined by Eq. 2.14.

2.4. Thermal spin-orbit torques

Similarly to the spin Hall or anomalous Hall conductivities, the torkance tensor describes the SOT arising from an applied electric field, i.e., it corresponds to the situation where the torque is driven by a mechanical force. A torque can also be induced by a temperature gradient, i.e., it can also originate from statistical forces. In this section we discuss how the thermal torques can be computed on the basis of general relations between thermal and electrical transport coefficients known as Mott relations.

Within the semiclassical theory of electronic transport, both thermal and electrical response functions arise from the change of the distribution function: a temperature gradient induces a position dependent distribution function while an electric field modifies the distribution of the electrons in k-space. The exact relation between electrical conductivity and its thermal counterpart is given by the Mott relation. However, it is not obvious at first sight by which mechanisms Berry-phase-induced phenomena, such as the intrinsic anomalous Hall effect or spin-orbit torques, can arise from thermal gradients. A first explanation has been proposed for the case of the anomalous Nernst effect by Xiao *et al.* [22], who have shown that the Berry-phase correction to the orbital magnetization is the key to understand anomalous thermoelectric transport. An analogous theory has been developed by Freimuth *et al.* [23] for the case of the thermally induced SOTs, where the thermal torque arises from the so-called *twist torque moments*. This theory gives a microscopic justification to the Mott relation between electrical and thermal SOTs.

While the existence of the thermally induced SOT has been shown, there has been no experimental evidence reported so far. This raises the question of the magnitude of this effect, which we address in this thesis in Section 3 for the case of $L1_0$-FePt/Pt bilayers. We discuss in the following the Mott relation, which we use to compute the thermal torkance from the electrical torkance computed from first principles.

In analogy to the torkance driven by electrical currents (Eq. 2.2), we define the thermal torkance tensor $\boldsymbol{\beta}$ by the expression

$$\boldsymbol{T}(\boldsymbol{E}) = -\boldsymbol{\beta}\boldsymbol{\nabla}T, \tag{2.16}$$

where $\boldsymbol{\nabla}T$ is the temperature gradient. We decompose the thermal torkance into even and odd components with respect to the magnetization direction: $\beta_{ij} = \beta_{ij}^{\text{even}} + \beta_{ij}^{\text{odd}}$. The intrinsic even part of the thermal torkance is analogous to the intrinsic anomalous Nernst [22, 24] and spin Nernst conductivities [25–28], while the odd part of the thermal torkance is similar to the Seebeck effect. Both even and odd components of

the thermal torkance can be computed directly from their mechanical counterparts employing the Mott relation [23]:

$$\beta_{ij}(T) = -\frac{1}{e}\int d\varepsilon \frac{\partial f(\varepsilon,\mu,T)}{\partial \mu} t_{ij}(\varepsilon)\frac{\varepsilon-\mu}{T} \tag{2.17}$$

where $t_{ij}(\varepsilon)$ is the torkance tensor with Fermi energy set to ε and μ is the chemical potential.

The relation between electrical and thermal torkances appears much more clearly if one investigates the limit of $T \to 0$. For this let us define the function

$$S(\varepsilon) = -t_{ij}(\varepsilon)\frac{1}{e}\frac{\varepsilon-\mu}{T} \tag{2.18}$$

and rewrite Eq. (2.17) as

$$\beta_{ij}(T) = \int d\varepsilon \frac{\partial f(\varepsilon,\mu,T)}{\partial \mu} S(\varepsilon). \tag{2.19}$$

We can compute this integral by a method similar to the well known Sommerfeld expansion [29]. At low temperature the derivative of the Fermi function is appreciable only close to the chemical potential μ. We can therefore use the second-order Taylor series expansion

$$\begin{aligned} S(\varepsilon) &= (\varepsilon-\mu)\frac{\partial S}{\partial \varepsilon}\bigg|_{\varepsilon=\mu} + \frac{1}{2}(\varepsilon-\mu)^2\frac{\partial^2 S}{\partial \varepsilon^2}\bigg|_{\varepsilon=\mu} + ... \\ &= -\frac{1}{e}\frac{(\varepsilon-\mu)}{T}t_{ij}(\mu) - \frac{1}{e}\frac{(\varepsilon-\mu)^2}{T}\frac{\partial t_{ij}}{\partial \varepsilon}\bigg|_{\varepsilon=\mu} + ... \end{aligned} \tag{2.20}$$

Inserting this expansion in Eq. (2.19) yields

$$\begin{aligned} \beta_{ij}(T) = &-\frac{1}{e}\int d\varepsilon \frac{\partial f(\varepsilon,\mu,T)}{\partial \mu}\frac{(\varepsilon-\mu)}{T}t_{ij}(\mu) \\ &-\frac{1}{e}\int d\varepsilon \frac{\partial f(\varepsilon,\mu,T)}{\partial \mu}\frac{(\varepsilon-\mu)^2}{T}\frac{\partial t_{ij}}{\partial \varepsilon}\bigg|_{\varepsilon=\mu}. \end{aligned} \tag{2.21}$$

The first term in the previous equation vanishes because the integrand is the product of the even function $\partial f(\varepsilon,\mu,T)/\partial\mu$ with the odd function $(\varepsilon-\mu)/T$. The remaining part can be rewritten as

$$\beta_{ij}(T) = -\frac{1}{e}k_B^2 T\frac{\partial t_{ij}}{\partial \varepsilon}\bigg|_{\varepsilon=\mu}\int dx(-\frac{\partial}{\partial x}\frac{1}{e^x+1})x^2 \tag{2.22}$$

where we introduced a new variable $x = \frac{\varepsilon-\mu}{k_B T}$. The integral in Eq. (2.22) is equal to $\pi^2/3$ [29]. The final expression for the thermal torkance in the limit of low temperature is then given by

$$\beta_{ij}(T) = -\frac{\pi^2 k_B^2 T}{3e}\frac{\partial t_{ij}}{\partial \varepsilon}\bigg|_{\varepsilon=\mu}, \tag{2.23}$$

i.e., the thermal torkance is directly proportional to the derivative of the torkance at a given energy, rather than its magnitude.

3 SOTs in the FLAPW method

In the previous chapter we have introduced the general expressions for the calculation of electrical and thermal spin-orbit torques within the Kubo formalism. We discuss now the implementation of the Kubo formula in the full potential linearized augmented plane waves (FLAPW) method, which is widely recognized as the most accurate computational method to perform density functional theory (DFT) calculations of periodic systems. We first introduce the essential elements of DFT and discuss in particular its Kohn-Sham formulation. We then discuss the construction of the FLAPW basis set and its advantages over other augmented plane wave methods. Next, we introduce the Wannier interpolation technique and the parallelization of the WANNIER90 code that has been achieved as part of this thesis. Finally, we give the exact expressions for the torkance in terms of the Bloch states and their corresponding energies, which we use in Section 5.1 to investigate electrical and thermal SOTs in $L1_0$-FePt/Pt bilayers.

3.1. Density Functional Theory (DFT)

3.1.1. The many body problem

Most properties of solids can be understood from the motion of the electrons in the electrostatic potential created by the nuclei. The problem of finding the many body electronic wave function $\Psi(\boldsymbol{r}_1, \boldsymbol{r}_2, ..., \boldsymbol{r}_N)$ for a system of N electrons can be addressed by solving the Schrödinger equation

$$H\Psi(\boldsymbol{r}_1, \boldsymbol{r}_2, ..., \boldsymbol{r}_N) = E\Psi(\boldsymbol{r}_1, \boldsymbol{r}_2, ..., \boldsymbol{r}_N), \tag{3.1}$$

where H is the many body Hamiltonian

$$H = \sum_{i=1}^{N} \Big(-\frac{\hbar^2}{2m}\Delta_i + v_{\text{ext}}(\boldsymbol{r}_i)\Big) + \sum_{i\neq j}^{N} \frac{e^2}{4\pi\epsilon_0}\frac{1}{|\boldsymbol{r}_i - \boldsymbol{r}_j|}. \tag{3.2}$$

The first and second terms in Eq. 3.2 correspond respectively to the kinetic energy and to the interaction of the electrons with the electrostatic potential $v_{\text{ext}}(\boldsymbol{r})$ created by the nuclei. The last term is the Coulomb interaction between electrons, which gives rise to a correlation of the motion of the different electrons in the system. This means

in practice that the many body wavefunction $\Psi(\boldsymbol{r}_1, \boldsymbol{r}_2, ..., \boldsymbol{r}_N)$ solution of Eq. 3.1 can not be written as a Slater determinant of single particle wavefunctions $\psi_i(\boldsymbol{r})$. It is then not possible to reduce the many body problem defined by Eq. 3.1 to a single particle problem and one has to work with the full many body wavefunction $\Psi(\boldsymbol{r}_1, \boldsymbol{r}_2, ..., \boldsymbol{r}_N)$ of correlated electrons. However, for systems with more than a few electrons it is not possible to solve Eq. 3.1 exactly, because the number of values necessary to represent the wavefunction $\Psi(\boldsymbol{r}_1, \boldsymbol{r}_2, ..., \boldsymbol{r}_N)$ becomes intractable.

In most practical applications one is not directly interested in the electronic wavefunction itself, but in the expectation value of an observable $\mathcal{O}$ given by

$$\langle \mathcal{O} \rangle = \langle \Psi | \mathcal{O} | \Psi \rangle. \tag{3.3}$$

Therefore, the development of *ab initio* methods that enable the calculation of expectation values without the knowledge of the exact many body wavefunction is of strong interest. The so-called *density functional theory* yields an exact and systematic scheme for solving many body problems, where the calculation of the electronic wavefunction is circumvented by the use of functionals of the electronic density for the expectation values of observables.

3.1.2. Hohenberg-Kohn theorem

The basic idea of DFT is to use the electronic density instead of the many body wavefunction as the central quantity of the theory. This can be achieved by using the Hohenberg-Kohn theorem, which states that the electronic density $n(\boldsymbol{r})$ contains the same information as the ground-state wave function $\Psi(\boldsymbol{r}_1, \boldsymbol{r}_2, ..., \boldsymbol{r}_N)$. In other words, all observables can be expressed as functionals of the density, which is in particular true for the total energy

$$\langle \Psi | H | \Psi \rangle = E[n]. \tag{3.4}$$

Therefore, one can obtain the electronic density $n(\boldsymbol{r})$ by minimizing the energy functional $E[n]$. This energy functional can be written as

$$E[n(\boldsymbol{r})] = T[n(\boldsymbol{r})] + V_{\text{ext}}[n(\boldsymbol{r})] + V_{\text{ee}}[n(\boldsymbol{r})], \tag{3.5}$$

where $T[n(\boldsymbol{r})]$ is the kinetic energy, $V_{\text{ext}}[n(\boldsymbol{r})]$ is the potential energy due to the interaction of the electrons with the external potential and $V_{\text{ee}}[n(\boldsymbol{r})]$ is the potential energy due to the electron-electron interaction.

Although the existence of a universal total energy functional $E[n(\boldsymbol{r})]$ has been shown, its exact form is unknown and the calculation of the ground state density in DFT calculations relies on approximations to the true energy functional. In particular, a difficulty immediately arises for the determination of the kinetic energy, which is given by the second space derivatives of the many body wave function in the Schrödinger equation. The Kohn-Sham formulation of DFT yields a practical algorithm for the determination of the kinetic energy and for the minimization of the total energy functional $E[n(\boldsymbol{r})]$.

3.1.3. Kohn-Sham equation

The Kohn-Sham formulation of DFT relies on the introduction of a fictitious system of non-interacting electrons, which has the same ground-state density as the real interacting system. The Kohn-Sham equation is the Schrödinger equation for this non-interacting system:

$$\Big[-\frac{\hbar^2}{2m}\nabla^2 + v_{\text{eff}}(\boldsymbol{r})\Big]\psi_i(\boldsymbol{r}) = \varepsilon_i\psi_i(\boldsymbol{r}). \tag{3.6}$$

The Kohn-Sham orbitals solutions of Eq. 3.6 yield a convenient way to estimate the kinetic energy of the many body system:

$$T_{\text{KS}}[n(\boldsymbol{r})] = \sum_i^{\text{occ}} \frac{\hbar^2}{2m}\langle\psi_i|\nabla^2|\psi_i\rangle. \tag{3.7}$$

The total energy of the system can be rewritten as

$$E[n(\boldsymbol{r})] = T_{\text{KS}}[n(\boldsymbol{r})] + \int d\boldsymbol{r}\; n(\boldsymbol{r})\, v_{\text{ext}}(\boldsymbol{r}) + \frac{e^2}{2}\int\int d\boldsymbol{r}d\boldsymbol{r'}\; \frac{n(\boldsymbol{r})\, n(\boldsymbol{r'})}{|\boldsymbol{r}-\boldsymbol{r'}|} + E_{xc}[n(\boldsymbol{r})], \tag{3.8}$$

where $E_{xc}[n(\boldsymbol{r})]$ is the so-called *exchange and correlation* functional that contains the unknown remaining part of the energy.

The effective potential $v_{\text{eff}}(\boldsymbol{r})$ should be chosen in such a way that the ground state density obtained from Eq. 3.6 minimizes the energy functional $E[n]$. This condition is fulfilled by the following expression [30]:

$$v_{\text{eff}}(\boldsymbol{r}) = v_{\text{ext}}(\boldsymbol{r}) + e^2\int \frac{n(\boldsymbol{r'})}{|\boldsymbol{r}-\boldsymbol{r'}|}d\boldsymbol{r'} + \frac{\delta E_{xc}[n]}{\delta n(\boldsymbol{r})}. \tag{3.9}$$

Since the effective potential $v_{\text{eff}}(\boldsymbol{r})$ depends itself on the charge density $n(\boldsymbol{r})$, Eqs. 3.6 and 3.9 have to be solved self-consistently.

Different approximations exist for the exchange and correlation energy functional $E_{xc}[n]$ in the literature. We use in this thesis the local density approximation (LDA), where $E_{xc}^{\text{LDA}}[n]$ depends only on the value of $\boldsymbol{r}$ at each point in space

$$E_{xc}^{\text{LDA}}[n(\boldsymbol{r})] = \int d\boldsymbol{r}\; \epsilon_{xc}^{\text{LDA}}(n(\boldsymbol{r})), \tag{3.10}$$

and the generalized gradient approximation (GGA), where $E_{xc}^{\text{GGA}}[n]$ also depends on the gradient of the density

$$E_{xc}^{\text{GGA}}[n(\boldsymbol{r})] = \int d\boldsymbol{r}\; \epsilon_{xc}^{\text{GGA}}(n(\boldsymbol{r}), \nabla n(\boldsymbol{r})). \tag{3.11}$$

There exist different parametrizations for the exchange and correlation energy density $\epsilon_{xc}^{\text{LDA}}(n(\boldsymbol{r}))$ and $\epsilon_{xc}^{\text{GGA}}(n(\boldsymbol{r}), \nabla n(\boldsymbol{r}))$. We use for LDA the one from Vosko, Wilk and

Nusair [31] and for GGA the one from Perdew, Burke, and Ernzerhof [32].

Besides the convenient scheme it provides for the determination of the electronic density, the Kohn-Sham formulation of DFT yields an elegant alternative to Eq. 3.3 for the calculation of the expectation values of observables

$$\langle \mathcal{O} \rangle = \sum_{i}^{\text{occ}} \langle \psi_i | \mathcal{O} | \psi_i \rangle. \tag{3.12}$$

Therefore, the Kohn-Sham formulation of DFT yields an effective and systematic approach for the calculation of physical quantities, where it is not required to diagonalize the full many-body Hamitonian. Instead, we can use the Kohn-Sham orbitals, solutions of a more simple single particle Hamitonian, to compute expectation values of observables according to Eq. 3.12.

3.2. FLAPW method

The solutions of Eq. 3.6 can be calculated using an expansion of the wave functions on a set of basis functions. A simple choice of basis functions are plane waves, which are orthogonal and allow a straightforward expansion of the Hamiltonian. However, a very high number of plane waves would be needed to capture the very rapid oscillations of the wave functions close to the nuclei. In order to restrict the number of basis functions and thus increase the performance of the calculation, an alternative approach has been proposed by Slater [33], which is known as the augmented planewave method (APW).

Within the APW approach, space is decomposed between atomic spheres (muffin-tins) centered on the nuclei and the remaining part (interstitial region) between the nuclei. The basis functions are given by plane waves in the interstitial region and by products of spherical harmonics with radial wave functions inside the muffin-tins:

$$\phi_{\boldsymbol{G}}(\boldsymbol{k}, \boldsymbol{r}) = \begin{cases} e^{i(\boldsymbol{G}+\boldsymbol{k})\cdot\boldsymbol{r}} & \text{interstitial region} \\ \sum\limits_{L} A_L^{\mu\boldsymbol{G}}(\boldsymbol{k}) u_l^{\mu}(r) Y_L(\hat{\boldsymbol{r}}) & \text{muffin-tin } \mu. \end{cases} \tag{3.13}$$

where $\boldsymbol{G}$ is a reciprocal lattice vector and $L = \{l, m\}$ a combined index for azimuthal quantum number l and magnetic quantum number m. The coefficients $A_L^{\mu\boldsymbol{G}}(\boldsymbol{k})$ are chosen such that the basis functions are continuous at the muffin-tin boundary. The radial wave functions $u_l^{\mu}(r)$ are the solutions of the radial Schrödinger equation

$$\Big\{ -\frac{\hbar^2}{2m}\frac{\partial^2}{\partial r^2} + \frac{\hbar^2}{2m}\frac{l(l+1)}{r^2} + V^{\mu}(r) - E_l^{\mu} \Big\} r u_l^{\mu}(r) = 0, \tag{3.14}$$

where E_l^{μ} is an energy parameter and $V^{\mu}(r)$ the spherical potential inside muffin-tin μ. It turns out the basis functions defined by Eq. 3.13 offer enough variational freedom

only if the energy parameters E_l^μ are chosen k- and G-dependent. This makes the determination of the band energies way more complicate than if the energy parameters could be kept fixed. This is the major drawback of the APW method and we discuss in the following how this problem is circumvented within the linearized augmented planewave (LAPW) method.

Within the LAPW method the basis functions in the muffin-tins are linear combinations of the radial functions $u_l^\mu(r)$ (Eq. 3.14) and of their energy derivatives $\dot{u}_l^\mu(r)$. The corresponding basis functions in the LAPW method read[1]

$$\phi_{\boldsymbol{G}}(\boldsymbol{k},\boldsymbol{r}) = \begin{cases} e^{i(\boldsymbol{G}+\boldsymbol{k})\cdot\boldsymbol{r}} & \text{interstitial region} \\ \sum_L \Big[A_L^{\mu\boldsymbol{G}}(\boldsymbol{k})u_l^\mu(r) + B_L^{\mu\boldsymbol{G}}(\boldsymbol{k})\dot{u}_l^\mu(r)\Big]Y_L(\hat{\boldsymbol{r}}) & \text{muffin-tin } \mu, \end{cases} \tag{3.15}$$

and the derivatives $\dot{u}_l^\mu(r)$ are obtained by taking the derivative of Eq. 3.14 with respect to the energy, which yields

$$\Big\{-\frac{\hbar^2}{2m}\frac{\partial^2}{\partial r^2} + \frac{\hbar^2}{2m}\frac{l(l+1)}{r^2} + V^\mu(r) - E_l^\mu\Big\} r\dot{u}_l^\mu(r) = r u_l^\mu(r). \tag{3.16}$$

The additional coefficients $B_L^{\mu\boldsymbol{G}}(\boldsymbol{k})$ in Eq. 3.15 drastically increases the variational freedom of the basis set. Unlike in the APW method, it is now sufficient to define a single set of $u_l^\mu(r)$ and $\dot{u}_l^\mu(r)$ radial wave functions for fixed energy parameters E_l^μ. This greatly simplifies the determination of the band energies by diagonalization of the Hamiltonian, which explains the popularity of the LAPW method over the APW method.

The Bloch states are then expanded into the basis functions $\phi_{\boldsymbol{G}}(\boldsymbol{k},\boldsymbol{r})$ according to

$$\psi_{m\boldsymbol{k}}(\boldsymbol{r}) = \sum_{\boldsymbol{G}} c_{m\boldsymbol{G}}(\boldsymbol{k})\phi_{\boldsymbol{G}}(\boldsymbol{k},\boldsymbol{r}), \tag{3.17}$$

where m is the band index. The problem of solving Eq. 3.6 therefore reduces to the determination of the $c_{m\boldsymbol{G}}(\boldsymbol{k})$ coefficients.

Historically the LAPW method has been used with the approximation that atomic potentials exhibit a spherical shape. This approximation yields good results in many cases for bulk systems, but is lacking accuracy for film calculations. The generalization of the LAPW method to the case of arbitrary shape of atomic potentials is called the full potential linearized augmented planewave (FLAPW) method.

3.3. Wannier functions

The evaluation of the Kubo formula for the torque (Eq. 3.67) requires the knowledge of the Bloch states for a very large number of k-points in the Brillouin zone. Typically,

[1] For film calculations it is necessary to define the basis functions also in the vacuum regions. For details of the implementation in the FLEUR code, see Ref.[34].

between 10^6 and 10^9 k-resolved Hamiltonians have to be set up and diagonalized (depending on the dimension of the system) in order to achieve convergence of the torque with respect to the number of k-points. The corresponding computational cost is way too high and one needs an efficient interpolation scheme to avoid brutal force diagonalization of too many matrices. A very efficient scheme is provided by the Wannier interpolation technique.

In the following we give a short view of the theoretical background that underlies the Wannier interpolation technique. First, we give the definition of Wannier functions and discuss the importance of the gauge choice for their localization properties. Then, we give an overview of the method developed by Marzari and Vanderbilt [35] for computing maximally localized Wannier functions (MLWFs) and we describe how the WANNIER90 code [36] has been parallelized as part of this thesis. Finally, we show how the Bloch states for millions of k-points can be interpolated from a comparatively very small number of Wannier functions.

3.3.1. Definition

We start by considering the case of a band well separated from all other bands, and we will generalize to the case of a group of bands later on. The Wannier function for an isolated band n is defined by the Fourier transform of the Bloch states $\psi_{n\boldsymbol{k}}(\boldsymbol{r})$, i.e.,

$$W_{n\boldsymbol{R}}(\boldsymbol{r}) = \frac{V}{8\pi^3} \int_{\mathrm{BZ}} e^{-i\boldsymbol{k}\cdot\boldsymbol{R}}\, \psi_{n\boldsymbol{k}}(\boldsymbol{r})\, d\boldsymbol{k}, \tag{3.18}$$

where V is the volume of a unit cell and $\boldsymbol{R}$ is a lattice vector. The Wannier functions for different lattice vectors are related to each other by the corresponding translations, i.e., $W_{n\boldsymbol{R}'}(\boldsymbol{r}) = W_{n\boldsymbol{R}}(\boldsymbol{r} + \boldsymbol{R} - \boldsymbol{R}')$. In Eq. 3.18 the eigen states $\psi_{n\boldsymbol{k}}(\boldsymbol{r})$ are defined up to a phase constant $\varphi_n(\mathbf{k})$, i.e., we have the gauge freedom

$$\psi_{n\boldsymbol{k}}(\boldsymbol{r}) \to e^{i\varphi_n^{(\boldsymbol{k})}}\, \psi_{n\boldsymbol{k}}(\boldsymbol{r}). \tag{3.19}$$

It turns out that the shape of the Wannier functions defined by Eq. 3.18 strongly depends on the choice of the gauge. For an efficient interpolation scheme it is necessary to generate Wannier functions that are to some extent localized, so that the interpolated Bloch states can be obtained by an inverse Fourier transform truncated to a small number of unit cells (see Section 3.3.4). The choice of the $\varphi_n^{(\mathbf{k})}$ phases is therefore crucial.

In the case of N energy bands forming an isolated group (composite band), one can allow for an additional gauge freedom that mixes the Bloch states according to

$$\psi_{n\boldsymbol{k}}(\boldsymbol{r}) \to \sum_{m=1}^{N} U_{nm}^{(\boldsymbol{k})}\, \psi_{m\boldsymbol{k}}(\boldsymbol{r}) = \widetilde{\psi}_{n\boldsymbol{k}}(\boldsymbol{r}). \tag{3.20}$$

and their periodic parts according to

$$u_{n\boldsymbol{k}}(\boldsymbol{r}) \to \sum_{m=1}^{N} U_{nm}^{(\boldsymbol{k})}\, u_{m\boldsymbol{k}}(\boldsymbol{r}) = \widetilde{u}_{n\boldsymbol{k}}(\boldsymbol{r}). \tag{3.21}$$

This can be seen as a generalization of Eq. 3.19 where the $U^{(\boldsymbol{k})}$ matrix was chosen diagonal. The rotated Bloch states $\widetilde{\psi}_{n\boldsymbol{k}}(\boldsymbol{r})$ are not eigen states of the Hamiltonian if the $U^{(\boldsymbol{k})}$ matrix has off-diagonal elements, but can still be used to define *generalized* Wannier functions according to

$$W_{n\boldsymbol{R}}(\boldsymbol{r}) = \frac{V}{8\pi^3} \int_{\mathrm{BZ}} e^{-i\boldsymbol{k}\cdot\boldsymbol{R}} \sum_{m=1}^{N} U_{nm}^{(\boldsymbol{k})}\, \psi_{m\boldsymbol{k}}(\boldsymbol{r})\, d\boldsymbol{k} \tag{3.22}$$

$$= \frac{V}{8\pi^3} \int_{\mathrm{BZ}} e^{-i\boldsymbol{k}\cdot\boldsymbol{R}}\, \widetilde{\psi}_{n\boldsymbol{k}}(\boldsymbol{r})\, d\boldsymbol{k}. \tag{3.23}$$

Therefore, the problem of finding well localized (generalized) Wannier functions now reduces to the choice of a suitable $U^{(\boldsymbol{k})}$ gauge transformation.

A systematic way of constructing maximally localized Wannier functions for composite bands has been proposed by Marzari and Vanderbilt [35], which have paved the way to the use of Wannier functions as a powerful interpolation technique. The method can be extended to the case of entangled bands, i.e., to bands that do not form an isolated group [37]. We use the implementation of the Wannier functions within the FLAPW formalism developed by Freimuth *et al.* [38].

3.3.2. Maximally localized Wannier functions

The WANNIER90 program [36] addresses the question of minimizing the spread of the Wannier functions by finding the optimal choice for the gauge $U^{(\boldsymbol{k})}$. We give in the following an overview of the method developped by Marzari and Vanderbilt [35] and finally describe how the code has been parallelized for this thesis.

Spread of Wannier functions

We define the total spread of the Wannier functions by

$$\Omega = \sum_n [\langle W_{0n}|r^2|W_{0n}\rangle - |\langle W_{0n}|\boldsymbol{r}|W_{0n}\rangle|^2] = \sum_n [\langle r^2\rangle_n - |\langle \boldsymbol{r}\rangle_n|^2], \tag{3.24}$$

where the sum runs over all occupied bands. For a given set of Bloch states computed from *ab initio*, the spread depends only on the gauge choice $U^{(\boldsymbol{k})}$ and can be written as a functional $\Omega[U^{(\boldsymbol{k})}]$.

It is fruitful to decompose the spread as the sum of three contributions:

$$\Omega_{\mathrm{I}} = \sum_{n} [\langle r^2 \rangle_n - \sum_{\boldsymbol{R}m} |\langle W_{\boldsymbol{R}m} | \boldsymbol{r} | W_{0n} \rangle|^2], \tag{3.25}$$

$$\Omega_{\mathrm{D}} = \sum_{n} \sum_{\boldsymbol{R}\neq 0} |\langle W_{\boldsymbol{R}n} | \boldsymbol{r} | W_{0n} \rangle|^2, \tag{3.26}$$

$$\Omega_{\mathrm{OD}} = \sum_{n} \sum_{m\neq n} \sum_{\boldsymbol{R}} |\langle W_{\boldsymbol{R}n} | \boldsymbol{r} | W_{0n} \rangle|^2. \tag{3.27}$$

The contributions Ω_{I}, Ω_{D} and Ω_{OD} are respectively independent from the gauge $U^{(\boldsymbol{k})}$, diagonal and off-diagonal with respect to band indices. The total spread to be minimized finally reads

$$\Omega[U^{(\boldsymbol{k})}] = \Omega_{\mathrm{I}}[U^{(\boldsymbol{k})}] + \Omega_{\mathrm{D}}[U^{(\boldsymbol{k})}] + \Omega_{\mathrm{OD}}[U^{(\boldsymbol{k})}]. \tag{3.28}$$

In order to obtain the gradient of the functional $\Omega[U^{(\boldsymbol{k})}]$, it is necessary to rewrite the expressions for the spread in a form that depends explicitly on the gauge $U^{(\boldsymbol{k})}$. This is achieved by rewriting the contributions to the spread in terms of the rotated Bloch states $\widetilde{\psi}_{n\boldsymbol{k}}(\boldsymbol{r}) = U^{(\boldsymbol{k})}_{nm}\, \psi_{m\boldsymbol{k}}(\boldsymbol{r})$ and their lattice periodic parts $\widetilde{u}_{n\boldsymbol{k}}(\boldsymbol{r}) = U^{(\boldsymbol{k})}_{nm}\, u_{m\boldsymbol{k}}(\boldsymbol{r})$.

The matrix elements of the position operator in the Wannier basis appear in Eqs. 3.25, 3.26 and 3.27. They have to be evaluated using Eq. 3.23, which yields the expression

$$\langle W_{\boldsymbol{R}n} |\, \boldsymbol{r}\, | W_{0n} \rangle = \left(\frac{V}{8\pi^3}\right)^2 \int\int d\boldsymbol{k}\, d\boldsymbol{k}'\; e^{i\boldsymbol{k}\cdot\boldsymbol{R}} \langle \widetilde{\psi}_{\boldsymbol{k}n} | \boldsymbol{r} | \widetilde{\psi}_{\boldsymbol{k}'m} \rangle. \tag{3.29}$$

The action of the position operator on a Bloch state $\widetilde{\psi}_{\boldsymbol{k}n}(\boldsymbol{r})$ can be reformulated in terms of a gradient in momentum space according to

$$\boldsymbol{r}\, \widetilde{\psi}_{\boldsymbol{k}n}(\boldsymbol{r}) = i\, e^{i\boldsymbol{k}\cdot\boldsymbol{r}}\, \nabla_{\boldsymbol{k}}\, \widetilde{u}_{n\boldsymbol{k}}(\boldsymbol{r}) - i\, \nabla_{\boldsymbol{k}}\, \widetilde{\psi}_{n\boldsymbol{k}}(\boldsymbol{r}), \tag{3.30}$$

which leads after a few lines of calculus to

$$\langle W_{\boldsymbol{R}n} |\, \boldsymbol{r}\, | W_{0n} \rangle = i \frac{V}{8\pi^3} \int d\boldsymbol{k}\; e^{i\boldsymbol{k}\cdot\boldsymbol{R}} \langle \widetilde{u}_{\boldsymbol{k}n} | \nabla_{\boldsymbol{k}} \widetilde{u}_{\boldsymbol{k}m} \rangle, \tag{3.31}$$

where the periodicity of the Bloch states in momentum space was used (see Ref. [35] for a derivation).

Similarly, we obtain the expectation value of the square of the position operator

$$\langle r^2 \rangle_n = \langle W_{0n} | r^2 | W_{0n} \rangle = \frac{V}{8\pi^3} \int d\boldsymbol{k}\; e^{i\boldsymbol{k}\cdot\boldsymbol{R}} |\nabla_{\boldsymbol{k}} | \widetilde{u}_{\boldsymbol{k}n} \rangle|^2. \tag{3.32}$$

by using the expression

$$r^2 \widetilde{\psi}_{\boldsymbol{k}n}(\boldsymbol{r}) = -2i\boldsymbol{r}\nabla_{\boldsymbol{k}} \widetilde{\psi}_{\boldsymbol{k}n}(\boldsymbol{r}) + \Delta_{\boldsymbol{k}} \widetilde{\psi}_{\boldsymbol{k}n}(\boldsymbol{r}) - e^{i\boldsymbol{k}\cdot\boldsymbol{r}} \Delta_{\boldsymbol{k}} \widetilde{u}_{\boldsymbol{k}n}(\boldsymbol{r}). \tag{3.33}$$

The spread can now be evaluated by inserting Eqs. 3.31 and 3.32 into Eqs. 3.25, 3.26 and 3.27. However, we first have to reformulate the previous expressions for the case of a discrete set of k-points. The following expressions have been derived in Ref [35]:

$$\langle \widetilde{u}_{\boldsymbol{k}n} | \nabla_{\boldsymbol{k}} \widetilde{u}_{\boldsymbol{k}m} \rangle = \sum_{\boldsymbol{b}} w_{\boldsymbol{b}} \, \boldsymbol{b} \, [\langle \widetilde{u}_{\boldsymbol{k}n} | \widetilde{u}_{\boldsymbol{k}+\boldsymbol{b}m} \rangle - \delta_{nm} \,], \tag{3.34}$$

$$|\nabla_{\boldsymbol{k}} | \widetilde{u}_{\boldsymbol{k}n} \rangle|^2 = \sum_{\boldsymbol{b}} w_{\boldsymbol{b}} \, [\, 2 - 2\mathrm{Re} \langle \widetilde{u}_{\boldsymbol{k}n} | \widetilde{u}_{\boldsymbol{k}+\boldsymbol{b}n} \rangle \,], \tag{3.35}$$

where $\boldsymbol{b}$ are vectors that connect two neighboring k-points in momentum space and $w_{\boldsymbol{b}}$ are the corresponding weights for the numerical integration. The spread evaluated from a discrete set of k-points are therefore given by the scalar products $\langle \widetilde{u}_{\boldsymbol{k}n} | \widetilde{u}_{\boldsymbol{k}+\boldsymbol{b}m} \rangle$, which can be used to define a set of matrices

$$M_{nm}^{(\boldsymbol{k},\boldsymbol{b})} = \langle \widetilde{u}_{\boldsymbol{k}n} | \widetilde{u}_{\boldsymbol{k}+\boldsymbol{b},m} \rangle. \tag{3.36}$$

The three contributions to the spread in terms of the $M^{(\boldsymbol{k},\boldsymbol{b})}$ matrices finally read

$$\Omega_{\mathrm{I}} = \frac{1}{N_k} \sum_{\boldsymbol{k}\boldsymbol{b}} w_{\boldsymbol{b}} \sum_n \Big\{ 1 - \sum_m |M_{mn}^{(\boldsymbol{k},\boldsymbol{b})}|^2 \Big\} \tag{3.37}$$

$$\Omega_{\mathrm{D}} = \frac{1}{N_k} \sum_{\boldsymbol{k}\boldsymbol{b}} w_{\boldsymbol{b}} \sum_n \Big[\mathrm{Im} \ln M_{nn}^{(\boldsymbol{k},\boldsymbol{b})} + \boldsymbol{b} \cdot \langle \boldsymbol{r} \rangle_n \Big] \tag{3.38}$$

$$\Omega_{\mathrm{OD}} = \frac{1}{N_k} \sum_{\boldsymbol{k}\boldsymbol{b}} w_{\boldsymbol{b}} \sum_n \sum_{m \neq n} |M_{mn}^{(\boldsymbol{k},\boldsymbol{b})}|^2, \tag{3.39}$$

with

$$\langle \boldsymbol{r} \rangle_n = -\frac{1}{N_k} \sum_{\boldsymbol{k}\boldsymbol{b}} w_{\boldsymbol{b}} \, \boldsymbol{b} \, \mathrm{Im} \ln M_{nn}^{(\boldsymbol{k},\boldsymbol{b})}. \tag{3.40}$$

The invariant and off-diagonal spread funcionals can be more conveniently summed up into one single contribution

$$\Omega_{\mathrm{I/OD}} = \Omega_{\mathrm{I}} + \Omega_{\mathrm{OD}} = \frac{1}{N_k} \sum_{\boldsymbol{k}\boldsymbol{b}} w_{\boldsymbol{b}} \sum_n \Big(1 - |M_{nn}^{(\boldsymbol{k},\boldsymbol{b})}|^2 \Big), \tag{3.41}$$

which involves only diagonal elements of the $M^{(\boldsymbol{k},\boldsymbol{b})}$ matrices.

The functional dependence of the spread functional $\Omega[U^{(\boldsymbol{k})}]$ is clear, because they depend only on the $M^{(\boldsymbol{k},\boldsymbol{b})}$ matrices (Eq. 3.36) defined by the scalar products of the rotated Bloch states (Eq. 3.21). The knowledge of the gradient of the functional would provide a systematic way of reducing the spread of the Wannier functions by an iterative steepest-descent algorithm.

Gradient of the spread functional

We want now to obtain an explicit expression for the gradient of the spread functional. For this let us consider an infinitesimal gauge transformation

$$U_{nm}^{(\boldsymbol{k})} = \delta_{nm} + dW_{nm}^{(\boldsymbol{k})}, \tag{3.42}$$

where $W^{(\boldsymbol{k})}$ is an anti-Hermitian matrix. Applying the infinitesimal gauge transformation to the Bloch states yields

$$|\widetilde{u}_{\boldsymbol{k}n}\rangle \to |\widetilde{u}_{\boldsymbol{k}n}\rangle + \sum_m dW_{mn}^{(\boldsymbol{k})}|\widetilde{u}_{\boldsymbol{k}n}\rangle. \tag{3.43}$$

The Eq. 3.43 can be used to compute the change of the $M^{(\boldsymbol{k},\boldsymbol{b})}$ matrices (Eq. 3.36) under the infinitesimal gauge transformation according to

$$M_{nn}^{(\boldsymbol{k},\boldsymbol{b})} \to \Big(\langle\widetilde{u}_{\boldsymbol{k}n}| + \sum_m (dW_{mn}^{(\boldsymbol{k})})^*\langle\widetilde{u}_{\boldsymbol{k}n}|\Big)\Big(|\widetilde{u}_{\boldsymbol{k}+\boldsymbol{b},n}\rangle + \sum_m |\widetilde{u}_{\boldsymbol{k}+\boldsymbol{b},n}\rangle dW_{mn}^{(\boldsymbol{k}+\boldsymbol{b})}\Big) \tag{3.44}$$

$$\approx \langle\widetilde{u}_{\boldsymbol{k}n}|\widetilde{u}_{\boldsymbol{k}+\boldsymbol{b},n}\rangle + \sum_m (-dW_{nm}^{(\boldsymbol{k})})\langle\widetilde{u}_{\boldsymbol{k}n}|\widetilde{u}_{\boldsymbol{k}+\boldsymbol{b},n}\rangle + \langle\widetilde{u}_{\boldsymbol{k}n}|\widetilde{u}_{\boldsymbol{k}+\boldsymbol{b},n}\rangle dW_{mn}^{(\boldsymbol{k}+\boldsymbol{b})} \tag{3.45}$$

$$= M_{nn}^{(\boldsymbol{k},\boldsymbol{b})} + dM_{nn}^{(\boldsymbol{k},\boldsymbol{b})}, \tag{3.46}$$

where the change of the $M^{(\boldsymbol{k},\boldsymbol{b})}$ matrices is defined by

$$dM_{nn}^{(\boldsymbol{k},\boldsymbol{b})} = -\Big[dW^{(\boldsymbol{k})}M^{(\boldsymbol{k},\boldsymbol{b})}\Big]_{nn} - \Big[dW^{(\boldsymbol{k}+\boldsymbol{b})}M^{(\boldsymbol{k}+\boldsymbol{b},-\boldsymbol{b})}\Big]_{nn}^*. \tag{3.47}$$

The equations 3.46 and 3.47 can be used along with Eq. 3.41 to obtain the change of the spread $\Omega_{\mathrm{I/OD}}$ when applying the gauge transformation (see Ref. [35] for a derivation)

$$d\Omega_{\mathrm{I/OD}} = \frac{4}{N_k}\sum_{\boldsymbol{k}\boldsymbol{b}} w_{\boldsymbol{b}}\mathrm{ReTr}\Big(dW^{(\boldsymbol{k})}R^{(\boldsymbol{k},\boldsymbol{b})}\Big), \tag{3.48}$$

where we have defined the matrix

$$R_{mn}^{(\boldsymbol{k},\boldsymbol{b})} = M_{mn}^{(\boldsymbol{k},\boldsymbol{b})}\,(M_{nn}^{(\boldsymbol{k},\boldsymbol{b})})^*. \tag{3.49}$$

In a similar way the change of the diagonal part of the spread functional Ω_{D} is given by

$$d\Omega_{\mathrm{D}} = -\frac{4}{N_k}\sum_{\boldsymbol{k}\boldsymbol{b}} w_{\boldsymbol{b}}\mathrm{ImTr}\Big(dW^{(\boldsymbol{k})}T^{(\boldsymbol{k},\boldsymbol{b})}\Big), \tag{3.50}$$

where we used the matrices

$$T_{mn}^{(\boldsymbol{k},\boldsymbol{b})} = \widetilde{R}_{mn}^{(\boldsymbol{k},\boldsymbol{b})}q_n^{(\boldsymbol{k},\boldsymbol{b})}, \tag{3.51}$$

$$q_n^{(\boldsymbol{k},\boldsymbol{b})} = \mathrm{Im}\ln M_{nn}^{(\boldsymbol{k},\boldsymbol{b})} + \boldsymbol{b}\cdot\langle\boldsymbol{r}\rangle_n, \tag{3.52}$$

$$\widetilde{R}_{mn}^{(\boldsymbol{k},\boldsymbol{b})} = \frac{M_{mn}^{(\boldsymbol{k},\boldsymbol{b})}}{M_{nn}^{(\boldsymbol{k},\boldsymbol{b})}}. \tag{3.53}$$

The gradient of the total spread functional follows from Eqs. 3.48 and 3.50 and is given by

$$G^{(\boldsymbol{k})} = \frac{d\Omega}{dW^{(\boldsymbol{k})}} = \frac{4}{N_k} \sum_{\boldsymbol{kb}} w_{\boldsymbol{b}} \Big[\mathcal{A}\Big(R^{(\boldsymbol{k},\boldsymbol{b})}\Big) - \mathcal{S}\Big(T^{(\boldsymbol{k},\boldsymbol{b})}\Big) \Big], \tag{3.54}$$

where we used the symmetrization and anti-symmetrization operators $\mathcal{S}(B) = (B + B^\dagger)/2i$ and $\mathcal{A}(B) = (B - B^\dagger)/2$.

3.3.3. Strategy for parallelization

The method discussed in the previous section for the minimization of the spread of the Wannier functions paves the way to the use of Wannier functions as a powerful interpolation technique. However, reaching convergence on a single CPU normally takes more time than the self-consistent calculation of the Kohn-Sham potential with an efficiently parallelized DFT code, so that the computation of the MLWFs constitutes a bottleneck in the computational workflow. In order to compute MLWFs of large systems in a reasonable amount of type, we have parallelized the WANNIER90 code using the message passing interface (MPI). We discuss in the following the parallelization strategy that has been used.

The minimization of the spread of the WFs is based on an iterative scheme. In each cycle the code starts by evaluating the gradient of the spread functional $G^{(\boldsymbol{k})}$ from which a small gauge transformation $dW^{(\boldsymbol{k})}$ is proposed. Then, the $U^{(\boldsymbol{k})}$ and $M^{(\boldsymbol{k},\boldsymbol{b})}$ matrices are updated and finally the corresponding spread Ω is evaluated. It turns out that the calculation of the new $U^{(\boldsymbol{k})}$ and $M^{(\boldsymbol{k},\boldsymbol{b})}$ matrices is by far the part that takes most time in the loop. Therefore, an efficient speedup of the program can be achieved by parallelization of the corresponding code section, as illustrated in Fig. 3.1.

We show in Fig. 3.2 a benchmark of the parallel code for a film calculation with 23 atoms per unit cell, 18 Wannier functions per atom and a 8×8 k-mesh. The computation time is almost entirely spent in the calculation of the $U^{(\boldsymbol{k})}$ and $M^{(\boldsymbol{k},\boldsymbol{b})}$ matrices when the code runs on a single CPU, which justifies the parallelization scheme described in Fig. 3.1. The time per cycle is drastically reduced by a factor of about 6, 8 and 10 when running respectively on 8, 16 and 32 nodes. The deviation from a perfect scaling is explained by the increase of the time spent in the communication between nodes and in the serial section. Since a few thousands of iterations are normally needed to converge the spread of the WFs, the parallelization of the code reduces the time of calculation from about a week to less than a day.

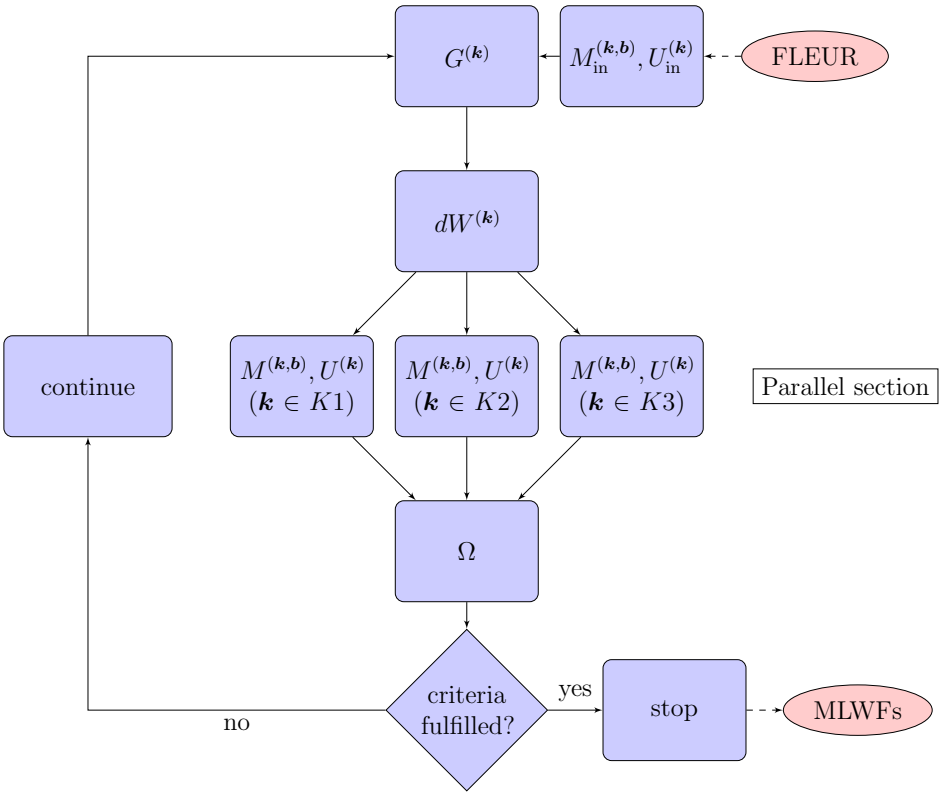

Figure 3.1.: Flowchart of the WANNIER90 programm [36] parallelized as part of this thesis. The parallel section includes the calculation of the $U^{(\boldsymbol{k})}$ and $M^{(\boldsymbol{k},\boldsymbol{b})}$ matrices, where the total set of k-vectors is split between n independent sets K_n distributed over n nodes ($n = 3$ is shown as an example). Once the parallel section ends, all $U^{(\boldsymbol{k})}$ and $M^{(\boldsymbol{k},\boldsymbol{b})}$ matrices are communicated to each node in order to compute the spread Ω.

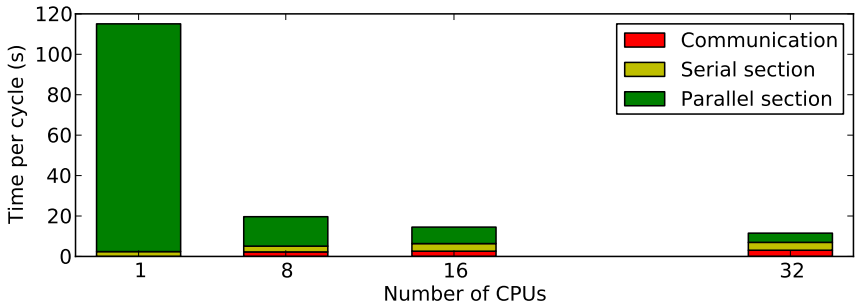

Figure 3.2.: Benchmark of the parallel WANNIER90 code for a film calculation with 23 atoms per unit cell, 18 Wannier functions per atom and a 8×8 k-mesh. The time per cycle of the iterative procedure for finding MLWFs is shown for 1, 8, 16 and 32 CPUs from the iff597 Jülich cluster. The parallel section corresponds to the calculation of the $U^{(\boldsymbol{k})}$ and $M^{(\boldsymbol{k},\boldsymbol{b})}$ matrices as shown in Fig. 3.1. The serial section corresponds to the calculation of $G^{(\boldsymbol{k})}$, $dW^{(\boldsymbol{k})}$ and Ω. The remaining part of the time is spent in the communication between nodes, i.e., to send and receive the different $U^{(\boldsymbol{k})}$ and $M^{(\boldsymbol{k},\boldsymbol{b})}$ matrices.

3.3.4. Wannier interpolation

The interpolated Bloch state for arbitrary wave vector $\widetilde{\boldsymbol{k}}$ can be obtained from the MLWFs $W_{n\boldsymbol{R}}(\boldsymbol{r})$ by inverse Fourier transform

$$\psi^{W}_{n\widetilde{\boldsymbol{k}}}(\boldsymbol{r}) = \sum_{|R_i|<R_i^c} e^{i\widetilde{\boldsymbol{k}}\cdot\boldsymbol{R}} W_{n\boldsymbol{R}}(\boldsymbol{r}), \tag{3.55}$$

where the sum over lattice vectors can be restricted to a small number of near lattice vectors within a range R_i^c because the Wannier functions we use are well localized. The interpolated Bloch states $\psi^{W}_{n\widetilde{\boldsymbol{k}}}(\boldsymbol{r})$ are in general not yet eigen states of the Hamiltonian since they belong to the Wannier gauge (W). A gauge transformation $V^{(\widetilde{\boldsymbol{k}})}$ is still needed to go back to the original *ab initio* gauge (see Eq. 3.20). The $V^{(\widetilde{\boldsymbol{k}})}$ matrices are defined as the ones that diagonalize the interpolated Hamiltonian operator $H(\widetilde{\boldsymbol{k}})$ and are closely related to the $U^{(\boldsymbol{k})}$ gauge transformation used earlier.

We focus now on the interpolation of the Hamiltonian $H(\boldsymbol{k})$ by the Wannier interpolation technique. We construct the matrix elements of the Hamiltonian in the

basis of the interpolated Bloch states by

$$\begin{aligned}\langle\psi^W_{n\widetilde{\boldsymbol{k}}}|H|\psi^W_{m\widetilde{\boldsymbol{k}}'}\rangle &= \sum_{|R_i|,|R_i|<R_i^c} e^{-i\widetilde{\boldsymbol{k}}\cdot\boldsymbol{R}}\, e^{i\widetilde{\boldsymbol{k}}'\cdot\boldsymbol{R}'}\langle W_{n\boldsymbol{R}}|H|W_{m\boldsymbol{R}'}\rangle \\ &= \sum_{|R_i|,|R_i|<R_i^c} e^{-i\widetilde{\boldsymbol{k}}\cdot\boldsymbol{R}}\, e^{i\widetilde{\boldsymbol{k}}'\cdot\boldsymbol{R}'}\langle W_{n0}|H|W_{m\boldsymbol{R}'-\boldsymbol{R}}\rangle \\ &= \sum_{|\Delta R_i|,|\mathcal{R}_i|<R_i^c} e^{i(\widetilde{\boldsymbol{k}}'-\widetilde{\boldsymbol{k}})\cdot\boldsymbol{\mathcal{R}}}\, e^{i(\widetilde{\boldsymbol{k}}'+\widetilde{\boldsymbol{k}})\cdot\frac{\Delta\boldsymbol{R}}{2}}\langle W_{n0}|H|W_{m\Delta\boldsymbol{R}}\rangle \\ &= N\delta_{\widetilde{\boldsymbol{k}}\widetilde{\boldsymbol{k}}'}\sum_{|\Delta R_i|<R_i^c} e^{i\widetilde{\boldsymbol{k}}\cdot\Delta\boldsymbol{R}}\langle W_{n0}|H|W_{m\Delta\boldsymbol{R}}\rangle,\end{aligned} \tag{3.56}$$

where N is the number lattice vectors on which the sums run and we have used the notations $\Delta\boldsymbol{R} = \boldsymbol{R}' - \boldsymbol{R}$ and $\boldsymbol{\mathcal{R}} = (\boldsymbol{R}' + \boldsymbol{R})/2$. As expected the Hamiltonian is diagonal with respect to $\widetilde{\boldsymbol{k}}$ also in the Wannier gauge and can therefore be written as

$$H^W_{nm}(\widetilde{\boldsymbol{k}}) = N\sum_{|\Delta R_i|<R_i^c} e^{i\widetilde{\boldsymbol{k}}\cdot\Delta\boldsymbol{R}}\langle W_{n0}|H|W_{m\Delta\boldsymbol{R}}\rangle \tag{3.57}$$

Finally, the Hamiltonian obtained from Eq. 3.57 can be diagonalized using the suitable rotation matrix $V^{(\widetilde{\boldsymbol{k}})}$, i.e.,

$$H^H_{nm}(\widetilde{\boldsymbol{k}}) = \left[[V^{(\widetilde{\boldsymbol{k}})}]^\dagger\, H^W(\widetilde{\boldsymbol{k}})\, V^{(\widetilde{\boldsymbol{k}})}\right]_{nm} = \varepsilon_n(\widetilde{\boldsymbol{k}})\,\delta_{nm}, \tag{3.58}$$

which yields the interpolated band structure $\varepsilon_n(\widetilde{\boldsymbol{k}})$.

In a similar way we obtain in the Wannier gauge the matrix elements of the velocity operators

$$v^W_{j,nm}(\widetilde{\boldsymbol{k}}) = \langle\widetilde{\psi}_{n\widetilde{\boldsymbol{k}}}|v_j|\widetilde{\psi}_{m\widetilde{\boldsymbol{k}}}\rangle = N\sum_{|\Delta R_i|<R_i^c} i\Delta R_j e^{i\widetilde{\boldsymbol{k}}\cdot\Delta\boldsymbol{R}}\langle W_{n0}|H|W_{m\Delta\boldsymbol{R}}\rangle \tag{3.59}$$

and of the torque operator

$$T^W_{i,nm}(\widetilde{\boldsymbol{k}}) = \langle\widetilde{\psi}_{n\widetilde{\boldsymbol{k}}}|\mathcal{T}_i|\widetilde{\psi}_{m\widetilde{\boldsymbol{k}}}\rangle = N\sum_{|\Delta R_i|<R_i^c} e^{i\widetilde{\boldsymbol{k}}\cdot\Delta\boldsymbol{R}}\langle W_{n0}|\mathcal{T}_i|W_{m\Delta\boldsymbol{R}}\rangle, \tag{3.60}$$

where the torque operator is defined by Eq. 2.12. Both operators can be rotated back to the *ab initio* gauge according to

$$v^H_{j,nm}(\widetilde{\boldsymbol{k}}) = \left[[V^{(\widetilde{\boldsymbol{k}})}]^\dagger\, v^W_j(\widetilde{\boldsymbol{k}})\, V^{(\widetilde{\boldsymbol{k}})}\right]_{nm} \tag{3.61}$$

and

$$T^H_{i,nm}(\widetilde{\boldsymbol{k}}) = \left[[V^{(\widetilde{\boldsymbol{k}})}]^\dagger\, T^W_i(\widetilde{\boldsymbol{k}})\, V^{(\widetilde{\boldsymbol{k}})}\right]_{nm}. \tag{3.62}$$

Therefore, the Wannier interpolation technique provides a very efficient way of computing the matrix elements $v^H_{j,nm}(\widetilde{\boldsymbol{k}})$ and $T^H_{i,nm}(\widetilde{\boldsymbol{k}})$, as well as the band energie $\varepsilon_n(\widetilde{\boldsymbol{k}})$, for arbitrary $\widetilde{\boldsymbol{k}}$-points. This is used in the next section for the evaluation of the Kubo formula for the torque.

3.4. Kubo formalism

We discuss in the following the implementation of the Kubo formula for the torque (Eq. 2.11) within the FLAPW method. We use the constant band broadening model for disorder that was introduced in Section 2.3. The Green functions and their derivatives for a band broadening Γ are given in the spectral representation by

$$G^{\mathrm{R}}_{\boldsymbol{k}}(\varepsilon) = \hbar \sum_m \frac{|\psi_{m\boldsymbol{k}}\rangle\langle\psi_{m\boldsymbol{k}}|}{\varepsilon - \varepsilon_m(\boldsymbol{k}) + i\Gamma}, \tag{3.63}$$

$$\frac{dG^{\mathrm{R}}_{\boldsymbol{k}}(\varepsilon)}{d\varepsilon} = -\hbar \sum_m \frac{|\psi_{m\boldsymbol{k}}\rangle\langle\psi_{m\boldsymbol{k}}|}{(\varepsilon - \varepsilon_m(\boldsymbol{k}) + i\Gamma)^2}, \tag{3.64}$$

$$G^{\mathrm{A}}_{\boldsymbol{k}}(\varepsilon) = \hbar \sum_m \frac{|\psi_{m\boldsymbol{k}}\rangle\langle\psi_{m\boldsymbol{k}}|}{\varepsilon - \varepsilon_m(\boldsymbol{k}) - i\Gamma}, \tag{3.65}$$

$$\frac{dG^{\mathrm{A}}_{\boldsymbol{k}}(\varepsilon)}{d\varepsilon} = -\hbar \sum_m \frac{|\psi_{m\boldsymbol{k}}\rangle\langle\psi_{m\boldsymbol{k}}|}{(\varepsilon - \varepsilon_m(\boldsymbol{k}) - i\Gamma)^2}. \tag{3.66}$$

The index m runs in principle over all eigen states. However, the number of states is defined in practice by the number of Wannier functions, which needs to be chosen sufficiently large in order to converge the torque calculation. Inserting the previous expressions into Eq. 2.11 yields for the three terms of the torkance tensor:

$$\begin{aligned}
t^{\mathrm{I(a)}}_{ij} &= -\frac{e}{hN_k}\int_{-\infty}^{\infty} d\varepsilon \frac{df(\varepsilon)}{d\varepsilon} \sum_{\boldsymbol{k}}\sum_{mn} \frac{\langle\psi_{n\boldsymbol{k}}|\mathcal{T}_i|\psi_{m\boldsymbol{k}}\rangle\langle\psi_{m\boldsymbol{k}}|v_j|\psi_{n\boldsymbol{k}}\rangle}{(\varepsilon - \varepsilon_m(\boldsymbol{k}) + i\Gamma)(\varepsilon - \varepsilon_n(\boldsymbol{k}) - i\Gamma)}, \\
t^{\mathrm{I(b)}}_{ij} &= \frac{e}{hN_k}\int_{-\infty}^{\infty} d\varepsilon \frac{df(\varepsilon)}{d\varepsilon} \sum_{\boldsymbol{k}}\sum_{mn} \frac{\mathrm{Re}[\langle\psi_{n\boldsymbol{k}}|\mathcal{T}_i|\psi_{m\boldsymbol{k}}\rangle\langle\psi_{m\boldsymbol{k}}|v_j|\psi_{n\boldsymbol{k}}\rangle]}{(\varepsilon - \varepsilon_m(\boldsymbol{k}) + i\Gamma)(\varepsilon - \varepsilon_n(\boldsymbol{k}) + i\Gamma)} \\
t^{\mathrm{II}}_{ij} &= \frac{e}{hN_k}\int_{-\infty}^{\infty} d\varepsilon f(\varepsilon) \sum_{\boldsymbol{k}}\sum_{mn} \frac{\mathrm{Re}[\langle\psi_{n\boldsymbol{k}}|\mathcal{T}_i|\psi_{m\boldsymbol{k}}\rangle\langle\psi_{m\boldsymbol{k}}|v_j|\psi_{n\boldsymbol{k}}\rangle]}{(\varepsilon - \varepsilon_m(\boldsymbol{k}) + i\Gamma)(\varepsilon - \varepsilon_n(\boldsymbol{k}) + i\Gamma)^2} \\
&\qquad - \frac{\mathrm{Re}[\langle\psi_{n\boldsymbol{k}}|\mathcal{T}_i|\psi_{m\boldsymbol{k}}\rangle\langle\psi_{m\boldsymbol{k}}|v_j|\psi_{n\boldsymbol{k}}\rangle]}{(\varepsilon - \varepsilon_m(\boldsymbol{k}) + i\Gamma)^2(\varepsilon - \varepsilon_n(\boldsymbol{k}) + i\Gamma)^2}.
\end{aligned} \tag{3.67}$$

Using Eq. 3.67 one can derive explicit equations for the parts of the torkance that are respectively even and odd with respect to magnetization direction:

$$
\begin{aligned}
t_{ij}^{\text{even}} = \frac{e\hbar}{2\pi N_k} \sum_{\boldsymbol{k}} \sum_{n\neq m} \operatorname{Im}\left[\langle\psi_{\boldsymbol{k}n}|\mathcal{T}_i|\psi_{\boldsymbol{k}m}\rangle\langle\psi_{\boldsymbol{k}m}|v_j|\psi_{\boldsymbol{k}n}\rangle\right] \Bigg\{ & \\
& \frac{\Gamma(\varepsilon_{\boldsymbol{k}m}-\varepsilon_{\boldsymbol{k}n})}{\left[(\varepsilon_{\text{F}}-\varepsilon_{\boldsymbol{k}n})^2+\Gamma^2\right]\left[(\varepsilon_{\text{F}}-\varepsilon_{\boldsymbol{k}m})^2+\Gamma^2\right]} \\
& + \frac{2\Gamma}{\left[\varepsilon_{\boldsymbol{k}n}-\varepsilon_{\boldsymbol{k}m}\right]\left[(\varepsilon_{\text{F}}-\varepsilon_{\boldsymbol{k}m})^2+\Gamma^2\right]} \\
& + \frac{2}{\left[\varepsilon_{\boldsymbol{k}n}-\varepsilon_{\boldsymbol{k}m}\right]^2} \operatorname{Im}\ln\frac{\varepsilon_{\boldsymbol{k}m}-\varepsilon_{\text{F}}-i\Gamma}{\varepsilon_{\boldsymbol{k}n}-\varepsilon_{\text{F}}-i\Gamma}\Bigg\},
\end{aligned}
\tag{3.68}
$$

$$
t_{ij}^{\text{odd}} = \frac{e\hbar}{\pi N_k} \sum_{\boldsymbol{k}} \sum_{nm} \frac{\Gamma^2 \operatorname{Re}\left[\langle\psi_{\boldsymbol{k}n}|\mathcal{T}_i|\psi_{\boldsymbol{k}m}\rangle\langle\psi_{\boldsymbol{k}m}|v_j|\psi_{\boldsymbol{k}n}\rangle\right]}{\left[(\varepsilon_{\text{F}}-\varepsilon_{\boldsymbol{k}n})^2+\Gamma^2\right]\left[(\varepsilon_{\text{F}}-\varepsilon_{\boldsymbol{k}m})^2+\Gamma^2\right]}. \tag{3.69}
$$

The interpretation of t_{ij}^{even} and t_{ij}^{odd} in the limit $\Gamma \to 0$ has been discussed in Section 2.3.

4 Impurity-driven SOTs in the KKR method

Most *ab initio* calculations of SOTs in ferromagnetic bilayers are based on the constant relaxation time approximation [19, 39–41]. While the importance of impurity scattering is well known in the field of charge and spin transport [42–48], the interplay between different types of disorder and current-induced SOTs in ferromagnetic heterostructures is essentially unexplored. Nonetheless, the crucial role of surfaces and interfaces giving rise to the spin accumulation suggests an enhanced sensitivity of the spin-orbit torque to structural and chemical types of disorder in these regions. This line of thought is supported by the large effect of annealing on the SOTs in AlO_x/Co/Pt and MgO/CoFeB/Ta thin films [49, 50]. This calls for a first principles theory of SOT that is able to account for an effect of specific types of defects and impurities, especially close to interfaces.

In this section, we present an implementation of *ab initio* Boltzmann formalism for the spin-orbit torque based on the Korringa-Kohn-Rostoker (KKR) Green function method, which is ideally suited for studying the effect of impurity scattering on the SOT. The main features of the formalism have been published in Ref. [51] and we give here a more detailed view of the underlying theory. We first give a short introduction to Green functions in condensed matter physics. We then present the KKR formalism, which we use to compute the electronic structure and investigate the scattering properties off impurities. Next, we discuss the implementation of the torque and spin flux operators in KKR, which is a central result of this thesis. Finally, we show how the impurity-driven spin-orbit torque can be computed within the Boltzmann formalism.

4.1. Green functions in physics

A central aim of solid states physics is to predict the expectation values of physical observables in systems in equilibrium and driven out of equilibrium by an external perturbation. The expectation value of an arbitrary observable $\mathcal{O}$ can be computed based on the Kohn-Sham eigen states using Eq. 3.12. Alternatively, one can first compute the Green function $G(\boldsymbol{r}, \boldsymbol{r'}, \varepsilon)$ of the Kohn-Sham equation defined by

$$\Big[-\frac{\hbar^2}{2m}\nabla_{\boldsymbol{r}}^2 + v_{\text{eff}}(\boldsymbol{r}) - \varepsilon \Big] G(\boldsymbol{r}, \boldsymbol{r'}, \varepsilon) = -\delta(\boldsymbol{r} - \boldsymbol{r'}) \tag{4.1}$$

and then obtain the expectation values by integration over energies:

$$\langle \mathcal{O} \rangle = -\frac{1}{\pi} \mathrm{Im} \int d\varepsilon \; \theta(\varepsilon_{\mathrm{F}} - \varepsilon) \int \int d\boldsymbol{r} d\boldsymbol{r'} \; G(\boldsymbol{r}, \boldsymbol{r'}, \varepsilon) \mathcal{O}(\boldsymbol{r'}, \boldsymbol{r}). \tag{4.2}$$

The Green function can be obtained in two different ways. The first one is to make use of the spectral representation of the Green function

$$G(\boldsymbol{r}, \boldsymbol{r'}, \varepsilon) = \sum_i \frac{\psi_i(\boldsymbol{r}) \psi_i^*(\boldsymbol{r'})}{\varepsilon - \varepsilon_i}, \tag{4.3}$$

where the index i runs over all eigen states. This requires the knowledge of the eigen functions, i.e., one first needs to solve Eq. 3.6. Another possibility is to make use of the Dyson equation

$$G(\boldsymbol{r}, \boldsymbol{r'}, \varepsilon) = G_0(\boldsymbol{r}, \boldsymbol{r'}, \varepsilon) + \int d\boldsymbol{r''} \; G_0(\boldsymbol{r}, \boldsymbol{r''}, \varepsilon) \Delta V(\boldsymbol{r''}) G(\boldsymbol{r''}, \boldsymbol{r'}, \varepsilon), \tag{4.4}$$

where G_0 is the Green function of a reference system and $\Delta V(\boldsymbol{r}) = v_{\mathrm{eff}}(\boldsymbol{r}) - v_0(\boldsymbol{r})$ is the difference between the Kohn-Sham potential (Eq. 3.9) and the potential of the reference system.

One advantage of using the Dyson equation instead of the spectral representation is that it can be used to obtain the Green function of an impurity embedded in an otherwise periodic host. In fact, determining the eigen functions and the eigen energies used in Eq. 4.3 is possible only for a purely periodic system, by making use of the Bloch theorem, or for a system of finite range, such as an isolated molecule. Beside this flexibility, using the Dyson equation can also be computationally more efficient if the Green function is needed at a single energy only. This is clearly the case when one investigates the effect of impurity scattering, where the Green function at the Fermi energy determines the transport properties.

4.2. KKR method

The KKR method aims at computing the electronic structure of solids using the multiple scattering theory [52, 53]. Within multiple scattering theory the problem of finding stationary solutions to the Schrödinger equation is separated into two parts. First, one computes the scattering properties of individual atomic potentials. Second, one enforces the incident wave at each scattering site to be equal to the sum of the outgoing waves from all other sites. This yields a very elegant way of determining the stationary solutions where the scattering properties of individual atoms are separated from the geometrical properties of the crystal, e.g., from the lattice type.

Because the separation of the local properties of individual atomic potentials and the geometrical properties of the crystal was realized to be an efficient method for

computing the Green function of the solid, the KKR method was reformulated in terms of Green functions [54–57]. Within this formalism the Green function is explicitly written as the sum of a single-site part, which can be computed for isolated atoms, and a multiple scattering part which accounts for all possible series of scattering events in the crystal. Using the Green function KKR formalism, the stationary solutions of the Schrödinger equation are no longer required to compute expectation values of physical observables, since the Green function already contains all the information of the system. This makes in particular the calculation of the charge density very efficient for self-consistent DFT calculations.

Because the KKR method is based on multiple-scattering theory, the scattering properties of impurities can be computed on the very same footing as the properties of the host. This makes it perfectly suitable to determine the transition rates and the relaxation times of the electronic states in the presence of impurities, which allows us to investigate the transport properties of disordered systems beyond the constant relaxation time approximation. This stands in sharp contrast to the case of the FLAPW method, where there is no obvious way to go beyond purely periodic systems.

4.2.1. Voronoi construction

In the KKR formalism the space is decomposed into atomic cells centered at the nuclei. They are found by a Voronoi construction, which assigns each point of space to a given atomic cell[1]. The aim of this space decomposition is to separate the calculation of the Green function of the crystal into two parts. First, one considers a set of local problems defined within each individual atomic cell (see section 4.2.2), which can be solved independently. Second, one connects the solutions of all atomic problems to obtain the full Green function of the crystal (see section 4.2.3). This separation is made possible by the decomposition of the globally defined real space vector $\boldsymbol{x}$ as

$$\boldsymbol{x} = \boldsymbol{R}_n + \boldsymbol{r}, \tag{4.5}$$

where $\boldsymbol{R}_n$ is a global vector pointing to the center of cell n and $\boldsymbol{r}$ a local vector defined only within the cell n. The Voronoi construction of the atomic cells and the system of coordinates are illustrated in Fig. 4.2.1.

Following the same philosophy the (Kohn-Sham) potential is divided into local cell-dependent potentials:

$$V(\boldsymbol{x}) = \sum_n V^n(\boldsymbol{x} - \boldsymbol{R}_n), \qquad V^n(\boldsymbol{r}) = \begin{cases} V(\boldsymbol{R}_n + \boldsymbol{r}) & \text{if } \boldsymbol{R}_n + \boldsymbol{r} \in \text{cell } n \\ 0 & \text{otherwise.} \end{cases} \tag{4.6}$$

The local potentials are then expanded into real spherical harmonics:

$$V^n(\boldsymbol{r}) = \sum_L V_L^n(r) Y_L(\hat{\boldsymbol{r}}), \tag{4.7}$$

[1] We use in this thesis the so-called Wiegner-Seitz cells, where each point of space is assigned to the cell of the closest atom.

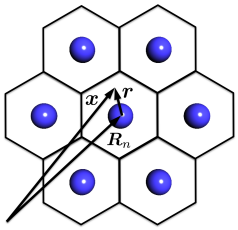

Figure 4.1.: Illustration of the atomic cells (black lines) found by the Voronoi construction and system of coordinates used in the KKR formalism. The vector $\boldsymbol{x}$ is a globally defined real space vector while the vector $\boldsymbol{r}$ is defined relatively to the position $\boldsymbol{R}_n$ of cell n. The atoms of the crystal are shown in blue.

where the variables $r = |\boldsymbol{r}|$ and $\hat{\boldsymbol{r}} = \boldsymbol{r}/r$ are respectively the magnitude and the direction of $\boldsymbol{r}$.

The regular scattering solutions of single atomic potentials (see Section 4.2.2) are expanded in a similar way:

$$R_L^n(\boldsymbol{r}, \varepsilon) = \sum_{L'} \frac{1}{r} R_{L'L}^n(r, \varepsilon) Y_{L'}(\hat{\boldsymbol{r}}). \tag{4.8}$$

In the KKR formalism the potential and the regular scattering solutions enter in various integrals where the domain of integration has to be restricted to the volume of a given atomic cell. This is for example the case when one computes the KKR representation of the torque operator, see Section 4.3. A very elegant way to restrict the integral to the volume of a given cell is to define for each cell the shape function

$$\theta^n(\boldsymbol{r}) = \begin{cases} 1 & \text{if } \boldsymbol{R}_n + \boldsymbol{r} \in \text{cell } n \\ 0 & \text{otherwise.} \end{cases} \tag{4.9}$$

The shape functions can be expanded into real spherical harmonics:

$$\theta^n(\boldsymbol{r}) = \sum_L \theta_L^n(r) Y_L(\hat{\boldsymbol{r}}). \tag{4.10}$$

The integration of a locally defined function $U^n(\boldsymbol{r}) = \sum_L U_L^n(r) Y_L(\hat{\boldsymbol{r}})$ can be easily restricted to the volume of the cell if one replaces the function by the product

$$u(\boldsymbol{r}) = U(\boldsymbol{r})\theta^n(\boldsymbol{r}) \quad = \sum_{LL'L''} C_{LL'L''} U_L^n(r) \theta_L^n(r) Y_{L''}(\hat{\boldsymbol{r}}), \tag{4.11}$$

where we have used the Gaunt coefficients

$$C_{LL'L''} = \int d\Omega \; Y_L(\hat{r}) Y_{L'}(\hat{r}) Y_{L''}(\hat{r}). \tag{4.12}$$

4.2.2. Single-site Green function

Following the idea of Eq. 4.4, we aim at finding the single-site Green function from the Green function of a reference system (here of free space). However, we will take a

slightly different route than a direct use of the Dyson equation, and will make use of the Lippmann-Schwinger equation instead. This is motivated by the fact that the so-called scattering solutions yielded by the Lippmann-Schwinger equation provide a simple expansion of the single-site Green function and are also used later to obtain the full Green function of the crystal.

Expansion of the Green function of free space

In this section we remind the expressions of the eigen functions and Green function of free electrons in spherical coordinates, which are used later on to compute the scattering solutions of single atomic potentials. The eigen functions of free space are given by

$$\begin{aligned}\varphi_{\boldsymbol{k}}(\boldsymbol{r}) &= e^{i\boldsymbol{k}\cdot\boldsymbol{r}} \\ &= \sum_L 4\pi i^l j_l(\kappa r) Y_L(\hat{\boldsymbol{r}}) Y_L(\hat{\boldsymbol{k}}),\end{aligned} \tag{4.13}$$

where $j_l(\kappa r)$ are the spherical Bessel functions, $Y_L(\hat{\boldsymbol{r}})$ the real spherical harmonics and $\kappa = \sqrt{\varepsilon}$. We have used a combined index $L = \{l, m\}$ for azimuthal quantum number l and magnetic quantum number m.

The Green function of free space is known analytically and is given by

$$\begin{aligned}g(\boldsymbol{r}, \boldsymbol{r'}, \varepsilon) &= -\frac{e^{i\kappa|\boldsymbol{r}-\boldsymbol{r'}|}}{4\pi|\boldsymbol{r}-\boldsymbol{r'}|} \\ &= \sum_L Y_L(\hat{\boldsymbol{r}}) \frac{1}{rr'} g_l(\boldsymbol{r}, \boldsymbol{r'}, \varepsilon) Y_L(\hat{\boldsymbol{r'}}),\end{aligned} \tag{4.14}$$

where the expansion coefficients

$$g_l(\boldsymbol{r}, \boldsymbol{r'}, \varepsilon) = \kappa r r' [\theta(r'-r) j_l(\kappa r) h_l(\kappa r') + \theta(r-r') h_l(\kappa r) j_l(\kappa r')] \tag{4.15}$$

are given by the spherical Bessel functions $j_l(\kappa r)$ and the spherical Hankel functions $h_l(\kappa r)$. We use in this work the definition $h_l(\kappa r) = n_l(\kappa r) - i j_l(\kappa r)$ for the Hankel function, where $n_l(\kappa r)$ is the Neumann function.

Expansion of the Green function of a finite range atomic potential

Let us now consider the problem of a finite range atomic potential $V(\boldsymbol{r})$ embedded in free space. The eigen functions of the corresponding Hamiltonian are obtained from the solutions in free space (Eq. 4.13) using the Lippmann-Schwinger equation:

$$\psi^s_{\boldsymbol{k}}(\boldsymbol{r}) = e^{i\boldsymbol{k}\cdot\boldsymbol{r}} \chi^s + \int d\boldsymbol{r'}\ g(\boldsymbol{r}, \boldsymbol{r'}, \varepsilon_k) V(\boldsymbol{r'}) \psi^s_{\boldsymbol{k}}(\boldsymbol{r'}), \tag{4.16}$$

where $\varepsilon_{\boldsymbol{k}} = \hbar^2 k^2 / 2m$ is the energy of a free particle of wave vector $\boldsymbol{k}$ and χ^s is a spin state with spin quantum number s.

The eigen functions computed from Eq. 4.16 are the sum of an incoming plane wave (first term) and a scattered wave (second term). They inherit a $\boldsymbol{k}$ index from the corresponding wavefunction of free space but are neither pure plane waves nor eigen states of the momentum operator. Similarly, they inherit a s index but are not pure spin states if the effect of spin-orbit coupling is included in the scattering potential $V(\boldsymbol{r})$.

Proceeding in the same way as in the case of free space (Eq. 4.13), the dependence of the wavefunctions on the wave vector $\boldsymbol{k}$ can be expanded in real spherical harmonics:

$$\psi^s_{\boldsymbol{k}}(\boldsymbol{r}) = \sum_L 4\pi i^l R^s_L(\boldsymbol{r}, \varepsilon_k) Y_L(\hat{\boldsymbol{k}}), \tag{4.17}$$

where $R^s_L(\boldsymbol{r}, \varepsilon_{\boldsymbol{k}})$ depends on the norm of the wave vector k via the energy parameter $\varepsilon_{\boldsymbol{k}} = \hbar^2 k^2/2m$.

Inserting Eqs. 4.13 and 4.17 into Eq. 4.16 yields a new Lippmann-Schwinger equation for each L-component of the wavefunctions:

$$R^s_L(\boldsymbol{r}, \varepsilon) = j_l(\kappa r) Y_L(\hat{\boldsymbol{r}}) \chi^s + \int d\boldsymbol{r'}\ g(\boldsymbol{r}, \boldsymbol{r'}, \varepsilon_k) V(\boldsymbol{r'}) R^s_L(\boldsymbol{r'}, \varepsilon). \tag{4.18}$$

Because $j_l(\kappa r) Y_L(\hat{\boldsymbol{r}}) \chi^s$ are eigen states of the free-space Hamiltonian, it is clear that the scattering solutions $R^s_L(\boldsymbol{r}, \varepsilon)$ are also eigen states of the perturbed Hamiltonian but differ from $\psi^s_{\boldsymbol{k}}(\boldsymbol{r})$ by the incoming boundary conditions. The scattering solutions $R^s_L(\boldsymbol{r}, \varepsilon)$ are intensively used in the KKR formalism because they provide a very elegant expansion of the Green function[2]:

$$G_s(\boldsymbol{r}, \boldsymbol{r'}, \varepsilon) = \kappa \sum_L [\theta(r' - r) R_L(\boldsymbol{r}) \bar{S}_L(\boldsymbol{r'}) + \theta(r - r') S_L(\boldsymbol{r}) \bar{R}_L(\boldsymbol{r'})]. \tag{4.19}$$

Both the regular and irregular scattering solutions are needed for the expansion of the Green function in Eq. 4.19. The irregular scattering solutions $S_L(\boldsymbol{r})$ are defined by

$$S^s_L(\boldsymbol{r}, \varepsilon) = \sum_{L'} h_{l'}(\kappa r) Y_{L'}(\hat{\boldsymbol{r}}) \beta^s_{LL'}(\varepsilon) + \int d\boldsymbol{r'}\ g(\boldsymbol{r}, \boldsymbol{r'}, \varepsilon_k) V(\boldsymbol{r'}) S^s_L(\boldsymbol{r'}, \varepsilon) \tag{4.20}$$

with

$$\beta^s_{LL'}(\varepsilon) = \delta_{L,L'} \chi^s - \kappa \int d\boldsymbol{r}\ j_l(\kappa r) Y_L(\boldsymbol{r}) V(\boldsymbol{r}) S^s_{L'}(\boldsymbol{r}, \varepsilon). \tag{4.21}$$

These expressions ensures that the irregular scattering solutions correspond to the Hankel functions (solutions of free space) outside the scattering region, as demonstrated by Drittler [58]. This in turn ensures that the Green function computed using

[2]The eigen functions $\psi^s_{\boldsymbol{k}}(\boldsymbol{r})$ are useful to determine the transition rates induced by a scattering potential from a state $\boldsymbol{k}$ to a state $\boldsymbol{k'}$. An equation similar to Eq. 4.16 is actually used in Section 4.2.5 to compute the transition rates induced by impurities in an otherwise periodic crystal.

Eq. 4.19 has the good boundary conditions.

The regular and irregular scattering solutions as defined by Eqs. 4.18 and 4.20 are called *right solutions*. Also the *left solutions* are required to compute the Green function according to Eq. 4.19, as explained in Ref. [59]. They are defined by the expressions

$$\bar{R}^s_L(\boldsymbol{r},\varepsilon) = \chi^s j_l(\kappa r) Y_L(\hat{\boldsymbol{r}}) + \int d\boldsymbol{r'}\ \bar{R}^s_L(\boldsymbol{r'},\varepsilon) V(\boldsymbol{r'}) g(\boldsymbol{r'},\boldsymbol{r},\varepsilon_k), \tag{4.22}$$

$$\bar{S}^s_L(\boldsymbol{r},\varepsilon) = \sum_{L'} \bar{\beta}^s_{LL'}(\varepsilon) h_{l'}(\kappa r) Y_{L'}(\hat{\boldsymbol{r}}) + \int d\boldsymbol{r'}\ \bar{S}^s_L(\boldsymbol{r'},\varepsilon) V(\boldsymbol{r'}) g(\boldsymbol{r'},\boldsymbol{r},\varepsilon_k) \tag{4.23}$$

and

$$\bar{\beta}^s_{LL'}(\varepsilon) = \delta_{L,L'}\chi^s - \kappa \int d\boldsymbol{r}\ \bar{R}^s_{L'}(\boldsymbol{r},\varepsilon) V(\boldsymbol{r}) h_l(\kappa r) Y_L(\boldsymbol{r}). \tag{4.24}$$

All scattering solutions are expanded in real spherical harmonics according to

$$R^s_L(\boldsymbol{r},\varepsilon) = \sum_{L'} \frac{1}{r} R^s_{L'L}(r,\varepsilon) Y_{L'}(\hat{\boldsymbol{r}}) \tag{4.25}$$

and

$$\bar{R}^s_L(\boldsymbol{r},\varepsilon) = \sum_{L'} \frac{1}{r} \bar{R}^s_{LL'}(r,\varepsilon) Y_{L'}(\hat{\boldsymbol{r}}) \tag{4.26}$$

and similarly for $S^s_L(\boldsymbol{r},\varepsilon)$ and $\bar{S}^s_L(\boldsymbol{r},\varepsilon)$. The corresponding expansion coefficients are obtained by

$$R^s_{L'L}(r,\varepsilon) = J_L(r,\varepsilon)\delta_{L',L}\ \chi^s + \int dr''\ g_{l'}(r,r'',\varepsilon) V_{L'L''}(r'') R^s_{L''L}(r'',\varepsilon) \tag{4.27}$$

$$\bar{R}^s_{LL'}(r,\varepsilon) = \delta_{L',L}\ \chi^s J_L(r,\varepsilon) + \int dr''\ \bar{R}^s_{LL''}(r'',\varepsilon) V_{L''L'}(r'') g_{l'}(r'',r,\varepsilon) \tag{4.28}$$

$$S^s_{L'L}(r,\varepsilon) = H_L(r,\varepsilon)\delta_{L',L}\ \chi^s + \int dr''\ g_{l'}(r,r'',\varepsilon) V_{L'L''}(r'') S^s_{L''L}(r'',\varepsilon) \tag{4.29}$$

$$\bar{S}^s_{LL'}(r,\varepsilon) = \delta_{L',L}\ \chi^s H_L(r,\varepsilon) + \int dr''\ \bar{S}^s_{LL''}(r'',\varepsilon) V_{L''L'}(r'') g_{l'}(r'',r,\varepsilon) \tag{4.30}$$

where we have introduced the notations $J_L(r,\varepsilon) = r j_l(\kappa r)$ and $H_L(r,\varepsilon) = r h_l(\kappa r)$ with $\kappa = \sqrt{\varepsilon}$. All right and left scattering solutions defined by Eqs. 4.27 to 4.30 are respectively 2×1 and 1×2 spinors. We note the corresponding spin components $R^{\sigma,s}_{L'L}(r,\varepsilon)$, $\bar{R}^{s,\sigma}_{LL'}(r,\varepsilon)$, $S^{\sigma,s}_{L'L}(r,\varepsilon)$ and $\bar{S}^{s,\sigma}_{LL'}(r,\varepsilon)$.

Atomic t-matrix

The atomic t-matrix will be an essential element in the subsequent section on multiple scattering theory. We give its definition already here to conclude our study of scattering

properties of single atomic potentials:

$$t^{ss'}_{LL'}(\varepsilon) = \sum_{\sigma,\sigma'} \int_0^R dr\ J_L(r,\varepsilon)\delta_{s\sigma} \sum_{L''} V^{\sigma\sigma'}_{L,L''}(r) R^{\sigma's'}_{L''L'}(r,\varepsilon). \tag{4.31}$$

The atomic t-matrix is an essential property of a scattering potential because it gives the behaviour of the regular scattering solutions outside the scattering region:

$$R^{\sigma s}_{L'L}(r,\varepsilon) = \delta_{L',L}\delta_{s\sigma} J_L(r,\varepsilon) + \kappa\ t^{\sigma s}_{L'L}(\varepsilon) H_{L'}(r,\varepsilon), \qquad r \geq R. \tag{4.32}$$

4.2.3. Multiple scattering theory

In this section we show how the scattering properties of single atomic potentials obtained previously can be used to obtain the Green function of the whole crystal. For this we separate the Green function into local parts defined within each atomic cell and a non-local part that couples different cells with each other.

Expansion of the Green function of free space

The expansion of the potential-free Green function in real spherical harmonics was already given by Eq. 4.14. We use here a somewhat more concise formulation

$$g(\boldsymbol{x}, \boldsymbol{x'}, \varepsilon) = \kappa \sum_L j_L(\boldsymbol{x}_<, \varepsilon) h_L(\boldsymbol{x}_>, \varepsilon) \tag{4.33}$$

where $\boldsymbol{x}_< = \min(x, x')$ and $\boldsymbol{x}_> = \max(x, x')$. We also introduced the notation $j_L(\boldsymbol{x}, \varepsilon) = j_l(\kappa x, \varepsilon) Y_L(\hat{\boldsymbol{x}})$ and $h_L(\boldsymbol{x}, \varepsilon) = h_l(\kappa x, \varepsilon) Y_L(\hat{\boldsymbol{x}})$.

We rewrite Eq. 4.33 explicitly in terms of the vectors $\boldsymbol{R}_n$ and $\boldsymbol{r}$ to obtain a form that is suitable for multiple scattering theory. This can be done using a formula to expand Hankel functions centered around $\boldsymbol{R}_n$ into Bessel functions centered around $\boldsymbol{R}_{n'}$:

$$h_L(\boldsymbol{r'} + \boldsymbol{R}_{n'} - \boldsymbol{R}_n, \varepsilon) = \frac{1}{\kappa} \sum_{L'} g^{nn'}_{LL'}(\varepsilon) j_{L'}(\boldsymbol{r'}, \varepsilon). \tag{4.34}$$

The coefficients $g^{nn'}_{LL'}(\varepsilon)$ are called *structure constants* and are given by

$$g^{nn'}_{LL'}(\varepsilon) = 4\pi(1 - \delta_{n,n'})\, \kappa \sum_{L''} i^{l-l'+l''} C_{LL'L''} h_{L''}(\boldsymbol{R}_n - \boldsymbol{R}_{n'}, \varepsilon), \tag{4.35}$$

where $C_{LL'L''} = \int d\Omega\ Y_L(\hat{\boldsymbol{r}}) Y_{L'}(\hat{\boldsymbol{r}}) Y_{L''}(\hat{\boldsymbol{r}})$ are the Gaunt coefficients. Inserting Eq. 4.34 into Eq. 4.33 yields the expansion of the potential-free Green function in terms of the variables $\boldsymbol{R}_n$ and $\boldsymbol{r}$:

$$g(\boldsymbol{r} + \boldsymbol{R}_n, \boldsymbol{r'} + \boldsymbol{R}_{n'}, \varepsilon) = \delta_{nn'}\kappa \sum_L j_L(\boldsymbol{r}_<, \varepsilon) h_L(\boldsymbol{r}_>, \varepsilon) + \sum_{LL'} j_L(\boldsymbol{r}, \varepsilon) g^{nn'}_{LL'}(\varepsilon) j_{L'}(\boldsymbol{r'}, \varepsilon) \tag{4.36}$$

Expansion of the Green function for a periodic potential

An equation similar to Eq. 4.36 can be found for the Green function of the periodic potential [60]:

$$G(\boldsymbol{r}+\boldsymbol{R}_n,\boldsymbol{r'}+\boldsymbol{R}_{n'},\varepsilon)=\delta_{nn'}G_s(\boldsymbol{r},\boldsymbol{r'},\varepsilon)+\sum_{\Lambda\Lambda'}R_\Lambda(\boldsymbol{r},\varepsilon)G^{nn'}_{\Lambda\Lambda'}(\varepsilon)\bar{R}_{\Lambda'}(\boldsymbol{r'},\varepsilon), \tag{4.37}$$

where $G_s(\boldsymbol{r},\boldsymbol{r'},\varepsilon)$ is the single site Green function defined by Eq. 4.19 and $\Lambda=(L,s)$. The second term in Eq. 4.37 is given by the matrix elements of the *structural Green function* $G^{nn'}_{\Lambda\Lambda'}$, which can be computed from the structure constants (see Eq. 4.35) by the following Dyson equation:

$$G^{nn'}_{\Lambda\Lambda'}(\varepsilon)=g^{nn'}_{\Lambda\Lambda'}(\varepsilon)+\sum_{n''\Lambda''\Lambda'''}g^{nn''}_{\Lambda\Lambda''}(\varepsilon)\,t^{n''}_{\Lambda''\Lambda'''}(\varepsilon)\,G^{n''n'}_{\Lambda'''\Lambda'}(\varepsilon). \tag{4.38}$$

It is interesting to note that while the structure constants vanish for $n=n'$ in Eq. 4.35, the structural Green function does not, i.e., the multiple scattering term of Eq. 4.37 gives a contribution to the total Green function for $n=n'$. Therefore, the modification of charge density at site n due to the presence of the surrounding atoms is interpreted in the KKR formalism as electrons that leave the site n and then come back after a series of scattering events on the other atoms of the crystal. Clearly, no back scattering can happen in the case of free space, which explains the factor $(1-\delta_{n,n'})$ in Eq. 4.35.

In a periodic crystal the structural Green function clearly depends only on the relative position of the sites $\boldsymbol{R}_n-\boldsymbol{R}_{n'}$. We define the Fourrier transform of the structural Green function

$$G_{\Lambda\Lambda'}(\boldsymbol{k},\varepsilon)=\sum_{nn'}G^{nn'}_{\Lambda\Lambda'}(\varepsilon)\,e^{i\boldsymbol{k}\cdot(\boldsymbol{R}_n-\boldsymbol{R}_{n'})}, \tag{4.39}$$

which can also be computed using a Dyson equation

$$G_{\Lambda\Lambda'}(\boldsymbol{k},\varepsilon)=g_{\Lambda\Lambda'}(\boldsymbol{k},\varepsilon)+\sum_{\Lambda''\Lambda'''}g_{\Lambda\Lambda''}(\boldsymbol{k},\varepsilon)\,t_{\Lambda''\Lambda'''}(\varepsilon)\,G_{\Lambda'''\Lambda'}(\boldsymbol{k},\varepsilon). \tag{4.40}$$

The Fourier transform of the Green function of the reference system (e.g. free space)

$$g_{\Lambda\Lambda'}(\boldsymbol{k},\varepsilon)=\sum_{nn'}g^{nn'}_{\Lambda\Lambda'}(\varepsilon)\,e^{i\boldsymbol{k}\cdot(\boldsymbol{R}_n-\boldsymbol{R}_{n'})} \tag{4.41}$$

has to be computed first. The sum over n and n' can be restricted to a finite number of sites for a numerical estimate of $g_{\Lambda\Lambda'}(\boldsymbol{k},\varepsilon)$[3].

[3] In the Jülich KKR code we employ the so-called tight-binding or screened KKR formalism, where we use instead of free space a lattice of repulsive potentials as reference system. This drastically accelerates the decay of the Green function elements $g^{nn'}_{\Lambda\Lambda'}(\varepsilon)$ as a function of $\boldsymbol{R}_n-\boldsymbol{R}_{n'}$, which strongly reduces the computational cost for computing the Fourier transform of the Green function of the reference system $g_{\Lambda\Lambda'}(\boldsymbol{k},\varepsilon)$.

KKR secular equation

In this section we aim at finding the stationary solutions of the Schrödinger equation and the corresponding eigen energies for electrons in a periodic crystal by enforcing the incident wave at each site to be equal to the sum of the outgoing waves from all other sites. For this let us consider the wavefunction $\psi_{\boldsymbol{k}}$ as the sum of an incoming wave and a scattered wave at site n:

$$\psi_{\boldsymbol{k}}(\boldsymbol{r}+\boldsymbol{R}_n) = \psi_{\boldsymbol{k}}^{\mathrm{in},n}(\boldsymbol{r}+\boldsymbol{R}_n) + \psi_{\boldsymbol{k}}^{\mathrm{sc},n}(\boldsymbol{r}+\boldsymbol{R}_n) \tag{4.42}$$

where $\psi_{\boldsymbol{k}}^{\mathrm{in},n}(\boldsymbol{r}+\boldsymbol{R}_n)$ and $\psi_{\boldsymbol{k}}^{\mathrm{sc},n}(\boldsymbol{r}+\boldsymbol{R}_n)$ can be expanded respectively into Bessel and Hankel functions:

$$\psi_{\boldsymbol{k}}^{\mathrm{in},n}(\boldsymbol{r}+\boldsymbol{R}_n) = \sum_L c_{\boldsymbol{k}L}^{\mathrm{in},n} j_L(\boldsymbol{r},\varepsilon) \tag{4.43}$$

$$\psi_{\boldsymbol{k}}^{\mathrm{sc},n}(\boldsymbol{r}+\boldsymbol{R}_n) = \sum_{L'} c_{\boldsymbol{k}L'}^{\mathrm{sc},n} h_{L'}(\boldsymbol{r},\varepsilon) \tag{4.44}$$

The incoming wave can be regarded as the sum of the scattered waves from all other sites $n' \neq n$, i.e.,

$$\begin{aligned}\psi_{\boldsymbol{k}}^{\mathrm{in},n}(\boldsymbol{r}+\boldsymbol{R}_n) &= \sum_{n'\neq n} \psi_{\boldsymbol{k}}^{\mathrm{sc},n'}(\boldsymbol{r}+\boldsymbol{R}_n) \\ &= \sum_{n'\neq n}\sum_{L'} c_{\boldsymbol{k}L'}^{\mathrm{sc},n'} h_{L'}(\boldsymbol{r}+\boldsymbol{R}_n-\boldsymbol{R}_{n'},\varepsilon) \\ &= \frac{1}{\kappa}\sum_{n'\neq n}\sum_{LL'} c_{\boldsymbol{k}L'}^{\mathrm{sc},n'} g_{L'L}^{n'n}(\varepsilon) j_L(\boldsymbol{r},\varepsilon),\end{aligned} \tag{4.45}$$

where we used for the last line the transformation formula for Hankel functions (Eq. 4.34). Comparing Eqs. 4.43 and 4.45 yields by identification

$$c_{\boldsymbol{k}L}^{\mathrm{in},n} = \frac{1}{\kappa}\sum_{n'\neq n}\sum_{L'} c_{\boldsymbol{k}L'}^{\mathrm{sc},n'} g_{L'L}^{n'n}(\varepsilon). \tag{4.46}$$

For the wavefunction to be a stationary solution it has to fulfil the Bloch theorem, which implies that

$$c_{\boldsymbol{k}L'}^{\mathrm{sc},n'} = c_{\boldsymbol{k}L'}^{\mathrm{sc},n}\, e^{i\boldsymbol{k}\cdot(\boldsymbol{R}_{n'}-\boldsymbol{R}_n)}. \tag{4.47}$$

Inserting Eq. 4.47 into Eq. 4.46 yields a relation between the coefficients of the incoming and scattered wavefunctions at the same site n:

$$c_{\boldsymbol{k}L}^{\mathrm{in},n} = \frac{1}{\kappa}\sum_{L'} c_{\boldsymbol{k}L'}^{\mathrm{sc},n}\sum_{n'\neq n} g_{L'L}^{n'n}(\varepsilon) e^{i\boldsymbol{k}\cdot(\boldsymbol{R}_{n'}-\boldsymbol{R}_n)}. \tag{4.48}$$

We define the Fourier transform of the structure constant

$$g_{L'L}(\boldsymbol{k},\varepsilon) = \sum_{n'\neq n} g_{L'L}^{n'n}(\varepsilon) e^{i\boldsymbol{k}\cdot(\boldsymbol{R}_{n'}-\boldsymbol{R}_n)}. \tag{4.49}$$

to obtain the relation between incoming and scattered wavefunctions as a simple matrix multiplication:

$$c^{\mathrm{in},n}_{\boldsymbol{k}L} = \frac{1}{\kappa}\sum_{L'} c^{\mathrm{sc},n}_{\boldsymbol{k}L'} g_{L'L}(\boldsymbol{k},\varepsilon), \tag{4.50}$$

The relation between incoming and scattered waves given by Eq. 4.50 relies solely on the geometry of the system. On the other hand, the scattered wave is also related to the incoming wave by a Lippmann-Schwinger equation. This yields a second relation between wavefunction coefficients that is given by the t-matrix:

$$c^{\mathrm{sc},n}_{\boldsymbol{k}L} = \kappa \sum_{L'} t_{LL'}(\varepsilon) c^{\mathrm{in},n}_{\boldsymbol{k}L'}, \tag{4.51}$$

Combining Eqs. 4.50 and 4.51 leads to the KKR secular equation

$$\sum_{\Lambda'} \Big[\, \delta_{\Lambda\Lambda'} - \sum_{\Lambda''} g_{\Lambda\Lambda''}(\boldsymbol{k},\varepsilon) t_{\Lambda''\Lambda'}(\varepsilon) \Big] c^{\mathrm{in}}_{\boldsymbol{k}\Lambda'} = 0, \tag{4.52}$$

where we have dropped the arbitrary index n. This equation has solutions only for certain pairs of $\boldsymbol{k}$ and ε, corresponding to the energy of the bands. This implies to scan all energies for a given k-point when performing a band structure calculation. This is in contrast to the FLAPW method (see Section 3), where a single eigen value problem is solved at each k-point to obtain the band energies.

We aim now at finding the eigen states $\psi_{\boldsymbol{k}}$ in terms of the regular scattering solutions $R^{\mu}_{\Lambda}(\boldsymbol{r},\varepsilon)$ (Eq. 4.18). We make the ansatz

$$\psi_{\boldsymbol{k}}(\boldsymbol{r}+\boldsymbol{R}_n) = \sum_{\Lambda} c^{n}_{\boldsymbol{k}\Lambda} R_{\Lambda}(\boldsymbol{r},\varepsilon), \qquad \boldsymbol{r}+\boldsymbol{R}_n \in \text{cell } n \tag{4.53}$$

and we explain in the following how to find the expansion coefficients $c^{n}_{\boldsymbol{k}\Lambda}$. Starting again from Eq. 4.42, we expand explicitly the eigen state into Bessel and Hankel functions:

$$\psi_{\boldsymbol{k}}(\boldsymbol{r}+\boldsymbol{R}_n) = \sum_{\Lambda} c^{\mathrm{in},n}_{\boldsymbol{k}\Lambda} j_{\Lambda}(\boldsymbol{r},\varepsilon) + \sum_{\Lambda'} c^{\mathrm{sc},n}_{\boldsymbol{k}\Lambda'} h_{\Lambda'}(\boldsymbol{r},\varepsilon). \tag{4.54}$$

Using Eq. 4.51 again yields:

$$\psi_{\boldsymbol{k}}(\boldsymbol{r}+\boldsymbol{R}) = \sum_{\Lambda} \Big\{ \sum_{\Lambda'} j_{\Lambda}(\boldsymbol{r},\varepsilon)\ \delta_{\Lambda\Lambda'} + \kappa\ h_{\Lambda'}(\boldsymbol{r},\varepsilon)\ t_{LL'} \Big\} c^{\mathrm{in},n}_{\boldsymbol{k}\Lambda} \tag{4.55}$$

The term appearing in the bracket in Eq. 4.55 can be identified to be the regular scattering solution $R_{\Lambda}(\boldsymbol{r},\varepsilon)$ outside the scattering region, see Eq. 4.32. Because the wavefunction and the regular scattering solutions must be continuous at the cell boundary, the expansion coefficients $c^{n}_{\boldsymbol{k}\Lambda}$ in Eq. 4.53 have to be equal to $c^{\mathrm{in},n}_{\boldsymbol{k}\Lambda}$.

4.2.4. Generalization to multiple atoms in the unit cell

This thesis is dedicated to the calculation of spin-orbit torques in ferromagnetic bilayers. This class of systems obviously exhibit more than a single atom per unit cell, which requires a generalization of the expressions used in the previous section. We give here the general expressions for the most important quantities that will be used in the subsequent chapters.

The decomposition of the real space vector $\boldsymbol{x}$ defined by Eq. 4.5 requires to use an additional index μ to label the atom type within a unit cell. This decomposition in the case of multiple atoms in the unit cell reads

$$\boldsymbol{x} = \boldsymbol{R}_n + \boldsymbol{R}_\mu + \boldsymbol{r}, \tag{4.56}$$

where n is the index for the unit cell and μ the index for the atom type within the unit cell.

The potential of the crystal (Eq. 4.57) is now divided into cell- and atom-dependent potentials according to

$$V(\boldsymbol{x}) = \sum_{n\mu} V^{n\mu}(\boldsymbol{x} - \boldsymbol{R}_n - \boldsymbol{R}_\mu), \tag{4.57}$$

$$V^{n\mu}(\boldsymbol{r}) = \begin{cases} V(\boldsymbol{R}_n + \boldsymbol{R}_\mu + \boldsymbol{r}) & \text{if } \boldsymbol{r} \in \text{cell } \{n, \mu\} \\ 0 & \text{otherwise.} \end{cases} \tag{4.58}$$

The corresponding scattering solutions $R_L^{s,\mu}(\boldsymbol{r}, \varepsilon)$ and $S_L^{s,\mu}(\boldsymbol{r}, \varepsilon)$ are obtained from Eqs. 4.18 and 4.20 by replacing the potential by $V^{n\mu}(\boldsymbol{r})$.

This yields for the t-matrix (Eq 4.31) and the structure constants (Eq 4.35) the expressions

$$t_{LL'}^{ss',\mu}(\varepsilon) = \sum_{\sigma,\sigma'} \int_0^R dr\ J_L(r, \varepsilon)\delta_{s\sigma} \sum_{L''} V_{L,L''}^{\sigma\sigma',\mu}(r) R_{L''L'}^{\sigma's',\mu}(r, \varepsilon) \tag{4.59}$$

and

$$g_{LL'}^{nn',\mu\mu'}(\varepsilon) = 4\pi(1 - \delta_{n,n'}\delta_{\mu,\mu'}) \sum_{L''} i^{l-l'+l''} C_{LL'L''} h_{L''}(\boldsymbol{R}_n + \boldsymbol{R}_\mu - \boldsymbol{R}_{n'} - \boldsymbol{R}_{\mu'}, \varepsilon). \tag{4.60}$$

The secular equation (Eq. 4.52) in the case of multiple atoms in the unit cell takes the form

$$\sum_{\Lambda'\mu'} \Big[\delta_{\Lambda\Lambda'}\delta_{\mu\mu'} - \sum_{\Lambda''} g_{\Lambda\Lambda''}^{\mu\mu'}(\boldsymbol{k}, \varepsilon) t_{\Lambda''\Lambda'}^{\mu'}(\varepsilon) \Big] c_{\boldsymbol{k}\Lambda'}^{\mu'} = 0, \tag{4.61}$$

and the expansion of the wavefunction (Eq. 4.53) is given by

$$\psi_{\boldsymbol{k}}(\boldsymbol{r} + \boldsymbol{R}_\mu + \boldsymbol{R}_n) = \sum_{\Lambda} c_{\boldsymbol{k}\Lambda}^{\mu} R_\Lambda^\mu(\boldsymbol{r}, \varepsilon), \qquad \boldsymbol{r} + \boldsymbol{R}_\mu + \boldsymbol{R}_n \in \text{cell } \{n, \mu\}. \tag{4.62}$$

This expansion of the wavefunction will be used in Sections 4.2.5 and 4.3.

4.2.5. Scattering off impurities

When the periodicity of the crystal is broken by the presence of an impurity, the eigen states can not be found from Eq. 4.52. Instead, the calculation of the eigen states of an impurity embedded in a periodic host has to be considered as a scattering problem. It is conceptually similar to the determination of the scattering solutions of individual atomic potentials from Eqs. 4.18 and 4.20, but differs by the boundary conditions. While the use of products of spherical harmonics with Bessel and Hankel functions in Eqs. 4.18 and 4.20 was motivated by the use of free space as reference system, it is now natural to use the Bloch states of the periodic host as incoming boundary conditions.

We define the scattering solutions of the impurity potential by

$$\psi_{\boldsymbol{k}}^{\mathrm{imp}}(\boldsymbol{x}) = \psi_{\boldsymbol{k}}(\boldsymbol{x}) + \int d\boldsymbol{r'} G(\boldsymbol{x}, \boldsymbol{x'}) \Delta V(\boldsymbol{x'}) \psi_{\boldsymbol{k}}^{\mathrm{imp}}(\boldsymbol{x'}), \tag{4.63}$$

where $\psi_{\boldsymbol{k}}(\boldsymbol{x})$ are the host eigen states (Eq. 4.53), $G(\boldsymbol{x}, \boldsymbol{x'})$ is the host Green function (Eq. 4.37) and $\Delta V(\boldsymbol{x'})$ is the difference between host and impurity potentials. The index $\boldsymbol{k}$ used for the impurity scattering solution $\psi_{\boldsymbol{k}}^{\mathrm{imp}}(\boldsymbol{x})$ is to be understood as a label inherited from the host wavefunction. It is not a good quantum number for the impurity scattering solutions since they do not fulfil the Bloch theorem.

In practice we use a slightly different form of the Lippmann-Schwinger equation:

$$\psi_{\boldsymbol{k}}^{\mathrm{imp}}(\boldsymbol{x}) = \psi_{\boldsymbol{k}}(\boldsymbol{x}) + \int d\boldsymbol{r'} G^{\mathrm{imp}}(\boldsymbol{x}, \boldsymbol{x'}) \Delta V(\boldsymbol{x'}) \psi_{\boldsymbol{k}}(\boldsymbol{x'}), \tag{4.64}$$

where $G^{\mathrm{imp}}(\boldsymbol{x}, \boldsymbol{x'})$ is the impurity Green function, which is connected to the host Green function by a Dyson equation.

It is fruitful to introduce the scattering amplitudes (T-matrix) for the Bloch states:

$$T_{\boldsymbol{k'k}} = \int d^3\boldsymbol{x}\ \psi_{\boldsymbol{k'}}^{\dagger}(\boldsymbol{x}) \Delta V(\boldsymbol{x}) \psi_{\boldsymbol{k}}^{\mathrm{imp}}(\boldsymbol{x}). \tag{4.65}$$

Beside the insight it gives on the scattering properties of impurities, the T-matrix yields simple expressions for the transition rates of wave packets in a solid in the presence of a finite concentration of impurities. The expression is valid in the dilute limit and reads [45]

$$P_{\boldsymbol{kk'}} = \frac{2\pi}{\hbar} N \delta(\varepsilon(\boldsymbol{k}) - \varepsilon(\boldsymbol{k'})) c |T_{\boldsymbol{kk'}}|^2, \tag{4.66}$$

where N is the number of atoms in the crystal and c is the concentration of impurities. The corresponding relaxation times are given by

$$\tau_{\boldsymbol{k}}^{-1} = \sum_{\boldsymbol{k'}} P_{\boldsymbol{k'k}}. \tag{4.67}$$

These expressions for the transition rates and the relaxation times will be used in Section 4.4 within the Boltzmann formalism to investigate the impurity-driven spin-orbit torques in disordered bilayers.

It is straightforward to generalize Eq. 4.68 to the case of different types of impurities by

$$P_{\boldsymbol{k}\boldsymbol{k'}} = \frac{2\pi}{\hbar} N \delta(\varepsilon(\boldsymbol{k}) - \varepsilon(\boldsymbol{k'})) \sum_m c_m |T^m_{\boldsymbol{k}\boldsymbol{k'}}|^2, \tag{4.68}$$

where c_m and $T^m_{\boldsymbol{k}\boldsymbol{k'}}$ are the concentration and the scattering amplitudes for impurity type m. A similar expression has been used successfully in the past for the study of the spin Hall and spin Nernst effects in ternary alloys [61].

We now discuss the implementation of Eqs. 4.64 and 4.65 in the KKR formalism. A difficulty for solving Eq. 4.64 is that the Bloch states $\psi_{\boldsymbol{k}}$ are expanded into the regular scattering solutions of the host $R^{\mu}_{\Lambda}(\boldsymbol{r}, \varepsilon)$ (Eq. 4.53), while the impurity scattering solutions $\psi^{\text{imp}}_{\boldsymbol{k}}$ are expanded into the regular scattering solutions of the perturbed atomic potentials $R^{\text{imp},\mu}_{\Lambda}(\boldsymbol{r}, \varepsilon)$ [4], defined by

$$R^{\text{imp},i}_{\Lambda}(\boldsymbol{r}, \varepsilon) = j_l(\kappa r) Y_L(\hat{\boldsymbol{r}}) \chi^s + \int d\boldsymbol{r'}\ g(\boldsymbol{r}, \boldsymbol{r'}, \varepsilon_k) V^{\text{imp}}(\boldsymbol{r'}) R^{\text{imp},i}_{\Lambda}(\boldsymbol{r'}, \varepsilon). \tag{4.69}$$

The corresponding expansion for the impurity scattering solutions $\psi^{\text{imp}}_{\boldsymbol{k}}$ reads

$$\psi^{\text{imp}}(\boldsymbol{r} + \boldsymbol{R_\mu}) = \sum_{\Lambda} c^{\text{imp},i}_{\Lambda} R^{\text{imp},i}_{\Lambda}(\boldsymbol{r}, \varepsilon), \qquad \boldsymbol{r} \in V_i \tag{4.70}$$

where the index i is used to label the atoms in the impurity region.

Most convenient is to obtain the coefficients $c^{\text{imp},i}_{\Lambda}$ in terms of the coefficients c^{μ}_{Λ} of the expansion of the Bloch states (Eq.4.53). The following expression was derived by [62]:

$$c^{\text{imp},i}_{\Lambda} = \sum_{\Lambda',i'} \left\{ \delta_{\Lambda\Lambda'} \delta_{ii'} + \sum_{\Lambda''} G^{\text{imp},ii'}_{\Lambda\Lambda''} \Delta t^{\text{imp},i'}_{\Lambda''\Lambda'} \right\} c^{\mu'}_{\Lambda'} e^{i\boldsymbol{k}\cdot\boldsymbol{R}_{n'}} \tag{4.71}$$

where the equality $c^{i'}_{\Lambda'} = c^{\mu'}_{\Lambda'} e^{i\boldsymbol{k}\cdot\boldsymbol{R}_{n'}}$ was used. The t-matrix elements $\Delta t^{\text{imp},i'}_{\Lambda''\Lambda'}$ are defined by

$$\Delta t^{\text{imp},i}_{\Lambda,\Lambda'} = \sum_{\Lambda''\Lambda'''} \int dr\ \bar{R}^{i}_{\Lambda\Lambda''}(r) \Delta V^{i}_{\Lambda''\Lambda'''}(\boldsymbol{r}) R^{\text{imp},i}_{\Lambda'''\Lambda'}(r) \tag{4.72}$$

[4] An expansion of the impurity scattering solutions $\psi^{\text{imp}}_{\boldsymbol{k}}$ into the regular scattering solutions of the host $R^{\mu}_{\Lambda}(\boldsymbol{r}, \varepsilon)$ would in principle be possible, but the number of regular scattering solutions needed would be higher for the same accuracy.

and $G^{\mathrm{imp},ii'}_{\Lambda\Lambda'}$ are the matrix elements of the structural impurity Green function[5].

The structural host Green function $G^{ii'}_{\Lambda\Lambda'}$ and impurity Green function $G^{\mathrm{imp},ii'}_{\Lambda\Lambda'}$ are related by a Dyson equation

$$G^{\mathrm{imp},ii'}_{\Lambda\Lambda'} = G^{ii'}_{\Lambda\Lambda'} + \sum_{\Lambda''\Lambda'''} \sum_{i''} G^{ii''}_{\Lambda\Lambda''} \Delta t^{i''}_{\Lambda''\Lambda'''} G^{\mathrm{imp},i''i'}_{\Lambda'''\Lambda'}, \tag{4.73}$$

where $\Delta t^{i''}_{\Lambda''\Lambda'''} = t^{\mathrm{imp},i''}_{\Lambda''\Lambda'''} - t^{\mathrm{host},i''}_{\Lambda''\Lambda'''}$ with both t-matrices computed according to Eq. 4.31.

Now that we know how to compute the expansion coefficients of the impurity scattering solutions $c^{\mathrm{imp},i}_{\Lambda}$, it is straightforward to obtain the scattering amplitudes

$$T_{\boldsymbol{k'k}} = \sum_{\Lambda\Lambda'} \sum_{i} [c^{i}_{\boldsymbol{k'},\Lambda}]^* \Delta^{i}_{\Lambda\Lambda'} c^{\mathrm{imp},i}_{\boldsymbol{k},\Lambda'}, \tag{4.74}$$

where we have defined the Δ-matrix

$$\Delta^{i}_{\Lambda,\Lambda'} = \sum_{\Lambda''\Lambda'''} \int dr\ [R^{i}_{\Lambda\Lambda''}(r)]^* \Delta V^{i}_{\Lambda''\Lambda'''}(\boldsymbol{r}) R^{\mathrm{imp},i}_{\Lambda'''\Lambda'}(r). \tag{4.75}$$

Combining Eqs. 4.71 and 4.74 yields a very elegant expression for the scattering amplitudes where only the expansion coefficients of the Bloch states enter:

$$T_{\boldsymbol{k'k}} = \sum_{\Lambda\Lambda'} \sum_{i,i'} [c^{i}_{\boldsymbol{k'},\Lambda}]^* T^{i,i'}_{\Lambda\Lambda'} c^{i'}_{\boldsymbol{k},\Lambda'}. \tag{4.76}$$

We have used in the previous equation the $\{\Lambda, i\}$-representation of the T-matrix

$$T^{i,i'}_{\Lambda\Lambda'} = \sum_{\Lambda''} \Delta^{i}_{\Lambda,\Lambda''} \Big(\delta_{ii'} \delta\Lambda''\Lambda' + \sum_{\Lambda'''} G^{\mathrm{imp},ii'}_{\Lambda''\Lambda'''} \Delta t^{\mathrm{imp},i'}_{\Lambda''',\Lambda'} \Big), \tag{4.77}$$

which is independent of $\boldsymbol{k}$ and therefore must be computed only once.

4.3. KKR representation of operators

We aim at computing the torque and the spin accumulation induced by an external electric field. This implies to be able to compute the torque and spin expectation values of individual electronic states. In this section we derive the expressions for the torque and spin operators in the KKR formalism. We then proceed with the spin flux operator, which is useful to determine how much of the torque arises from spin currents. Finally, we discuss how the velocity of the states can be obtained from the relativistic velocity operator (α-matrix).

[5] The full expression for the impurity Green function reads $G^{\mathrm{imp}}(\boldsymbol{r}+\boldsymbol{\tau}_i, \boldsymbol{r'}+\boldsymbol{\tau}_{i'}) = \delta_{ii'} G^{\mathrm{imp},i}_{s}(\boldsymbol{r}, \boldsymbol{r'}) + \sum_{\Lambda\Lambda'} R^{\mathrm{imp},i}_{\Lambda}(\boldsymbol{r})\, G^{\mathrm{imp},ii'}_{\Lambda\Lambda'}\, \bar{R}^{\mathrm{imp},i'}_{\Lambda'}(\boldsymbol{r'})$, but the single-site term is not needed to determine the scattering amplitudes $T_{\boldsymbol{kk'}}$. It is however used to compute the charge density when the impurity potential is determined self-consistently, see [59].

4.3.1. Spin operator

The contribution of a state to the i-th component of the spin at the atom μ is given by:

$$\langle \sigma_{i\mu} \rangle_{\boldsymbol{k}} = \langle \psi_{\boldsymbol{k}} | \sigma_{i\mu} | \psi_{\boldsymbol{k}} \rangle = \int_{V_\mu} d^3r \; [\psi_{\boldsymbol{k}}(\boldsymbol{r})]^\dagger \sigma_i \psi_{\boldsymbol{k}}(\boldsymbol{r}), \tag{4.78}$$

where the integration is performed over the volume of the atomic cell V_μ. In the KKR formalism the wavefunction $\psi_{\boldsymbol{k}}$ at site μ is expanded into the regular scattering solutions of the corresponding atomic potential (Eq. 4.53). The spin expectation value then reads

$$\langle \sigma_{i\mu} \rangle_{\boldsymbol{k}} = \sum_{Ls} \sum_{L's'} [c_L^{s,\mu}]^* c_{L'}^{s',\mu} \int_{V_\mu} d^3r \; \theta^\mu(\boldsymbol{r}) [R_L^{s,\mu}(\boldsymbol{r}, \varepsilon)]^\dagger \sigma_i R_{L'}^{s',\mu}(\boldsymbol{r}, \varepsilon), \tag{4.79}$$

where the integration could be extended to entire space by the introduction of the shape function $\theta^\mu(\boldsymbol{r})$ (Eq. 4.9) in the integral. The previous equation can be written in the form of a matrix multiplication:

$$\langle \sigma_{i\mu} \rangle_{\boldsymbol{k}} = \sum_{Ls} \sum_{L's'} [c_L^{s,\mu}]^* \, \Sigma_{LL',i}^{ss',\mu} \, c_{L'}^{s',\mu}, \tag{4.80}$$

by defining the matrix elements [62, 63]

$$\Sigma_{LL',i}^{ss',\mu} = \int_{V_\mu} d^3r \; \theta^\mu(\boldsymbol{r}) [R_L^{s,\mu}(\boldsymbol{r}, \varepsilon)]^\dagger \sigma_i R_{L'}^{s',\mu}(\boldsymbol{r}, \varepsilon). \tag{4.81}$$

Both the shape function and the regular scattering solutions are expanded into spherical harmonics according to Eqs. 4.10 and 4.25. The spin matrix elements in the KKR formalism finally read

$$\Sigma_{LL',i}^{ss',\mu} = \sum_{L_1 L_2 L_3} C_{L_1,L_2,L_3} \int dr \; \theta_{L_1}^\mu(r) [R_{L_2 L}^{s,\mu}(r)]^\dagger \sigma_i R_{L_3 L'}^{s',\mu}(r), \tag{4.82}$$

were C_{L_1,L_2,L_3} are the Gaunt coefficients (Eq. 4.12). Since the regular scattering solutions are always computed for the eigen energy of state $\psi_{\boldsymbol{k}}$, we have omitted the energy parameter ε in Eq. 4.82.

4.3.2. Torque operator

According to Eq. 2.12, the components of the torque operator are given by:

$$\mathcal{T}_i(\boldsymbol{r}) = -\mu_B \sum_{jk} \epsilon_{ijk} \sigma_j B_k(\boldsymbol{r}), \tag{4.83}$$

where ϵ_{ijk} is the Levi-Civita symbol and the indices i, j and k are x, y or z. The derivation of the torque matrix elements is somewhat more complicated than for the spin matrix elements, because the exchange field $\boldsymbol{B}(\boldsymbol{r})$ enters explicitly the definition

of the torque operator in Eq. 4.83. In the following we show in detail how to obtain the torque matrix elements in the KKR formalism.

The torque exerted on a state at the atom μ is given by:

$$\begin{aligned}\langle \mathcal{T}_{i\mu} \rangle_{\boldsymbol{k}} &= \langle \psi_{\boldsymbol{k}} | \mathcal{T}_{i\mu} | \psi_{\boldsymbol{k}} \rangle \\ &= -\mu_B \sum_{jk} \epsilon_{ijk} \int_{V_\mu} d^3r \; [\psi_{\boldsymbol{k}}(\boldsymbol{r})]^\dagger \sigma_j \psi_{\boldsymbol{k}}(\boldsymbol{r}) B_k(\boldsymbol{r}).\end{aligned} \tag{4.84}$$

Similarly to Eq. 4.80 this can be cast into the form

$$\langle \mathcal{T}_{i\mu} \rangle_{\boldsymbol{k}} = \sum_{Ls} \sum_{L's'} [c_L^{s,\mu}]^* \, \mathfrak{T}_{LL',i}^{ss',\mu} \, c_{L'}^{s',\mu}, \tag{4.85}$$

where the matrix elements $\mathfrak{T}_{LL',i}^{ss',\mu}$ are defined by

$$\mathfrak{T}_{LL',i}^{ss',\mu} = -\mu_B \sum_{jk} \epsilon_{ijk} \int_{V_\mu} d^3r \; [R_L^{s,\mu}(\boldsymbol{r})]^\dagger \sigma_j R_{L'}^{s',\mu}(\boldsymbol{r}) B_k^\mu(\boldsymbol{r}). \tag{4.86}$$

Using the shape functions $\theta^\mu(\boldsymbol{r})$ of the voronoi cells (Eq. 4.9), we can extend the space integration to the entire space. This yields the expression

$$\mathfrak{T}_{LL',i}^{ss',\mu} = -\mu_B \sum_{jk} \epsilon_{ijk} \int d^3r \; \theta^\mu(\boldsymbol{r}) [R_L^{s,\mu}(\boldsymbol{r})]^\dagger \sigma_j R_{L'}^{s',\mu}(\boldsymbol{r}) B_k^\mu(\boldsymbol{r}). \tag{4.87}$$

where we introduced the notation $B_k^\mu(\boldsymbol{r}) = B_k(\boldsymbol{r} + \boldsymbol{R}_\mu)$.

The scattering solutions $R_L^{s,\mu}(\boldsymbol{r})$, the shape functions $\theta^\mu(\boldsymbol{r})$ and the exchange field $B_k^\mu(\boldsymbol{r})$ are all expanded in real spherical harmonics as:

$$R_L^{s,\mu}(\boldsymbol{r}) = \sum_{L_2} \frac{1}{r} R_{L_2 L}^{s,\mu}(r) Y_{L_2}(\hat{\boldsymbol{r}}), \tag{4.88}$$

$$\theta^\mu(\boldsymbol{r}) = \sum_{L_1} \theta_{L_1}^\mu(r) Y_{L_1}(\hat{\boldsymbol{r}}), \tag{4.89}$$

$$B_k^\mu(\boldsymbol{r}) = \sum_{L_4} B_{L_4,k}^\mu(r) Y_{L_4}(\hat{\boldsymbol{r}}). \tag{4.90}$$

To avoid the integration of the product of four spherical harmonics, we first compute the convoluted exchange field $b_k^\mu(\boldsymbol{r}) = B_k^\mu(\boldsymbol{r}) \theta^\mu(\boldsymbol{r})$ and then replace the two spherical harmonics expansions of $B_k^\mu(\boldsymbol{r})$ and $\theta^\mu(\boldsymbol{r})$ by a single one for $b_k^\mu(\boldsymbol{r})$:

$$b_k^\mu(\boldsymbol{r}) = \sum_{L_5} b_{L_5,k}^\mu(r) Y_{L_5}(\hat{\boldsymbol{r}}). \tag{4.91}$$

Inserting Eqs. 4.88, 4.89 and 4.91 into Eq. 4.87 yields the torque matrix elements in the KKR formalism:

$$\mathfrak{T}_{LL',i}^{ss',\mu} = -\mu_B \sum_{jk} \epsilon_{ijk} \sum_{L_2 L_3 L_5} C_{L_2 L_3 L_5} \int dr \; [R_{L_2 L}^{s,\mu}(r)]^\dagger \sigma_j R_{L_3 L'}^{s',\mu}(r) b_{L_5,k}^\mu(r). \tag{4.92}$$

4.3.3. Spin flux operator

We derive in the following the expression for the spin flux operator, which is useful to determine how much of the torque arises from spin currents. The contribution of a state to the spin flux flowing into the atom μ is given by:

$$\langle \mathcal{Q}_{i\mu} \rangle_{\boldsymbol{k}} = -\frac{\mu_B \hbar}{2ie} \int_{S_\mu} d\boldsymbol{S} \cdot [\psi^\dagger_{\boldsymbol{k}}(\boldsymbol{r}) \sigma_i \boldsymbol{\nabla} \psi_{\boldsymbol{k}}(\boldsymbol{r}) - \boldsymbol{\nabla} \psi^\dagger_{\boldsymbol{k}}(\boldsymbol{r}) \sigma_i \psi_{\boldsymbol{k}}(\boldsymbol{r})], \tag{4.93}$$

where the surface S_μ corresponds to the muffin-tin (MT) sphere of the atom μ.

In the KKR representation the expectation values of the spin-flux operator can be cast into the form

$$\langle \mathcal{Q}_{i\mu} \rangle_{\boldsymbol{k}} = \sum_{Ls} \sum_{L's'} [c_L^{s,\mu}]^* \, q^{ss',\mu}_{LL',i} \, c_{L'}^{s',\mu}, \tag{4.94}$$

where the matrix elements $q^{ss',\mu}_{LL',i}$ are defined by

$$q^{ss',\mu}_{LL',i} = -\frac{\mu_B \hbar}{2ie} \int_{S_\mu} d\boldsymbol{S} \cdot \Big[[R_L^{s,\mu}(\boldsymbol{r})]^\dagger \sigma_i \boldsymbol{\nabla} R_{L'}^{s',\mu}(\boldsymbol{r}) - [\boldsymbol{\nabla} R_L^{s,\mu}(\boldsymbol{r})]^\dagger \sigma_i R_{L'}^{s',\mu}(\boldsymbol{r}) \Big]. \tag{4.95}$$

Because the integration is performed on the MT sphere, radial and angular variables can be separated. The infinitesimal surface elements in Eq. 4.95 take the form $d\boldsymbol{S} = r^2_{\mathrm{MT}} \boldsymbol{e}_\Omega d\Omega$, where $\boldsymbol{e}_\Omega$ is a unit vector pointing towards the center of the MT. The integration over the surface of the MT can be replaced by an integration over the solid angle Ω and the $\boldsymbol{\nabla}$ operator can be replaced by a simple derivative with respect to r (with a minus sign). Using the expansion of the scattering solutions in spherical harmonics the orthogonality of the spherical harmonics gives after a few lines of calculus the expression for the spin flux matrix elements

$$q^{ss',\mu}_{LL',i} = -\frac{\mu_B \hbar}{2ie} \sum_{L_1} \Big[[R^{s,\mu}_{L_1 L}(r)]^\dagger \sigma_i \frac{\partial}{\partial r} \Big(R^{s',\mu}_{L_1 L'}(r) \Big) - R^{s',\mu}_{L_1 L'}(r) \sigma_i \frac{\partial}{\partial r} \Big([R^{s,\mu}_{L_1 L}(r)]^\dagger \Big) \Big]_{r = r_{\mathrm{MT}}}. \tag{4.96}$$

4.3.4. Relativistic velocity operator (α-matrix)

The definition of an appropriate velocity operator is essential for the investigation of transport properties of solids. In relativistic quantum mechanics the information on the velocity of a state is encoded in the coupling between the four components of the wavefunction[6] $\psi_{\boldsymbol{k}}(\boldsymbol{r}) = (\psi^\downarrow_{\boldsymbol{k}L}(\boldsymbol{r}), \psi^\uparrow_{\boldsymbol{k}L}(\boldsymbol{r}), \psi^\downarrow_{\boldsymbol{k}S}(\boldsymbol{r}), \psi^\uparrow_{\boldsymbol{k}S}(\boldsymbol{r}))^T$. The exact velocity operator is given in units of the velocity of light by the α-matrix:

$$\alpha_i = \begin{pmatrix} 0 & \sigma_i \\ \sigma_i & 0 \end{pmatrix}. \tag{4.97}$$

[6] Although not specified in the previous sections, the scattering solutions defined by Eqs. 4.18, 4.20, 4.22 and 4.23 are four-component spinors computed in the scalar relativistic approximation, see Ref [59]. Because the small component is normally much smaller than the large component, it is not essential for the spin, torque and spin flux operators, but is crucial for the α-matrix, which couples both components.

The velocity for state $\psi_{\boldsymbol{k}}(\boldsymbol{r})$ is given by the expectation value

$$\langle\psi|v_i|\psi\rangle = \int_{u.c.} d^3r\ \psi^\dagger(\boldsymbol{r}) c\alpha_i \psi(\boldsymbol{r}) \tag{4.98}$$

where c is the velocity of light.

Using the element-wise notation for the α-matrix, one obtains

$$\langle\psi|v_i|\psi\rangle = \sum_{\sigma\beta}\sum_{\sigma'\beta'} c\alpha_i^{\sigma\beta,\sigma'\beta'} \int_{u.c.} d^3r\ [\psi_\beta^\sigma(\boldsymbol{r})]^* \psi_{\beta'}^{\sigma'}(\boldsymbol{r}) \tag{4.99}$$

where $\sigma = \{\downarrow,\uparrow\}$ is the spin index and $\beta = \{\text{large}, \text{small}\}$ is the index for large and small components.

Expanding the wavefunction in terms of the regular scattering solutions $R_{L'}^{s,\mu}(\boldsymbol{r},\varepsilon)$ (Eq. 4.18) and introducing the shape functions $\theta^\mu(\boldsymbol{r})$ (Eq. 4.9) in the integration yields

$$\langle\psi|v_i|\psi\rangle = \sum_\mu \sum_{Ls} \sum_{L's'} [c_L^{s,\mu}]^* c_{L'}^{s',\mu} \sum_{\sigma\beta}\sum_{\sigma'\beta'} c\alpha_i^{\sigma\beta,\sigma'\beta'} \int_{u.c.} d^3r\ \theta^\mu(\boldsymbol{r}) [R_L^{\sigma\beta s,\mu}(\boldsymbol{r})]^* R_{L'}^{\sigma'\beta' s',\mu}(\boldsymbol{r}) \tag{4.100}$$

Proceeding in a similar way as for the spin and torque operators, one finds the following expression for the KKR representation of the velocity operator in terms of the α-matrix :

$$\mathcal{V}_{LL',i}^{ss',\mu} = \sum_{\sigma\beta}\sum_{\sigma'\beta'} c\alpha_i^{\sigma\beta,\sigma'\beta'} \sum_{L_1L_2L_3} C_{L_1,L_2,L_3} \int dr\ \theta_{L_1}^\mu(r) [R_{L_2L}^{\sigma\beta s,\mu}(r)]^* R_{L_3L'}^{\sigma'\beta' s',\mu}(r). \tag{4.101}$$

The expectation values then read

$$\langle\psi|v_i|\psi\rangle = \sum_\mu \sum_{Ls} \sum_{L's'} \mathcal{V}_{LL',i}^{ss',\mu} [c_L^{s,\mu}]^* c_{L'}^{s',\mu}. \tag{4.102}$$

In the equation Eq. 4.100, it is important to note that $R_L^{s,\mu}(\boldsymbol{r})$ and $R_{L'}^{s',\mu}(\boldsymbol{r})$ must be approximated solutions of the Dirac equation for the single site problem (formulated in terms of a Lippmann-Schwinger equation). In the way the scalar relativistic approximation is implemented in the Jülich KKR code, the scattering solutions $R_L^{s,\mu}(\boldsymbol{r})$ need to be slightly modified in order to provide an approximate solution to the Dirac equation. We thus need a new set of scattering solutions

$$\widetilde{R}_L^{s,\mu}(\boldsymbol{r}) = \begin{pmatrix} \widetilde{R}_L^{s,\mu,\text{large}}(\boldsymbol{r}) \\ \widetilde{R}_L^{s,\mu,\text{small}}(\boldsymbol{r}) \end{pmatrix} = \begin{pmatrix} R_L^{s,\mu,\text{large}}(\boldsymbol{r}) \\ -i\frac{\boldsymbol{\sigma}\cdot\boldsymbol{r}}{r} R_L^{s,\mu,\text{small}}(\boldsymbol{r}) \end{pmatrix}, \tag{4.103}$$

which can be used to compute the matrix elements of the velocity operator from the α-matrix.

Using the expansion

$$\frac{\boldsymbol{\sigma}\cdot\boldsymbol{r}}{r} = \sqrt{\frac{4\pi}{3}}\Big(Y_{1,1}(\hat{r})\sigma_x + Y_{1,-1}(\hat{r})\sigma_y + Y_{1,0}(\hat{r})\sigma_z\Big) \tag{4.104}$$

yields the following expression for the small component of the new scattering solutions:

$$\begin{aligned}\widetilde{R}_L^{s,\mu,\text{small}}(\boldsymbol{r}) = \sum_{L''}\frac{1}{r}(-i)\sqrt{\frac{4\pi}{3}}\Big[\Big(&Y_{1,1}(\hat{r})Y_{L''}(\hat{r})\sigma_x + Y_{1,-1}(\hat{r})Y_{L''}(\hat{r})\sigma_y \\ &+ Y_{1,0}(\hat{r})Y_{L''}(\hat{r})\sigma_z\Big]R_{L''L}^{s,\mu,\text{small}}(r).\end{aligned} \tag{4.105}$$

The products of spherical harmonics can be themselves expanded in spherical harmonics using the Gaunt coefficients, which leads to the expression

$$\begin{aligned}\widetilde{R}_L^{s,\mu,\text{small}}(\boldsymbol{r}) = \sum_{L_1}\frac{1}{r}Y_{L_1}(\hat{r})\Big[-i\sqrt{\frac{4\pi}{3}}\sum_{L''}\Big(&G_{L_1L''(1,1)}\sigma_x + G_{L_1L''(1,-1)}\sigma_y \\ &+ G_{L_1L''(1,0)}\sigma_z\Big)R_{L''L}^{s,\mu,\text{small}}(r)\Big],\end{aligned} \tag{4.106}$$

where L_1 should run in principle from 1 to $(l_{max}+1)^2+4$ but can be restricted to $(l_{max}+1)^2$ for consistency with the rest of the code.

In the previous equation one can easily identify the radial parts of the scattering solutions

$$\widetilde{R}_{L_1L}^{s,\mu,\text{small}}(r) = -i\sqrt{\frac{4\pi}{3}}\sum_{L''}\Big(G_{L_1L''(1,1)}\sigma_x + G_{L_1L''(1,-1)}\sigma_y + G_{L_1L''(1,0)}\sigma_z\Big)R_{L''L}^{s,\mu,\text{small}}(r). \tag{4.107}$$

4.4. Boltzmann formalism for the torque

The Heisenberg uncertainty principle states that position and momentum of a particle cannot be known simultaneously. However, it is possible to build a wavepacket of Bloch states with a width Δk in reciprocal space, whose wavefunction spreads only over a distance $\Delta R \sim 1/\Delta k$ in real space. Such a wavepacket of Bloch states taken from band n obeys the following semiclassical equations of motion :

$$\dot{\boldsymbol{r}} = \boldsymbol{v}_n(\boldsymbol{k}) = \frac{1}{\hbar}\frac{\partial\varepsilon_n(\boldsymbol{k})}{\partial\boldsymbol{k}}, \tag{4.108}$$

$$\hbar\dot{\boldsymbol{k}} = -e\boldsymbol{E}(\boldsymbol{r},t) + \frac{e}{c}\boldsymbol{v}_n(\boldsymbol{k})\times\boldsymbol{H}(\boldsymbol{r},t). \tag{4.109}$$

We can define the distribution function $f_n(\boldsymbol{r},\boldsymbol{k},t)$ so that $f_n(\boldsymbol{r},\boldsymbol{k},t)d\boldsymbol{r}d\boldsymbol{k}/(2\pi)^3$ gives the number of electrons in band n in a volume $d\boldsymbol{r}d\boldsymbol{k}$ of the semiclassical phase space

at time t. In the absence of collisions, the motion of the electrons in phase space is fully defined by the equations Eqs. 4.108 and 4.109. The distribution function then obeys the relation

$$\frac{df_n}{dt} = \frac{\partial f_n}{\partial t} + \dot{\boldsymbol{r}}\ \nabla_{\boldsymbol{r}} f_n + \dot{\boldsymbol{k}}\ \nabla_{\boldsymbol{k}} f_n. \tag{4.110}$$

It is important to note at that point that the semiclassical equations of motions Eqs. 4.108 and 4.109 rely on the bandstructure $\varepsilon_n(\boldsymbol{k})$ of a periodic system and therefore can not account for scattering on defects. Nevertheless, it is crucial to incorporate the effect of scattering on the distribution function, since the absence of scattering would lead to unphysical results, such as infinite conductivity in metals. The Eq. 4.110 then becomes

$$\frac{\partial f_n}{\partial t} + \dot{\boldsymbol{r}}\ \nabla_{\boldsymbol{r}} f_n + \dot{\boldsymbol{k}}\ \nabla_{\boldsymbol{k}} f_n = \sum_{n'\boldsymbol{k'}} \Big(g_{n'}(\boldsymbol{k'}) P^{nn'}_{\boldsymbol{kk'}} - g_n(\boldsymbol{k}) P^{n'n}_{\boldsymbol{k'k}} \Big), \tag{4.111}$$

where $P^{nn'}_{\boldsymbol{kk'}}$ is the rate of the transition from the state $n'\boldsymbol{k'}$ into the state $n\boldsymbol{k}$ that is induced by the scattering off impurities. We have defined the deviation of the distribution function $g_n(\boldsymbol{k}) = f_n(\boldsymbol{k}) - f^0_n(\varepsilon(\boldsymbol{k}))$ as the difference between the non-equilibrium distribution function $f_n(\boldsymbol{k})$ and the equilibrium Fermi-Dirac distribution $f^0_n(\varepsilon(\boldsymbol{k}))$.

In the case of a time-independent homogeneous electric field, the Eq. 4.111 simplifies to

$$\dot{\boldsymbol{k}}\ \nabla_{\boldsymbol{k}} f_n = \sum_{n'\boldsymbol{k'}} \Big(g_{n'}(\boldsymbol{k'}) P^{nn'}_{\boldsymbol{kk'}} - g_n(\boldsymbol{k}) P^{n'n}_{\boldsymbol{k'k}} \Big). \tag{4.112}$$

For a weak electric field, the gradient of the distribution function $\nabla_{\boldsymbol{k}} f_n$ can be well approximated by $\frac{\partial f^0_n(\varepsilon(\boldsymbol{k}))}{\partial \varepsilon(\boldsymbol{k})} \boldsymbol{v}_n(\boldsymbol{k})$. This yields the relation

$$-e \frac{\partial f^0_n(\varepsilon(\boldsymbol{k}))}{\partial \varepsilon(\boldsymbol{k})} \boldsymbol{v}_n(\boldsymbol{k}) \cdot \boldsymbol{E} = \sum_{n'\boldsymbol{k'}} \Big(g_{n'}(\boldsymbol{k'}) P^{nn'}_{\boldsymbol{kk'}} - g_n(\boldsymbol{k}) P^{n'n}_{\boldsymbol{k'k}} \Big), \tag{4.113}$$

where $\boldsymbol{v}_n(\boldsymbol{k}) = \nabla_{\boldsymbol{k}} \varepsilon_n(\boldsymbol{k})$ is the group velocity.

For a weak electric field, the variation of the distribution function $g_n(\boldsymbol{k})$ is expected to be linear in $\boldsymbol{E}$ and sizeable only close to the Fermi energy, which suggests the following Ansatz:

$$g_n(\boldsymbol{k}) = e \frac{\partial f^0(\varepsilon_n(\boldsymbol{k}))}{\partial \varepsilon_n(\boldsymbol{k})} \boldsymbol{\lambda}_n(\boldsymbol{k}) \cdot \boldsymbol{E}. \tag{4.114}$$

Inserting Eq. 4.114 into Eq. 4.113 yields a self-consistent equation for the vector mean free path $\boldsymbol{\lambda}$:

$$\boldsymbol{\lambda}(\boldsymbol{k}) = \tau_{\boldsymbol{k}} \Big(\boldsymbol{v}(\boldsymbol{k}) + \sum_{\boldsymbol{k'}} P_{\boldsymbol{kk'}} \boldsymbol{\lambda}(\boldsymbol{k'}) \Big), \tag{4.115}$$

where $\tau_{\boldsymbol{k}}$ is the relaxation time for state $\boldsymbol{k}$ as defined by Eq. 4.67. We drop the band indices because the transition rates $P_{\boldsymbol{kk'}}$ are energy-conserving. The equation

for the mean free path can be solved numerically on the Fermi surface. It is then straightforward to find the variation of the distribution function $g(\boldsymbol{k})$ according to Eq. 4.114.

The torque induced by the electric field on atom μ is given by

$$\begin{aligned}\boldsymbol{T}_\mu &= -\frac{1}{\mathcal{S}_{\mathcal{BZ}}}\sum_n \int d^2\boldsymbol{k}\; g_n(\boldsymbol{k})\langle \boldsymbol{\mathcal{T}}_\mu\rangle_{n\boldsymbol{k}} \\ &= -\frac{1}{\mathcal{S}_{\mathcal{BZ}}}\sum_n \int d^2\boldsymbol{k}\; e\frac{\partial f^0(\varepsilon_n(\boldsymbol{k}))}{\partial \varepsilon_n(\boldsymbol{k})}\Big(\boldsymbol{\lambda}_n(\boldsymbol{k})\cdot\boldsymbol{E}\Big)\langle \boldsymbol{\mathcal{T}}_\mu\rangle_{n\boldsymbol{k}},\end{aligned} \tag{4.116}$$

where $\langle \boldsymbol{\mathcal{T}}_\mu\rangle_{n\boldsymbol{k}}$ is the torque expectation value of the state computed using Eq. 4.85 and $\mathcal{S}_{\mathcal{BZ}}$ is the surface of the Brillouin zone. From this point we restrict the discussion to the case of two-dimensional systems, for which the integral in Eq. 4.116 is performed on the two-dimensional Brillouin zone. The generalization of the expressions for the torque, spin accumulation and spin fluxes for the three-dimensional case is straightforward. The minus sign in Eq. 4.116 is used to obtain the torque exerted by the electronic state on the magnetization, while the torque operator is defined as the torque exerted by the magnetization on the electronic states.

Because the derivative of the Fermi-Dirac distribution $\frac{\partial f^0(\varepsilon_n(\boldsymbol{k}))}{\partial \varepsilon_n(\boldsymbol{k})}$ is significant only close to the Fermi energy, the domain of integration in Eq. 4.116 can be restricted to narrow regions of k-space enclosing the isoenergy lines. This allows us to decompose the integral into a first integration over the isoenergy lines (Fermi surface) and a second integration in the perpendicular direction. The infinitesimal elements $d^2\boldsymbol{k}$ are then replaced by the elements $dk^{\parallel}$ and $dk^{\perp}$ that are respectively parallel and perpendicular to the isoenergy lines. This yields the expression

$$\boldsymbol{T}_\mu = -\frac{1}{\mathcal{S}_{\mathcal{BZ}}}\sum_n \int_{FS} dk^{\parallel}\int dk^{\perp}\; e\frac{\partial f^0(\varepsilon_n(\boldsymbol{k}))}{\partial \varepsilon_n(\boldsymbol{k})}\Big(\boldsymbol{\lambda}_n(\boldsymbol{k})\cdot\boldsymbol{E}\Big)\langle \boldsymbol{\mathcal{T}}_\mu\rangle_{n\boldsymbol{k}}. \tag{4.117}$$

Replacing the energy derivative of the Fermi-Dirac distribution $\frac{\partial f^0(\varepsilon_n(\boldsymbol{k}))}{\partial \varepsilon_n(\boldsymbol{k})}$ by $-\delta(k^{\perp} - k_{\mathrm{F}})/(\hbar|\boldsymbol{v}_n(\boldsymbol{k})|)$, we can rewrite the torque exerted on atom μ as a Fermi surface integral:

$$\boldsymbol{T}_\mu = \frac{e}{\hbar\mathcal{S}_{\mathcal{BZ}}}\int_{FS}\frac{dk}{|\boldsymbol{v}(\boldsymbol{k})|}\Big(\langle \boldsymbol{\mathcal{T}}_\mu\rangle_{\boldsymbol{k}}\otimes\boldsymbol{\lambda}(\boldsymbol{k})\Big)\boldsymbol{E}. \tag{4.118}$$

The torque in a ferromagnet/heavy metal bilayer usually has a large contribution arising from spin currents. It is therefore very instructive to compare the atom-resolved torques to the spin fluxes on the corresponding atoms. A similar equation to Eq. 4.121 can be found for the spin flux absorbed by the atom μ:

$$\boldsymbol{Q}_\mu = -\frac{e}{\hbar\mathcal{S}_{\mathcal{BZ}}}\int_{FS}\frac{dk}{|\boldsymbol{v}(\boldsymbol{k})|}\Big(\langle \boldsymbol{\mathcal{Q}}_\mu\rangle_{\boldsymbol{k}}\otimes\boldsymbol{\lambda}(\boldsymbol{k})\Big)\boldsymbol{E}, \tag{4.119}$$

and similarly for the spin accumulation induced on atom μ:

$$\boldsymbol{s}_\mu = \frac{e\mu_B}{\hbar\mathcal{S}_{\mathcal{BZ}}}\int_{FS}\frac{dk}{|\boldsymbol{v}(\boldsymbol{k})|}\left(\langle\boldsymbol{\sigma}_\mu\rangle_{\boldsymbol{k}}\otimes\boldsymbol{\lambda}(\boldsymbol{k})\right)\boldsymbol{E}. \tag{4.120}$$

The expectation values for the spin accumulation $\langle\boldsymbol{\sigma}_\mu\rangle_{\boldsymbol{k}}$ and the spin fluxes $\langle\boldsymbol{\mathcal{Q}}_\mu\rangle_{\boldsymbol{k}}$ are computed according to Eqs. 4.80 and 4.94.

We define the response tensors for the torque, $\boldsymbol{t}_\mu$, the spin flux, $\boldsymbol{q}_\mu$ and the spin accumulation, $\boldsymbol{\chi}_\mu$, according to:

$$\boldsymbol{T}_\mu = \boldsymbol{t}_\mu\boldsymbol{E}, \tag{4.121}$$

$$\boldsymbol{Q}_\mu = \boldsymbol{q}_\mu\boldsymbol{E}, \tag{4.122}$$

$$\boldsymbol{s}_\mu = \boldsymbol{\chi}_\mu\boldsymbol{E}. \tag{4.123}$$

All three response tensors are given by:

$$\boldsymbol{t}_\mu = \frac{e}{\hbar\mathcal{S}_{\mathcal{BZ}}}\int_{FS}\frac{dk}{|\boldsymbol{v}(\boldsymbol{k})|}\langle\boldsymbol{\mathcal{T}}_\mu\rangle_{\boldsymbol{k}}\otimes\boldsymbol{\lambda}(\boldsymbol{k}), \tag{4.124}$$

$$\boldsymbol{q}_\mu = -\frac{e}{\hbar\mathcal{S}_{\mathcal{BZ}}}\int_{FS}\frac{dk}{|\boldsymbol{v}(\boldsymbol{k})|}\langle\boldsymbol{\mathcal{Q}}_\mu\rangle_{\boldsymbol{k}}\otimes\boldsymbol{\lambda}(\boldsymbol{k}), \tag{4.125}$$

$$\boldsymbol{\chi}_\mu = \frac{e\mu_B}{\hbar\mathcal{S}_{\mathcal{BZ}}}\int_{FS}\frac{dk}{|\boldsymbol{v}(\boldsymbol{k})|}\langle\boldsymbol{\sigma}_\mu\rangle_{\boldsymbol{k}}\otimes\boldsymbol{\lambda}(\boldsymbol{k}). \tag{4.126}$$

The above atom-resolved response functions provide a deep insight into the mechanisms giving rise to spin-orbit torques in magnetic systems. However, the magnetization dynamics in a ferromagnet is rather driven by the total torque $\boldsymbol{T} = \sum_\mu \boldsymbol{T}_\mu$, since all magnetic atoms are exchange-coupled. Therefore, we also define the total torkance tensor $\boldsymbol{t}$ according to

$$\boldsymbol{T} = \boldsymbol{t}\boldsymbol{E}. \tag{4.127}$$

The total torkance tensor is given by

$$\boldsymbol{t} = \frac{e}{\hbar\mathcal{S}_{\mathcal{BZ}}}\int_{FS}\frac{dk}{|\boldsymbol{v}(\boldsymbol{k})|}\langle\boldsymbol{\mathcal{T}}\rangle_{\boldsymbol{k}}\otimes\boldsymbol{\lambda}(\boldsymbol{k}), \tag{4.128}$$

where we have used the total torque operator $\boldsymbol{\mathcal{T}} = \sum_\mu \boldsymbol{\mathcal{T}}_\mu$.

4.4.1. Finite temperature

In real systems at room temperature, many sources of scattering may exist and not all can be computed explicitly from their corresponding scattering potentials. In particular, the scattering on phonons is crucial to explain room temperature conductivities in metals. In order to mimic the effect of a finite temperature, we add for all states a constant contribution to lifetimes and scattering probabilities.

We thus replace the lifetimes $\tau_{\boldsymbol{k}}$ used in Eq. 4.115 and defined by Eq. 4.67 by $\widetilde{\tau}_{\boldsymbol{k}}$, which we define by the relation

$$\frac{1}{\widetilde{\tau}_{\boldsymbol{k}}} = \frac{1}{\tau_{\boldsymbol{k}}} + \frac{2\Gamma}{\hbar}, \tag{4.129}$$

where Γ has the dimension of an energy and can be set to 25 meV to mimic the effect of room temperature.

The matrix elements $P_{\boldsymbol{k}'\boldsymbol{k}}$ of the scattering-in term in Eq. 4.115 shall be modified in a consistent way, i.e., it must ensure that $\widetilde{\tau}_{\boldsymbol{k}}^{-1} = \sum_{\boldsymbol{k}'} \widetilde{P}_{\boldsymbol{k}'\boldsymbol{k}}$. This condition is fullfilled by the generalized transition rates

$$\widetilde{P}_{\boldsymbol{k}'\boldsymbol{k}} = P_{\boldsymbol{k}'\boldsymbol{k}} + \frac{2\Gamma}{\hbar n(\varepsilon(\boldsymbol{k}'))}\delta(\varepsilon(\boldsymbol{k}) - \varepsilon(\boldsymbol{k}')), \tag{4.130}$$

where $n(\varepsilon)$ is the density of states.

The relaxation times and the transition rates from Eq. 4.129 and 4.130 can be used to compute the effect of specific types of defects or impurities in a system where other sources of scattering exist, as it is the case at room temperature.

5 Results

5.1. SOTs induced by electrical and thermal currents in $L1_0$-FePt/Pt films

The results presented in this section have been published in Ref. [41] and [51].

We present in this section first principles calculations of SOTs driven by electrical and thermal currents in $L1_0$-FePt/Pt thin films. The choice of these materials is motivated by its potential for applications: like the more conventionally studied Co/Pt bilayers [5, 8, 10], $L1_0$-FePt/Pt thin films exhibit a large out-of-plane magnetocrystalline anisotropy energy (MAE) [64], which is desirable for the development of memory devices. The strong advantage of $L1_0$-FePt/Pt over Co/Pt thin films is the good matching of the lattice constants of the materials, which makes it possible to grow these bilayers epitaxially [65, 66]. The ability to grow samples with a very high level of interfacial crystallinity will allow a direct comparison of experimental and theoretical SOTs in order to shade light on the underlying mechanisms.

This section is organized as follows. First, we investigate in Section 5.1.1 the SOTs induced by electrical currents within the Kubo formalism that was described in Section 3.4. Then, we compute in Section 5.1.2 the SOTs induced by thermal currents using the Mott relation as discussed in Section 2.4. Finally, we investigate the SOTs driven by scattering off impurities in disordered $L1_0$-FePt/Pt films using the Boltzmann formalism that was described in Section 4.

5.1.1. Spin-orbit torques driven by electrical currents

Computational details

We consider a system of two layers of $L1_0$-FePt oriented along the [001]-direction and terminated with Fe atoms (Fe/Pt/Fe/Pt/Fe) deposited on a Pt(001) film, see Fig. 5.1, where the number of atomic layers N in the Pt(001) substrate varies from 6 to 18.

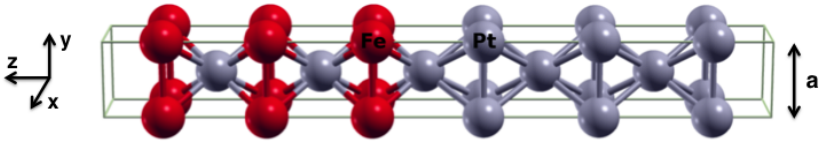

Figure 5.1.: Illustration of 2 layers of $L1_0$-FePt oriented along the [001]-direction and terminated with Fe atoms (Fe/Pt/Fe/Pt/Fe) deposited on a Pt(001) film of 6 layers. We show the Fe and Pt atoms in red and gray respectively. The in-plane lattice constant was set to its experimental value $a = 2.7765\,\text{Å}$.

We compute the electronic structure of the film using the FLEUR code [67] with the Perdew, Burke, and Ernzerhof (PBE) functional. The in-plane lattice constant was set to its experimental value $a = 2.7765\,\text{Å}$ and the out-of-plane coordinates of the atoms were relaxed until forces were smaller than 10^{-5} Hartree/a_0, see Table 5.1. The DFT calculations were performed with 576 k-points in the two-dimensional Brillouin zone. The plane wave cutoff and muffin-tin radii were set respectively to $3.7\,a_0^{-1}$ and $2.4\,a_0$. The atomic magnetic moments for the case $N = 6$ are listed in Table 5.1. We find a magnetic moment for the Fe atoms that varies between 3.02 and $3.08\,\mu_\text{B}$ depending on the layer. The magnetic moment for the Pt atoms in the FePt layer (Pt1 and Pt2) is about $0.4\,\mu_\text{B}$. The induced magnetic moment in the Pt substrate reaches $0.3\,\mu_\text{B}$ in the layer closest to the interface (Pt3).

We have made use of the Wannier interpolation technique to generate the torque, velocity and energy matrix elements for the calculation of the SOT. For this we have used the parallel version of the WANNIER90 code (see Section 3.3.3) to construct 18 MLWFs per atom based on the Bloch states on an 8×8 k-points mesh. The torkances were computed using a 2048×2048 or 4096×4096 k-points mesh depending on the broadening.

The symmetries of the torkance tensor directly reflect the symmetry of the crystal. The C_4 symmetry of $L1_0$-FePt/Pt films implies that the even (Eq. 3.68) and odd (Eq. 3.69) torkances are respectively off-diagonal and diagonal matrices, whose matrix elements follow the relations $t_{yx}^{\text{even}} = -t_{xy}^{\text{even}}$ and $t_{xx}^{\text{odd}} = t_{yy}^{\text{odd}}$.

Even and odd torkances as a function of disorder strength

We first compute the even and odd SOTs for varying disorder strength Γ according to Eqs. 3.68 and 3.69. The results are shown in Fig. 5.2 for different thicknesses of Pt substrate. One clearly observes that the even torkance converges to a finite clean limit value in the limit of $\Gamma \to 0$ corresponding to the Berry curvature expression given by Eq. 2.13. We find that the clean limit value for the even torkance lies in the range of 0.65 to $0.85\,\text{ea}_0$ depending on the substrate thickness. With increasing

atomic layer	d_z	$\Delta(\%)$	μ_{at}^{FLAPW}	μ_{at}^{KKR}
Fe1	1.790	-3.9	3.080	3.060
Pt1	1.869	0.4	0.403	0.363
Fe2	1.862	0.0	3.021	2.934
Pt2	1.874	0.6	0.383	0.337
Fe3	1.816	-2.5	3.040	2.950
Pt3	2.100	3.6	0.297	0.268
Pt4	2.039	0.6	0.047	0.038
Pt5	2.027	0.0	0.022	0.015
Pt6	2.019	-0.4	0.009	0.005
Pt7	1.982	-2.2	0.008	0.006
Pt8			0.007	0.006

Table 5.1.: Computational details for the calculation of the electronic structure of the $L1_0$-FePt/Pt thin films: interlayer distances d_z from one atomic layer to the next one (in units of Å); variation $\Delta = (d_z - d_{ref})/d_{ref}$ of the interlayer distances with $d_{ref} = d_z(Fe2)$ for the first five atomic layers and $d_{ref} = d_z(Pt5)$ for the other ones; atomic magnetic moments μ_{at}^{FLAPW} and μ_{at}^{KKR} (in units of μ_B) obtained respectively with the FLEUR and Jülich KKR codes.

disorder strength these values start to deviate from the Berry curvature value and the dependence on the substrate thickness is reduced. At room temperature, i.e., around $\Gamma = 25\,\text{meV}$, the even torkance is relatively close to the Berry curvature values and lie in the same range as those computed for $Co^3/Pt^{10}(111)$ bilayers [19].

The odd torkance has a very distinct behavior from the even torkance and diverges like $1/\Gamma$ in the limit of $\Gamma \to 0$ in accordance with Eq. 2.14. The odd torkance is larger than the even torkance for disorder strength below 10 meV, but rapidly decays when increasing Γ. At room temperature the magnitude of the odd torkance is about twice as small as the even torkance. At larger values of Γ the odd torkance finally changes sign but its magnitude remains relatively small.

Even and odd torkances as a function of Fermi energy

We now compute the even and odd torkances as a function of the Fermi energy in order to describe the effect of gating or doping the system. The results are shown in Fig. 5.3 for three different thicknesses of Pt substrate and a value of disorder strength $\Gamma = 25$ meV. The even torkance is close to its maximal value at the true Fermi energy and it varies within the range of $[-0.25, +1]\,\text{ea}_0$ depending on the Fermi energy. Overall, the variation of the even torkance in the energy range of $[-0.1, +0.5]\,\text{eV}$ is well reproduced by the "hypothetical" SHE-SOT $\boldsymbol{T}^{SHE}$ given by Eq. 2.3. For the

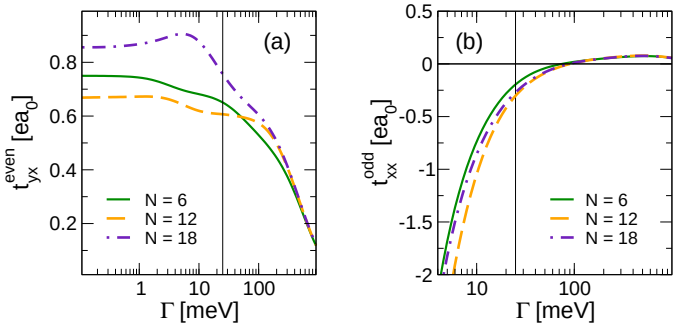

Figure 5.2.: a) Even torkance t_{yx}^{even} and b) odd torkance t_{xx}^{odd} in L1$_0$-FePt^2/Pt^N for N = 6 (green solid), 12 (orange dashed) and 18 (blue dot-dashed). Solid vertical lines correspond to the value of disorder strength $\Gamma = 25$ meV.

geometry of the film considered here the SHE-torkance reads

$$t_{yx}^{\text{SHE}} = S\sigma_{zx}^{y}, \tag{5.1}$$

where σ_{zx}^{y} is the SHE conductivity of Pt and $S = 7.71\,\text{Å}^2$ is the in-plane area of the unit cell. We estimated the intrinsic spin Hall conductivity $\sigma_{zx}^{y} = 2184\,(\hbar/e)$ S/cm from a bulk calculation of fcc Pt employing the Kubo formalism. In the range $[-0.1, +0.5]$ eV the SHE-to-SOT efficiency defined by Eq. 2.4 varies smoothly in the range of $0.5 < \xi < 0.7$ and depends moderately on the substrate thickness. Outside of this range the "hypothetical" SHE-torkance t_{yx}^{SHE} deviates significantly from the first principles torkance and even fails to predict the sign of the torque in several energy windows. Overall, the comparison of our first principles results with the model of SHE-SOT discussed in Section 2.2.1 shows that such models have to be employed with much cautious, but suggests that the spin Hall effect in the Pt substrate is an essential mechanism giving rise to the SOT in that system.

The odd torkance shows a much more pronounced dependence on the Fermi energy as compared to the even torkance. It is of moderate magnitude at the true Fermi energy, while it reaches as much as $4\,\text{ea}_0$ when the Fermi energy is increased by 1 eV. This suggests that an increase of the odd SOT can be achieved by proper engineering of the Fermi level using gating of doping techniques. The dependence on the thickness of the Pt substrate is not especially large except in the energy range of about $[-0.7, -0.3]$ eV, where the odd torkance for the case $N = 6$ is smaller by $1\,\text{ea}_0$ as compared to the cases $N = 12$ and 18.

The band structures of the films are shown in Fig. 5.4 for the cases $N = 6$ and 18, where we have marked the states by the weights of the wave functions on the atoms seating at the interface and at the bottom of the Pt substrate. The bandstructures are overall very similar but we observe in the case of the 6-layer film an hybridization

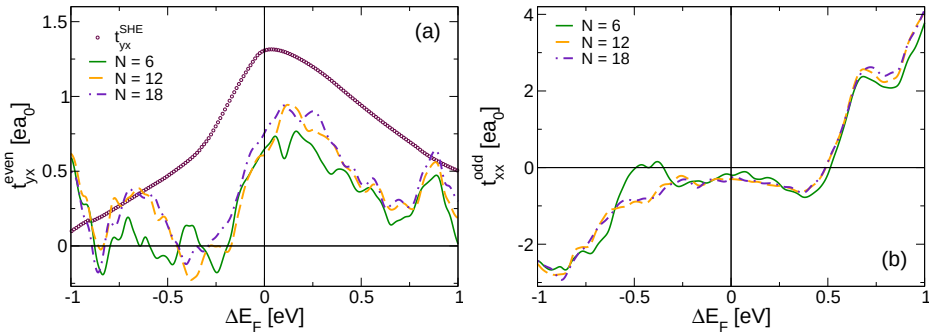

Figure 5.3.: (a) Even torkance t_{yx}^{even} and (b) odd torkance t_{xx}^{odd} as a function of the Fermi energy (with respect to the true Fermi energy $E_{\text{F}} \approx -4.33$ eV for all three thicknesses) at $\Gamma = 25\,\text{meV}$ in L1$_0$-FePt^2/Pt^{N} films for N = 6 (green solid), 12 (orange dashed) and 18 (blue dot-dashed). The line of circles in the (a) corresponds to the SHE-torkance t_{yx}^{SHE} estimated from Eq. (5.1) with a spin Hall conductivity equal to $\sigma_{zx}^{y} = 2184\,(\hbar/e)$ S/cm.

of the states at the interface with those at the bottom of the Pt substrate, see black circles in Fig. 5.4. This hybridization occurs in the energy range of $[-0.7, -0.2]$ eV, i.e., precisely where the odd torkance differs most for the 6-layer film as compared to the 12- and 18-layer films, see Fig. 5.3. This suggests that the cross-talk between the states at the interface and at the bottom of the Pt substrate results in the decrease of the odd torkance observed for the thinnest film.

5.1.2. Thermal spin-orbit torques

We compute now the even and odd thermal torkances using the Mott relation defined by Eq. 2.17 and based on the first principles electrical torkances discussed in the previous section. The results are shown in Fig. 5.5 as a function of the Fermi energy. By comparison with the electrical (Fig. 5.3), it is immediately clear that the thermal torkance is closely related to its electrical counterpart. Indeed, the zeros of the thermal torkance correspond roughly to the local extrema of the electrical torkance and the maximal values for the former correspond to the largest slopes of the latter. This is in agreement with the Mott relation in the limit of $T \to 0$, see Eq. 2.23, where the thermal torkance is directly given by the energy derivative of the electrical torkance. The maximal values of the even torkances are reached around 0.2 eV below the below Fermi energy, while the magnitude of the odd torkance is maximal around 0.6 eV above the Fermi energy. Overall, the even and odd thermal torkances are much more dependent on the thickness of the Pt substrate than its thermal counterpart.

Following the philosophy of the model for the SHE-SOT (Eq. 2.3), one can estimate the "hypothetical" SNE-SOT arising from the spin Nernst effect (SNE) in the

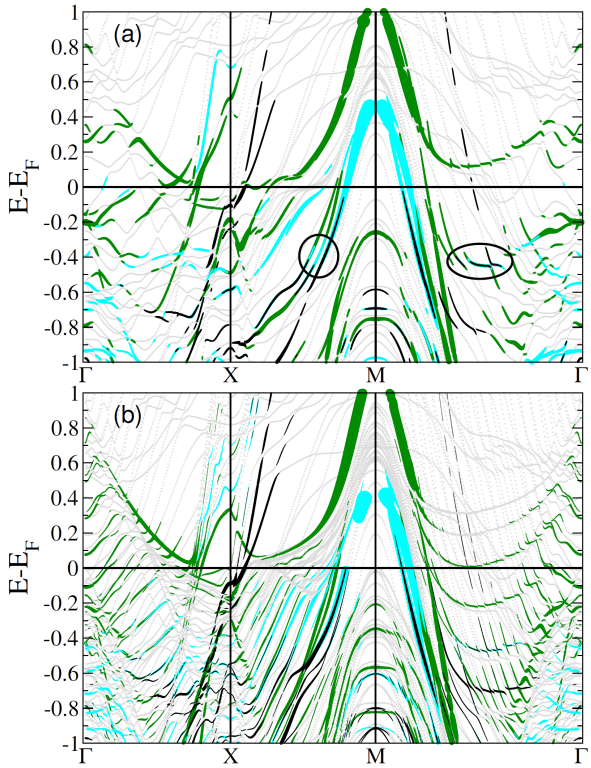

Figure 5.4.: Band structures of (a) $L1_0$-$FePt^2/Pt^6$ and (b) $L1_0$-$FePt^2/Pt^{18}$ thin films. States with large weight of the wavefunction on specific atoms are marked by green (Pt atoms at the bottom of the slab), cyan (Pt substrate atoms closest to the FePt/Pt interface) and black (Fe atoms closest to the FePt/Pt interface). The radius of the dots is proportional to the weight of the wave function on the corresponding atom. (a) States are marked only if the portion of the wave function in a given atomic layer is larger than 9.6% for Pt-atoms and 7.7% for Fe-atoms. (b) These values are reduced to 4.5% for Pt-atoms and 3.6% for Fe-atoms, to account for the twice larger thickness. All states are marked by light gray dots in background. The energy scale is given in eV.

substrate. This is achieved by replacing the spin Hall conductivity σ^s_{zj} by the spin Nernst conductivity β^s_{zj} and the electric field E_j by the applied thermal gradient ∇T_j in Eq. 2.3. For the geometry of the film considered here, this yields for the SNE-torkance the following expression:

$$t^{\mathrm{SNE}}_{yx} = S\beta^y_{zx}, \tag{5.2}$$

where the value of the spin Nernst conductivity $\beta^y_{zx} = -8383\,(\hbar/e)\,\mu\mathrm{A\ cm^{-1}\ K^{-1}}$ was computed from the Mott relation based on the first principles spin Hall conductivity σ^y_{zx}, see line of circles in Fig. 5.3a.

Comparing t^{SNE}_{yx} to the first principles even thermal torkance in Fig. 5.5, we find a good correlation in a range of $[-0.2, +0.6]$ eV around the Fermi energy. Outside of this energy window, the SNE-model fails to predict the variations of the torkance as a function of the Fermi energy and can even fail to predict the sign. Overall, these results demonstrate that the rapid variations of the even thermal torkance as a function of the Fermi energy can only be captured by first principles calculations, but suggests that the SNE is an essential mechanism giving rise to the thermal torkance in $L1_0$-FePt/Pt thin films. Therefore, it might be a promising line of research to consider substrates where SNE is large such as Ir, Pd or Rh, whose spin Nernst conductivities reach as much as -8744, $+20\,804$ and $-20\,779$ $(\hbar e)$ $\mu\mathrm{A\ cm^{-1}\ K^{-1}}$, respectively.

As for the odd thermal torkance, it is of rather small amplitude at the Fermi energy but increases by orders of magnitudes when the Fermi energy is set to ~ 0.6 eV above its true value. In a rough approximation, this can be achieved by considering a $L1_0$-$(Fe_{1-x}Co_x)(Pt_{1-x}Au_x)/Pt_{1-x}Au_x$ film instead of $L1_0$-FePt/Pt, with $x \sim 0.6$ if we assume a constant density of states of $\sim 1\,\mathrm{eV}^{-1}$ per atom for $Fe_{1-x}Co_xPt_{1-x}Au_x$ and $Pt_{1-x}Au_x$.

From the first principles torkances and conductivities, we can conclude that a temperature gradient of the order of ~ 2 K/nm reproduces the same torque as a current density of $\sim 10^7$ A/cm^2. Therefore, although the T-SOT might not be large enough to switch the magnetization in $L1_0$-FePt/Pt thin films, it should be possible to observe the fingerprints of the effect.

5.1.3. Impurity driven spin-orbit torques

In the previous sections, we have considered the SOT and T-SOT in $L1_0$-FePt/Pt thin films within the constant relaxation time approximation, i.e., the same broadening Γ was used for all bands. In the following, we go beyond the constant relaxation time approximation and we compute from first principles the electronic transition rates induced by scattering off impurities. We use the Boltzmann formalism for the SOT discussed in Section 4.4 to compute the current-induced SOT in the presence of

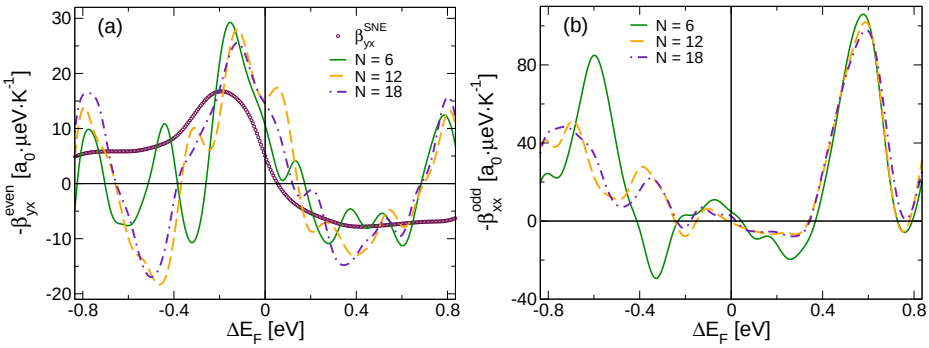

Figure 5.5.: (a) Even thermal torkance t_{yx}^{even} and (b) odd thermal torkance t_{xx}^{odd} as a function of the Fermi energy (with respect to the true Fermi energy $E_{\text{F}} \approx -4.33$ eV for all three thicknesses) at $\Gamma = 25$ meV in $L1_0$-$FePt^2/Pt^N$ films for N = 6 (green solid), 12 (orange dashed) and 18 (blue dot-dashed). The line of circles in the (a) corresponds to the SNE-torkance t_{yx}^{SNE} estimated from Eq. (5.2) with a spin Nernst conductivity equal to $\beta_{zx}^{y} = -8383\,(\hbar/e)\,\mu\text{A cm}^{-1}\text{ K}^{-1}$.

specific types of defects in the $L1_0$-$FePt^2/Pt^6$ layer[1].

The electronic structure of the film was computed with the Jülich KKR code and the VWN functional. The in-plane lattice constant and out-of-plane atomic coordinates are the same as in the previous sections, see Table 5.1. We used an angular momentum cutoff of $l_{\text{max}} = 3$ for the Green functions and the wave functions. We show in Table 5.1 the KKR atomic magnetic moments, which are in good agreement with the FLEUR magnetic moments. The impurity potentials were computed in a cluster of atoms including the first and second nearest neighbors with the Jülich KKR impurity-embedding code (KKRimp) [59]. The Fermi surface is charted by 24 148 k-points in the two-dimensional Brillouin zone.

Scattering due to defects in the FePt ($T = 0$)

We compute the zero-temperature response tensors for the torque, the spin fluxes and the spin accumulation using Eq. 4.124, 4.125 and 4.126 based on the vector mean free path solution of Eq. 4.115. We focus on defects consisting of Fe atoms being replaced

[1] In the constant relaxation time approximation, the Boltzmann torkance (Eq. 4.128) is equivalent to the odd part of the Kubo torkance (Eq. 2.14) in the limit of $T \to 0$. The intrinsic even part of the Kubo torkance (Eq. 2.13) is not captured by the Boltzmann formalism, as it arises from interband transitions. We focus in this section in this section on the dependence of the odd part of the torkance on the details of the disorder in the film.

by Pt atoms and vice versa. In order reproduce experimentally relevant situations, we define three distributions of defects A, B and C shown in Fig. 5.6 (blue shaded areas). In the case A, defects are distributed homogeneously within the FePt layer, while they seat preferentially on the suface or interface side for cases B and C, respectively. The blue shaded areas in Fig. 5.6 define the average number of impurities per unit cell c_m in a given atomic layer m and $\bar{c}_{\text{imp}} = \sum_m c_m$ is the average number of impurities per unit cell for all layers. If not specified otherwise, the impurity distributions are normalized such that $\bar{c}_{\text{imp}} = 0.1$ defects per unit cell. Since the defects are distributed over six atomic layers, this corresponds to an average impurity concentration of 1.7%.

We first discus the zero-temperature response tensor component for the spin accumulation $\chi^{0\text{K}}_{yx,\mu}$. For all impurity distributions we find that the spin accumulation is one order of magnitude larger at the bottom of the film than in the Fe layers, due to the competition of the spin-orbit fields with the strong exchange field in the FePt. Comparing the results for the different defect distributions, we observe that the spin accumulation at the bottom of the film is larger by a factor of 3 for distribution B, owing to the absence of defects in the Pt film in that case. For the atoms of the FePt film, we show in Fig. 5.7 the expectation values of the spin operator $\langle -\boldsymbol{\sigma}_{y\mu}\rangle$ across the Brillouin zone. Overall, we find a larger induced spin polatization for Pt atoms, due to the stronger SOI as compared to Fe atoms. Comparing the induced spin polarization between Pt atoms, we find much larger spin expectation values for Pt3. This is a consequence of the proximity of the Pt3 layer with the Pt substrate that also provides a strong SOI. Comparing Fig. 5.7 and Fig. 5.8, we observe that the sign of the torque expectation values $\langle \mathcal{T}_{x\mu}\rangle$ follows the sign of the spin expectation values $\langle -\boldsymbol{\sigma}_{y\mu}\rangle$, in accordance with Eq. 2.12.

Next, we compute the torkance tensor $t^{0\text{K}}_{xx,\mu}$ for the three defect distributions. Overall, we find a torkance that is much larger on Fe atoms compared to Pt atoms, owing to the much larger magnetic moments (see Table 5.1). This difference in the magnitude of the torkance is directly reflected in the expectation values of the torque operator $\langle \mathcal{T}_{x,\mu}\rangle_{\boldsymbol{k}}$ across the Brillouin zone, see Fig. 5.8. It is interesting to note that the torkance on Pt3 can be as large as on Fe, even though the expectation values $\langle \mathcal{T}_{x,\mu}\rangle_{\boldsymbol{k}}$ of the states at the Fermi energy are much smaller in the case of Pt3. This is a direct consequence of the stronger asymmetry of the local environment seen by Pt3, which seats between the last Fe atom and the Pt substrate. This explains to a large extent that the torkance for Pt3 is much larger than for Pt1 and Pt2, which have a nearly inversion symmetric environment.

Comparing the atom-resolved torkance to the response of the spin fluxes $q^{0\text{K}}_{xx,\mu}$ in Fig. 5.6, we find that the torque on Fe2 and Fe3 is essentially mediated by spin currents, while the torque acting on Fe1 also has local contributions. The deviation of the torkance from the spin flux on Fe1 is the signature of the more pronounced breaking of inversion symmetry at the surface of the film. The spin flux contribution is much larger on Fe3 because of its proximity with the Pt substrate. As for the torque

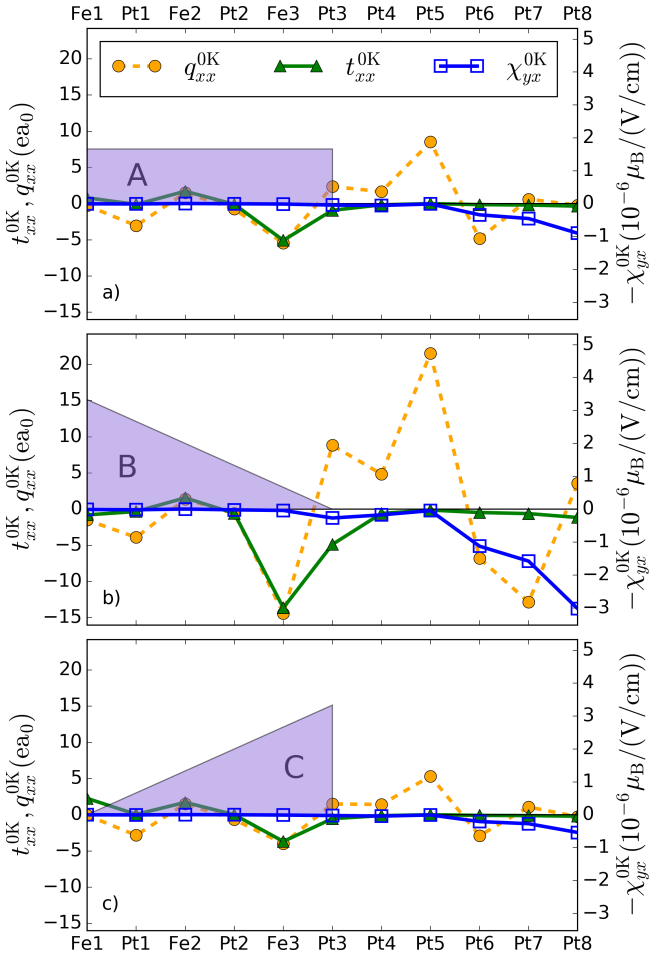

Figure 5.6.: Blue shaded areas give the average number of impurities per unit cell and per atomic layer for distributions A, B and C. The average total number of defects per unit cell is equal to $\bar{c}_{imp} = 0.1$ for all three distributions. The scale for zero-temperature torkances (triangles) and spin-flux response coefficients (circles) is shown on the left. The scale for spin-accumulation response coefficients (squares) is given on the right.

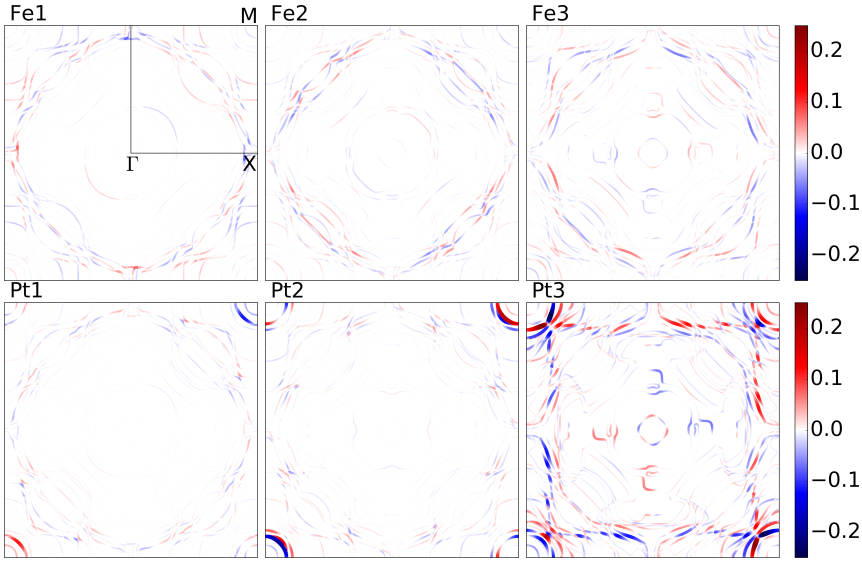

Figure 5.7.: Expectation values $\langle -\boldsymbol{\sigma}_{y\mu} \rangle$ (color code) for $\mu = \{$Fe1, Pt1, Fe2, Pt2, Fe3, Pt3$\}$ for the states at the Fermi surface of the FePt/Pt film. The thickness of the lines is proportional to the absolute values of $\langle -\boldsymbol{\sigma}_{y\mu} \rangle$.

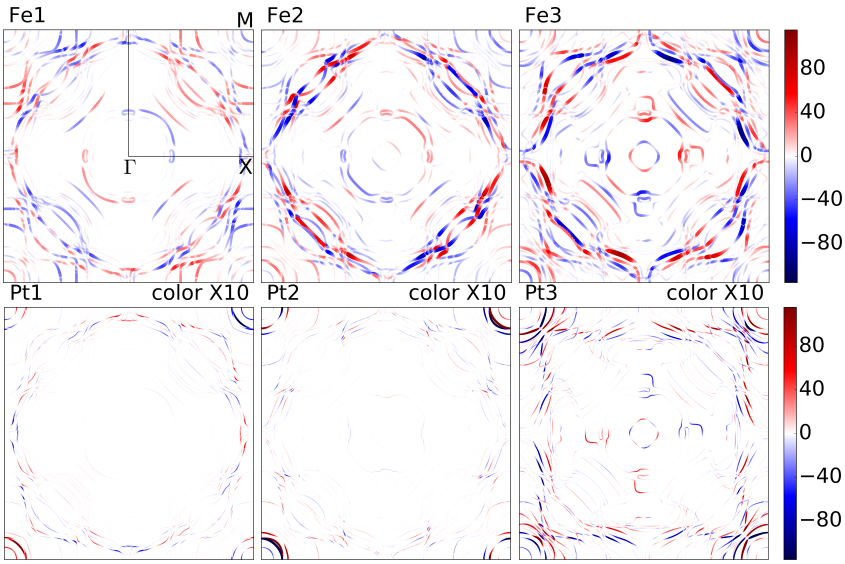

Figure 5.8.: Expectation values $\langle \mathcal{T}_{x\mu} \rangle$ in meV (color code) for $\mu = \{$Fe1, Pt1, Fe2, Pt2, Fe3, Pt3$\}$ for the states at the Fermi surface of the FePt/Pt film. Values are multiplied by a factor of ten for Pt atoms to help visualization.

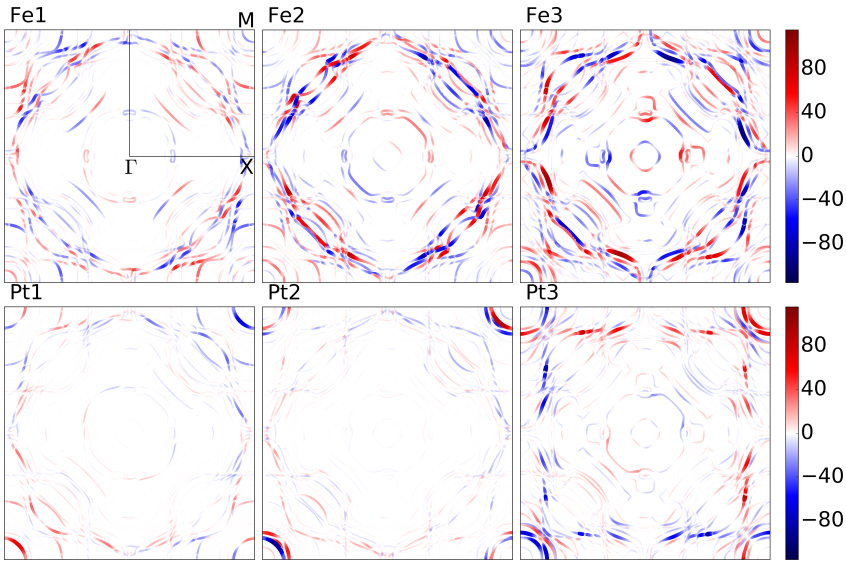

Figure 5.9.: Expectation values $\langle -\mathcal{Q}_{x\mu} \rangle$ in meV (color code) for $\mu = \{$Fe1, Pt1, Fe2, Pt2, Fe3, Pt3$\}$ for the states at the Fermi surface of the FePt/Pt film. The thickness of the lines is proportional to the absolute values of $\langle -\mathcal{Q}_{x\mu} \rangle$.

exerted on the induced magnetization of the Pt layers, there is no clear correlation with the spin fluxes, due to the large angular momentum transferred to the lattice by SOI. This is in accordance with the expectation values of the spin flux operator $\langle -\mathcal{Q}_{x\mu} \rangle$ in Fig. 5.9, which are in agreement with the torque expectation values $\langle \mathcal{T}_{x\mu} \rangle$ in Fig. 5.8 for Fe atoms but not for Pt atoms[2].

It is fruitful to compute the effective magnetic fields that give rise to the same torque as a given current density. This gives a good feeling of the magnitude of the effect and the comparison to experimental results is made easier. We compute the ratio of the effective magnetic field $B_y^{0\mathrm{K}}$ to the current density $j_x^{0\mathrm{K}}$ using the equation

$$\frac{B_y^{0\mathrm{K}}}{j_x^{0\mathrm{K}}} = \frac{1}{M_S} \frac{t_{xx}^{0\mathrm{K}}}{\sigma_{xx}^{0\mathrm{K}}}, \tag{5.3}$$

where M_S is the total magnetic moment per unit cell and $\sigma_{xx}^{0\mathrm{K}}$ is the longitudinal charge conductivity. Interestingly, this ratio is independent of impurity concentration since both quantities scale with the inverse of the concentration. We give in Table 5.2 the values of effective magnetic fields for a current density of $j_x = 10^7 \mathrm{A/cm}^2$ and for

[2]We compare the torque $\langle \mathcal{T}_{x\mu} \rangle$ to the opposite of the spin flux $\langle -\mathcal{Q}_{x\mu} \rangle$ (with a minus sign). This is because the torque operator $\mathcal{T}_{x\mu}$ (Eq. 2.12) is defined as the torque exerted by the magnetization on the electronic states.

impurity distribution	B_y^{0K} (mT)	t_{xx}^{0K} (ea_0)
A	-0.67	-4.5
B	-1.13	-21.5
C	-0.14	-0.7

Table 5.2.: Effective magnetic fields B_y^{0K} for a current density of $j_x = 10^7 \mathrm{A/cm^2}$ and torkances t_{xx}^{0K} for the FePt/Pt film with a concentration of defects per unit cell of $\bar{c}_{\mathrm{imp}} = 0.1$.

the different impurity distributions. We find that the effective magnetic fields vary from -1.13 (case B) to -0.14 mT (case C) depending on the impurity distribution.

The strong dependence of the effective magnetic fields on the impurity distribution can be understood by looking at the atom-resolved torkance in Fig. 5.6. In the case of distribution A, the large negative torque acting on Fe3 dominates the positive torques of smaller magnitude on Fe1 and Fe2, which leads to a negative total torkance of $-4.5\,ea_0$, see Table 5.2. In the case of distribution B, the very large torque acting on Fe3, allowed by the small amount of defects in the Pt3 layer, reaches about $-14\,ea_0$ and the total torkance increases to the value of $-21.5\,ea_0$. For distribution C, the contributions on different atoms cancel to a larger extent than for distributions A and C, which leads to a much smaller torkance equal to $-0.7\,ea_0$. Overall, the strong variation of torkances and effective magnetic fields with the detail of the impurity distribution is a consequence of the torque being the sum of different atomic contributions that partially cancel. The cancellation of the atomic contributions can be tuned by varying the disorder, which leads to a surprisingly large variation of the total torque.

The total torkance can also be decomposed in terms of Fermi surface contributions, as shown in Fig. 5.10. We find that the distribution of the torkance across the Brillouin zone is drastically different in case B as compared to cases A and C. Very large negative contributions to the torkance can be observed in the case B that are almost absent in cases A and C. The very large negative torque acting on the Fe3 atom (see Fig. 5.6) suggests that the corresponding states are located close to the FePt/Pt interface, where disorder is strongly reduced for distributions B. Overall, the variation of the magnetic effective field and of the torkance with the impurity distribution can be explained by a complex interplay of several competing Fermi surface contributions to the SOT. Although the overall distribution of the torkance in the Brillouin zone is rather similar in cases A and C, the total torkance t_{xx}^{0K} is about 6 times larger for distribution A, which we explain by a larger unbalance between positive and negative contributions in case A. To conclude on the zero-temperature torkance in FePt/Pt films, we want to stress the importance of a first principles description of the exchange field in the ferromagnetic layer. Comparing the contributions of the states at

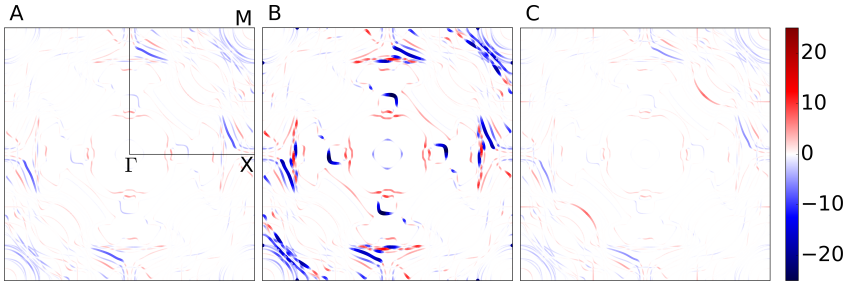

Figure 5.10.: Distribution of $\langle \mathcal{T}_x \rangle_{\boldsymbol{k}} \lambda_x(\boldsymbol{k})/|\boldsymbol{v}(\boldsymbol{k})|$ in the Brillouin zone, in units of $\hbar$, for an FePt/Pt film with a concentration of defects per unit cell of $\bar{c}_{\text{imp}} = 0.1$. The impurity distributions A, B and C are shown in Fig. 5.6.

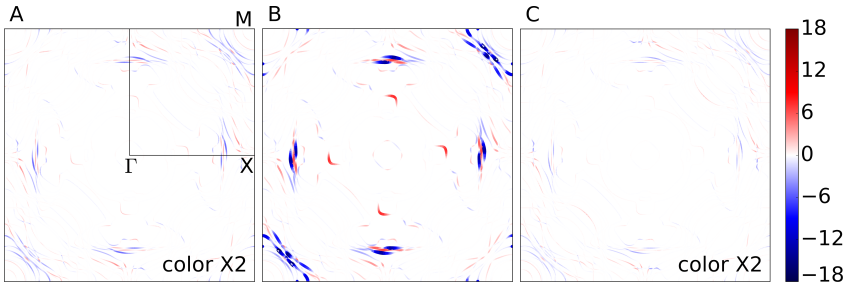

Figure 5.11.: Distribution of $\langle -\boldsymbol{\sigma}_{y,\text{FePt}} \rangle_{\boldsymbol{k}} \, \lambda_x(\boldsymbol{k})/|\boldsymbol{v}(\boldsymbol{k})|$ in the Brillouin zone, in units of $100 \times \hbar/\text{Ry}$, for an FePt/Pt film with a concentration of defects per unit cell of $\bar{c}_{\text{imp}} = 0.1$. The spin operator $\boldsymbol{\sigma}_{y,\text{FePt}}$ gives the spin of a state that is localized on Fe1, Pt1, Fe2, Pt3, Fe3 or Pt3. The impurity distributions A, B and C are shown in Fig. 5.6.

the Fermi energy to the response tensors for the torque (Fig. 5.10) and for the spin accumulation in the FePt film (Fig. 5.11), we observe that the spin accumulation alone do not explain the magnitude of the computed torque and fails to predict the sign for many bands. Therefore, the naive approximation of a constant exchange field in the FePt layer would give a poor estimate of the torque.

Defects in FePt at room temperature ($\Gamma = 25\,\mathrm{meV}$)

At room temperature additional sources of scattering are present such as phonons. In the following, we investigate the interplay between the scattering off impurities and other sources of scattering. The former is computed from first principles as discussed in the previous section, while the later is treated within the constant relaxation time approximation. We compute the relaxation times and the electronic transition rates using Eqs. 4.129 and 4.130 with a disorder strength $\Gamma = 25\,\mathrm{meV}$ to include the effect of room temperature.

We show in Fig. 5.12 the room temperature torkance $t^{\mathrm{RT}}_{xx,\mu}$ and the response of the spin accumulation $\chi^{\mathrm{RT}}_{yx,\mu}$ for room temperature. As compared to the zero temperature values, we find that the spin accumulation is reduced by a factor of 100 for case B and a factor of 25 for case C. The values for case A are intermediate between cases B and C, we therefore omit them in Fig. 5.12 for clarity. Overall, we find that the strong differences in the zero temperature values between impurity distributions is washed out by the inclusion of the additional finite disorder strength Γ. This is consistent with the values of the impurity-induced relaxation times being such that $\hbar/2\tau^{av}_{0\mathrm{K}}$ is always smaller than $8\,\mathrm{meV}$, i.e., much smaller than the broadening induced by room temperature. The same trend is observed for the room temperature torkance $t^{\mathrm{RT}}_{xx,\mu}$, which is reduced by a factor of 15 and 5 for distributions B and C, as compared to the zero temperature case. Overall, the scattering off impurities at room temperature tends to reduce the magnitude of the torkance and the spin accumulation as compared to the CRTA case, see Fig. 5.12. However, the variations between different distributions is of moderate amplitude.

We show in Fig. 5.13 the effective magnetic field and the total torkance as a function of impurity concentration. Within the range of concentration considered, we find a pronounced dependence of the SOT on the concentration of impurities, which stands in sharp contrast with the rather moderate differences in the individual atomic contributions (Fig. 5.12). This paradox can be explained by the observation that the atomic contributions to the SOT in the ferromagnetic layer partially cancel out in the CRTA case, leading to a total SOT of reduced amplitude. Depending on the distribution of impurities, the cancellation of atomic contributions is either enhanced or reduced, which leads to a strong variation of the total torkance or effective magnetic field in Fig. 5.13. In the case B, this mechanism leads to a strong increase of the torkance, which is a very counter-intuitive result and stands in sharp contrast with the case of longitudinal conductivity.

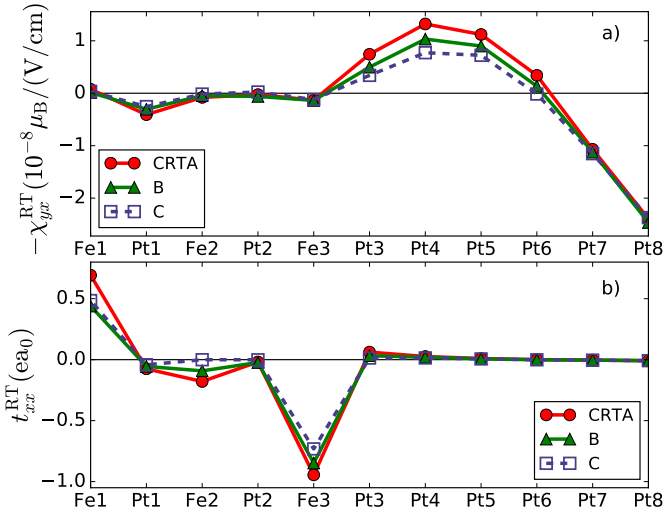

Figure 5.12.: (a) Response coefficient of the spin accumulation, and (b) torkance, computed for three different types of disorder: (squares) constant relaxation time, i.e. $P_{\boldsymbol{k}'\boldsymbol{k}} = 0$ in Eq. (4.130); (triangles) defects located preferentially at the surface, case B; (circles) defects located preferentially at the interface, case C. The concentration of defects per unit cell is equal to $\bar{c}_{imp} = 0.1$ for cases B and C. All calculations where performed setting $\Gamma = 25$ meV in Eq. (4.130).

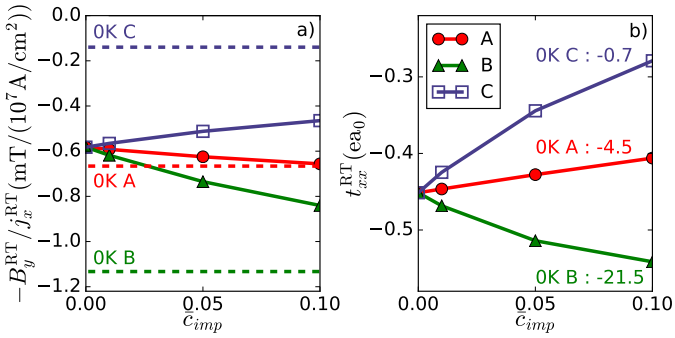

Figure 5.13.: (a) Effective fields per unit of current density, and (b) total torkances, computed as a function of defect concentration for distributions A, B and C. Horizontal dashed lines and numbers stand for the 0K values, computed with $\bar{c}_{\mathrm{imp}} = 0.1$ for total torkances. Full lines show the values at room temperature, i.e., using Eq. (4.130).

5.2. Influence of doping by various impurities in Co/Cu films

The results presented in this section have been published in Ref. [51].

In this section we investigate the SOT in a single layer of Co deposited on a six-layer Cu(111) film (Fig. 5.14) and the effect of doping with light (C, N) and heavy (Bi, Ir) impurities. This study is motivated by the experimental and theoretical findings that Ir and Bi impurities have a huge impact on the spin-dependent transport properties of Cu [43, 44, 46]. Therefore, the question arises whether the spin-orbit torque in a ferromagnetic layer deposited on a Cu substrate can be tuned with the amount and type of doping impurities.

We compute the electronic structure of the film with the Jülich KKR code and the VWN functional. The in-plane lattice constant was set to $a/\sqrt{2} = 2.556\,\text{Å}$, where $a = 3.615\,\text{Å}$ is the lattice constant of bulk fcc Cu. The distance between Cu layers was set to $a/\sqrt{3} = 2.087\,\text{Å}$. The distance between the Co layer and the first Cu layer was set to $1.959\,\text{Å}$, which was obtained by relaxation of the Cu/Co interface [68]. Interlayer distances are summarized in Table 5.3. The angular momentum cutoff was set to $l_{\max} = 3$ for the Green functions and the wave functions. The magnetic moment of the Co atom is equal to $1.664\,\mu_{\text{B}}$ and the induced magnetic moments in the Cu substrate are negligible, see Table 5.3. The impurity potentials were computed in a cluster of atoms including the first and second nearest neighbors with the Jülich KKR impurity-embedding code (KKRimp) [59]. The Fermi surface is charted by 15 810 k-points in the Brillouin zone.

Scattering due to impurities ($\Gamma = 0$)

We show in Fig. 5.15 the zero-temperature response coefficients for the torque, $t_{xx}^{0\text{K}}$, the spin accumulation, $\chi_{yx}^{0\text{K}}$, and the spin fluxes, $q_{xx}^{0\text{K}}$, in the presence of Bi, Ir, C or

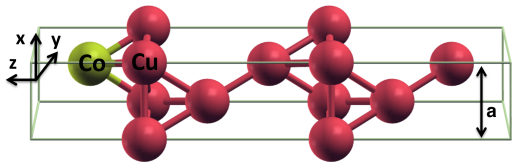

Figure 5.14.: Illustration of the unit cell of one layer of Co deposited on six layers of Cu(111). Co and Cu atoms are shown in yellow and red respectively. The in-plane lattice constant and out-of-plane distance are given in the text.

atomic layer	d_z	μ_{at}
Co	1.959	1.664
Cu1	2.087	0.004
Cu2	2.087	-0.010
Cu3	2.087	-0.003
Cu4	2.087	-0.004
Cu5	2.087	-0.004
Cu6	2.087	0.000

Table 5.3.: Computational details for the calculation of the electronic structure of the Co/Cu thin films: interlayer distances d_z from one atomic layer to the next one (in units of Å) and atomic magnetic moments μ_{at} obtained within the Jülich KKR code (in units of μ_B).

N impurities in the Co/Cu film. We consider the case of a homogeneous distribution of impurities, i.e., the average number of impurities is the same for all Co and Cu atomic layers, see blue shaded areas in Fig. 5.15. If not specified otherwise, the impurity distributions are normalized such that the average number of impurities per unit cell is equal to 0.1 for all impurity types.

We fist discuss the zero-temperature response tensor for the spin accumulation χ_{yx}^{0K}. We find that the spin accumulation at the bottom of the film is three orders of magnitude smaller than in the case of the FePt/Pt film (Section 5.1), due to the smaller spin-orbit interaction in Cu and to the presence of impurities in the Cu layers. For Bi, C and N impurities, the spin accumulation is positive in all layers. On the Co layer, it reaches 0.00, 0.34 and $0.18 \times 10^{-9}\mu_B/(V/cm)$ for Bi, C and N impurities respectively. The situation is quite different in the case of Ir impurities, where the spin accumulation is negative in most layers, in particular on the Co layer where it reaches $-2.61 \times 10^{-9}\mu_B/(V/cm)$.

The torkance follows the general trend of the spin accumulation. It reaches $0.4\,ea_0$ for Ir impurities, $-0.1\,ea_0$ for C and N impurities, and vanishes for Bi impurities. In contrast to the FePt/Pt film (Section 5.1), the torque in entirely exerted on the ferromagnetic Co layer itself and the torkance on the very small induced magnetization ($\sim 0.004\,\mu_B$) of the neighboring Cu layer is negligible. The variation of the spin fluxes in the region close to the interface (Co, Cu1, Cu2) indicates that angular momentum is taken from the lattice in the Cu layers (where spin fluxes are negatives) and transferred to the Co layer (where spin fluxes are positive). The spin flux in the Co layer is of similar order of magnitude as the torkance. However, the spin flux does not correlate with the torkance on the Co layer for any of the impurity types. This clearly demonstrates that a large part of the SOT in Co/Cu films arises from the local SOI on the Co atoms. This is a strong difference with the FePt/Pt films where

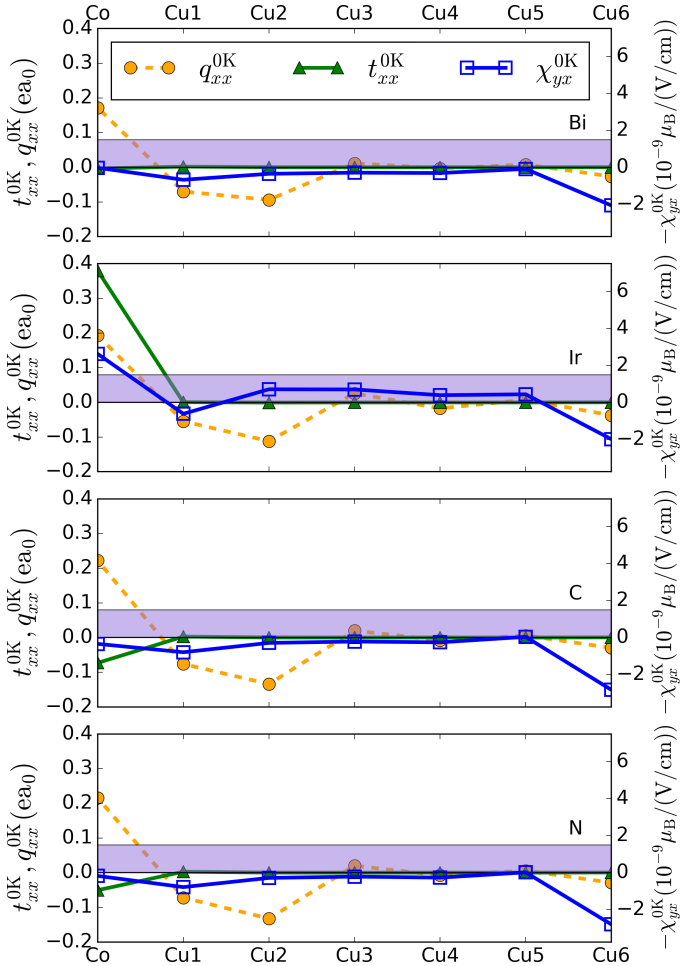

Figure 5.15.: Blue shaded areas mark the homogeneous distributions of Bi, Ir, C and N impurities. The concentration of impurities per unit cell is equal to $\bar{c}_{imp} = 0.1$ for all distributions. The scale for zero temperature torkance (triangles) and spin-flux response coefficient (circles) is shown on the left. The scale for the spin-accumulation response coefficent (squares) is given on the right.

Impurity type	$B_y^{0\mathrm{K}}$ (mT)	$t_{xx}^{0\mathrm{K}}$ (ea_0)
Bi	0.00	0.00
Ir	1.61	0.38
C	−0.33	−0.07
N	−0.22	−0.05

Table 5.4.: Effective magnetic fields $B_y^{0\mathrm{K}}$ for a current density of $j_x = 10^7\,\mathrm{A/cm^2}$ and torkances $t_{xx}^{0\mathrm{K}}$ for the Co/Cu film with a concentration of impurities per unit cell of $\bar{c}_{\mathrm{imp}} = 0.1$.

the SOT originates essentially from spin currents generated in the substrate.

We show in Table 5.4 the total torkances and effective magnetic fields for Bi, Ir, C and N impurity distributions. The very strong dependence of the SOT on the impurity type can be related to the FS contributions to the torkance shown in Fig. 5.16. In the case of C and N impurities, the torkance is dominated by states in the outer part of the Brillouin zone, which yields total torkances of -0.07 and $-0.05\,\mathrm{ea}_0$ for C and N impurities, respectively. In the case of Bi impurities, the contributions from the outer part of the Brillouin zone are strongly suppressed, due to the larger scattering cross-section of Bi impurities as compared to C and N impurities. As a result, the total torkance vanishes by cancellation of the contributions from different states in the Brillouin zone. The situation is very different for Ir impurities, where an additional contribution to the torkance arises from a FS loop around the Γ point, resulting in a much larger positive total torkance of $0.38\,\mathrm{ea}_0$ in that case. Given the similar atomic numbers of Ir and Bi, the large difference in the induced torkances is rather surprising. The fact that Ir and Co have similar valence shells, respectively, $5\mathrm{d}^7 6\mathrm{s}^2$ and $5\mathrm{d}^7 6\mathrm{s}^2$, provides an explanation for the weaker scattering induced by Ir impurities in Co, as compared to Bi impurities.

To conclude our study of the zero-temperature spin-orbit torques in Co/Cu bilayers, we show in Fig. 5.17 the contribution of the states at the Fermi energy to the current-induced spin accumulation on the Co layer. We find that the overall distribution of the spin accumulation across the Brillouin zone closely follows the distribution of the torkance (Fig. 5.16). This stands in sharp contrast to the case of the FePt/Pt film (Section 5.1), where the spin accumulation and the torque differ even in sign at many k-points, due to the much more complex structure of the exchange field in FePt as compared to a Co monolayer. Overall, we conclude that doping with different types of impurities provide a very powerful mean to engineer both the spin accumulation and the SOT in ferromagnetic heterostructures.

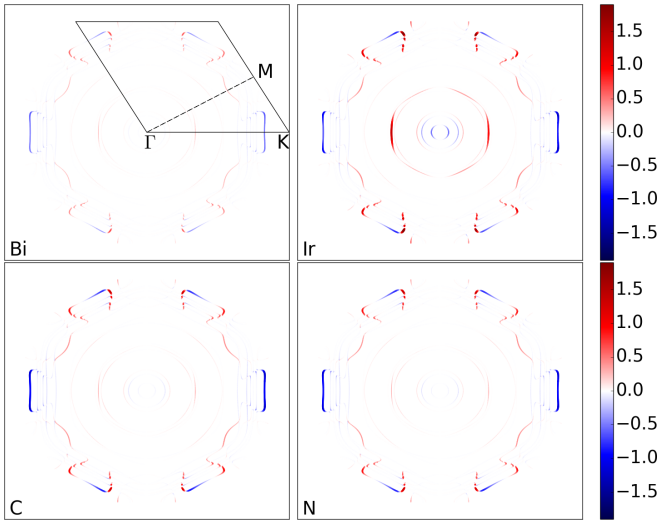

Figure 5.16.: The total torkance in terms of the Fermi surface distribution of $\langle \mathcal{T}_x \rangle_{\boldsymbol{k}} \lambda_x(\boldsymbol{k})/|\boldsymbol{v}(\boldsymbol{k})|$ [see Eq. (4.128)], in units of $\hbar$, for a Co/Cu film with a concentration of Bi, Ir, C or N impurities per unit cell of $\bar{c}_{imp} = 0.1$. The irreducible Brillouin zone is shown by solid lines and the dashed line is a guide to the eyes.

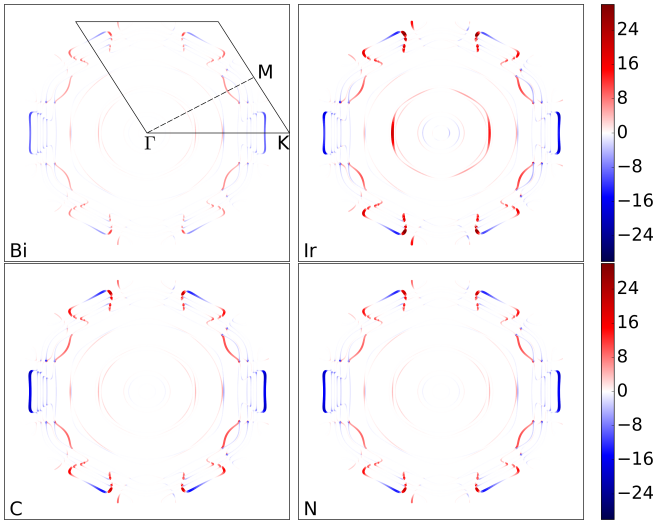

Figure 5.17.: Distribution of $\langle -\boldsymbol{\sigma}_{y,\mathrm{Co}} \rangle_{\boldsymbol{k}} \, \lambda_x(\boldsymbol{k})/|\boldsymbol{v}(\boldsymbol{k})|$ in the Brillouin zone, in units of $\hbar/\mathrm{Ry}$, for a Co/Cu film with a concentration of Bi, Ir, C or N impurities per unit cell of $\bar{c}_{imp} = 0.1$.

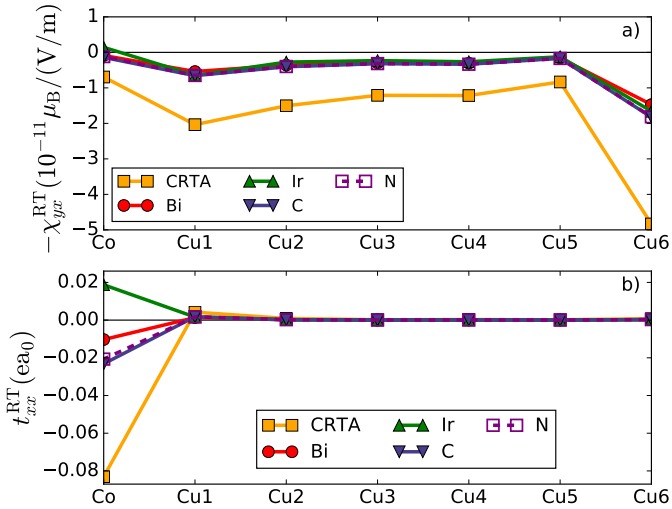

Figure 5.18.: (a) Response coefficient of the spin accumulation, and (b) torkance, in a Co/Cu film for the clean system in CRTA (full squares), and in the presence of Bi (circles), Ir (triangles up), C (triangles down) and N (open squares) impurities. The concentration of impurities per unit cell is equal to $\bar{c}_{imp} = 0.1$ for all impurity types. All calculations where performed with $\Gamma = 25\,\mathrm{meV}$ in Eq. (4.130).

Impurities at room temperature ($\Gamma = 25\,\mathrm{meV}$)

In the following we investigate the effect of impurities at room temperature, when other sources of scattering exist. In analogy to Section 5.1.3, we compute the relaxation times and scattering rates from Eqs. 4.129 and 4.130 with a disorder strength $\Gamma = 25\,\mathrm{meV}$ that accounts for the effect of room temperature. We present the room temperature (RT) spin accumulation coefficients χ_{yx}^{RT} and torkances t_{xx}^{RT} in Figs. 5.18 and 5.19.

As shown in Fig. 5.18, the spin accumulation in the Co/Cu film is reduced by about two orders of magnitude as compared to the zero temperature case. The sign of the spin accumulation is consistent with the zero temperature calculations, i.e., it is positive in all layers for Bi, C and N impurities, but it is negative in the Co layer for Ir impurities. The same trend is observed for the torkance, which is negative for Bi, C and N impurities but positive for Ir impurities. Overall, the variation of the zero-temperature torkance with the type of impurity is strongly reduced by the addition of the constant smearing $\Gamma = 25\,\mathrm{meV}$. However, the variation is more pronounced than for the FePt/Pt film studied in Section 5.1.3, especially when comparing the case of Ir impurities to the case of Bi, C and N impurities.

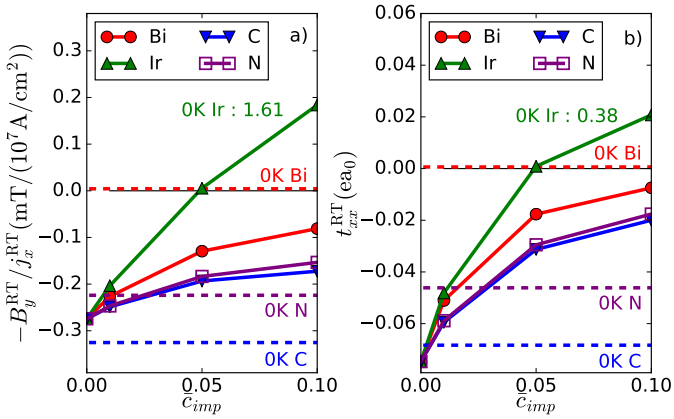

Figure 5.19.: (a) Effective fields per unit of current density, and (b) total torkances, computed as a function of concentrations of Bi, Ir, C and N impurities. Horizontal dashed lines and numbers stand for the 0K values, computed with $\bar{c}_{\mathrm{imp}} = 0.1$ for total torkances. Full lines show the values at room temperature, i.e., using Eq. (4.130).

We show in Fig. 5.19 the total torkance and effective magnetic field as a function of impurity concentration. The torque is affected in two ways by the presence of impurities. On the one hand, the torkance tends to decrease as a function of the impurity concentration, owing to the reduced relaxation times. For an average number of impurities of $\bar{c}_{\mathrm{imp}} = 0.1$, it results in a torkance reduced by a factor of 10 for Bi impurities and a factor of 4 for C and N impurities. On the other hand, the scattering induced by impurities tends to push the torkance and effective magnetic field toward the zero temperature values, resulting in the splitting of the curves observed in Fig. 5.19. In the case of Ir impurities, the splitting is so large that it changes the sign of the SOT.

In summary, our results clearly demonstrate that doping with proper type and amount of impurities provides a powerful mean to tailor the SOT in magnetic thin films for a given application. Astonishingly, even the sign of the SOT can be changed at room temperature and the effective magnetic fields per unit of current density follow the trend of the zero-temperature values, which are independent of impurity concentration.

5.3. Contributions from the Rashba effect to the SOT in $Ag_2Bi/Ag/Fe$

In this section we investigate the spin-orbit torque in a Ag_2Bi-terminated Ag(111) film grown on ferromagnetic Fe(110). This system has been proposed by Carbone *et al.* [69] as an ideal system to study the interplay of exchange and spin-orbit Rashba interactions. On the one hand, the Ag_2Bi alloy at the surface is known to have Rashba bands with an extremely large spin splitting [70]. On the other hand, the quantum well states in Ag are exchange-split due to the neighboring ferromagnetic Fe. The simultaneous breaking of time reversal and spatial inversion symmetry yields a k-asymmetric band structure, where the asymmetry arises from the relative orientation of the spin-orbit and exchange fields.

It has been suggested by Carbone *et al.* [69] that the peculiar asymmetry of the band structure in this system can have a strong effect on transport properties. The current-induced magnetization precession has been investigated by Jungfleisch *et al.* in a similar stack of Bi/Ag/Py [71]. In their paper they suggest that the Rashba effect at the Bi/Ag interface generates a spin-current flowing out-of-plane that drives the magnetization precession in the Py. However, the origin of the torque acting on the ferromagnet in an experiment can be only indirectly inferred and the distribution of the spin currents within the thickness of the stack can not be measured. Therefore, first principles calculations of the SOT in that system would be very valuable.

In the following we perform a first-principles investigation of the transport properties of the $Ag_2Bi/Ag/Fe$ system originally proposed by Carbone *et al.* [69]. We use the Boltzmann formalism discussed in Section 4.4 to compute the spin-orbit torques and the spin fluxes in order to shed light on the underlying mechanisms.

5.3.1. Electronic structure

We use the Jülich KKR code to compute the electronic structure of the film using the VWN functional. We construct a film that contains 5 layers of Fe(110), 9 layers

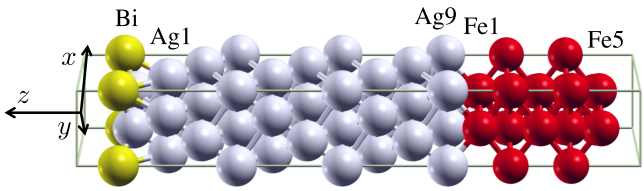

Figure 5.20.: Illustration of the unit cell of a Ag_2Bi-terminated Ag(111) film grown on ferromagnetic Fe(110). Bi, Ag and Fe atoms are shown in yellow, gray and red respectively. Atomic coordinates are given in Table 5.5.

atom	x	y	z	μ_{at}	atom	x	y	z	μ_{at}
Fe	-2.165	1.250	-31.528	2.95	Ag	0.000	0.000	-14.147	0.00
Fe	0.721	1.250	-31.528	2.95	Ag	-1.443	2.500	-14.147	0.00
Fe	-0.721	3.751	-31.528	2.95	Ag	1.443	2.500	-14.147	0.00
Fe	0.000	0.000	-29.499	2.70	Ag	0.000	1.667	-11.789	0.00
Fe	-1.443	2.500	-29.499	2.70	Ag	-1.443	4.168	-11.789	0.00
Fe	1.443	2.500	-29.499	2.70	Ag	1.443	4.168	-11.789	0.00
Fe	-2.165	1.250	-27.471	2.69	Ag	0.000	3.334	-9.431	0.00
Fe	0.721	1.250	-27.471	2.69	Ag	-1.443	5.835	-9.431	0.00
Fe	-0.721	3.751	-27.471	2.69	Ag	1.443	5.835	-9.431	0.00
Fe	0.000	0.000	-25.442	2.69	Ag	0.000	0.000	-7.073	0.00
Fe	-1.443	2.500	-25.442	2.69	Ag	-1.443	2.500	-7.073	0.00
Fe	1.443	2.500	-25.442	2.69	Ag	1.443	2.500	-7.073	0.00
Fe	-2.165	1.250	-23.413	2.83	Ag	0.000	1.667	-4.715	0.00
Fe	0.721	1.250	-23.413	2.83	Ag	-1.443	4.168	-4.715	0.00
Fe	-0.721	3.751	-23.413	2.83	Ag	1.443	4.168	-4.715	0.00
Ag	0.000	0.000	-21.220	0.00	Ag	0.000	3.334	-2.357	0.00
Ag	-1.443	2.500	-21.220	0.00	Ag	-1.443	5.835	-2.357	0.00
Ag	1.443	2.500	-21.220	0.00	Ag	1.443	5.835	-2.357	0.00
Ag	0.000	1.667	-18.862	0.00	Bi	0.000	0.000	0.849	0.00
Ag	-1.443	4.168	-18.862	0.00	Ag	-1.443	2.500	0.000	0.00
Ag	1.443	4.168	-18.862	0.00	Ag	1.443	2.500	0.000	0.00
Ag	0.000	3.334	-16.504	0.00					
Ag	-1.443	5.835	-16.504	0.00					
Ag	1.443	5.835	-16.504	0.00					

Table 5.5.: Computational details for the calculation of the electronic structure of the Co/Cu thin films: x, y and z Cartesian atomic coordinates (in units of Å) and atomic magnetic moments μ_{at} obtained within the Jülich KKR code (in units of μ_{B}). The direct Bravais vectors in Cartesian coordinates are defined by $\boldsymbol{a} = (4.331, 3.334, 0)$ and $\boldsymbol{b} = (-4.331, 3.334, 0)$ (in units of Å).

of Ag(111) and one layer of Ag_2Bi in accordance with Ref. [69], see Fig. 5.20. The atomic coordinates are given in Table 5.5 along with the atomic magnetic moments. In order to include the Ag_2Bi layer in the calculation, it is necessary to use a supercell of 3 atoms per atomic layer, i.e., a total number of 45 atoms per unit cell[3].

We show in Fig. 5.21a and Fig. 5.21b the band structure for k-vectors respectively parallel and perpendicular to magnetization direction (see Fig 5.22b for an illustration of the corresponding k-paths P-Γ-P' and K-Γ-K'). We find that the band structure is k-symmetric for k-vectors parallel to magnetization direction (path P-Γ-P') while it is strongly k-asymmetric for the other case (path K-Γ-K'). Overall, the electronic structure is very complex with a large number of bands crossing the Fermi energy. The k-asymmetry is even more pronounced for the local density of states on the Ag_2Bi layer, shown in Fig. 5.21c and Fig. 5.21d. The Rasbha bands are clearly symmetric along the P-Γ-P' path and strongly asymmetric along the K-Γ-K' path. The asymmetry of the bands is illustrated in a most prominent way by the asymmetric band-gap openings observed along the K-Γ-K' path. An example of asymmetric band-gap opening is marked by the letter A in Fig. 5.21d.

The different symmetries of the Rashba bands along P-Γ-P' and K-Γ-K' paths can be explained by the relative orientation of the exchange field with the Rashba spin-orbit fields. According to the symmetry of the Rashba bands illustrated in Fig. 2.2b, the spin-orbit field is always perpendicular to the k-vector and rotates either clockwise or anti-clockwise depending on the band. This implies that the spin-orbit fields are always parallel to the exchange field along the K-Γ-K' path, but their relative direction depends on the sign of the k-vector. This leads to a strong asymmetry of the bands along the K-Γ-K' path, which is not possible along the P-Γ-P' path where spin-orbit fields are always perpendicular to the exchange field.

As observed in Figs. 5.21c and 5.21d the Fermi energy in that system is located almost exactly at the top of the Rashba bands. We show in Fig. 5.22a the states at the Fermi energy marked by the portion of their wave functions located on the Ag_2Bi layer. The symmetry of the weights along the P-Γ-P' and K-Γ-K' is consistent with the spectral density of states (Fig. 5.21c and Fig. 5.21d), i.e., the weights are symmetric along the P-Γ-P' path but very asymmetric along the K-Γ-K' path. On the one hand, the states for the band closest to the Γ point are located on the Ag_2Bi layer at more than 75% and they follow the nearly circular shape expected for a Rashba band. On the other hand, the next states found when moving away from the Γ point are strongly asymmetric and overall have a smaller weight on the Ag_2Bi layer.

We show in Fig. 5.22b the states at the energy 930 meV below the Fermi energy marked by the portion of their wave functions located on the Ag_2Bi layer. As ob-

[3]The screened KKR formalism is the method of choice for systems of this size because it scales linearly with the number of atoms.

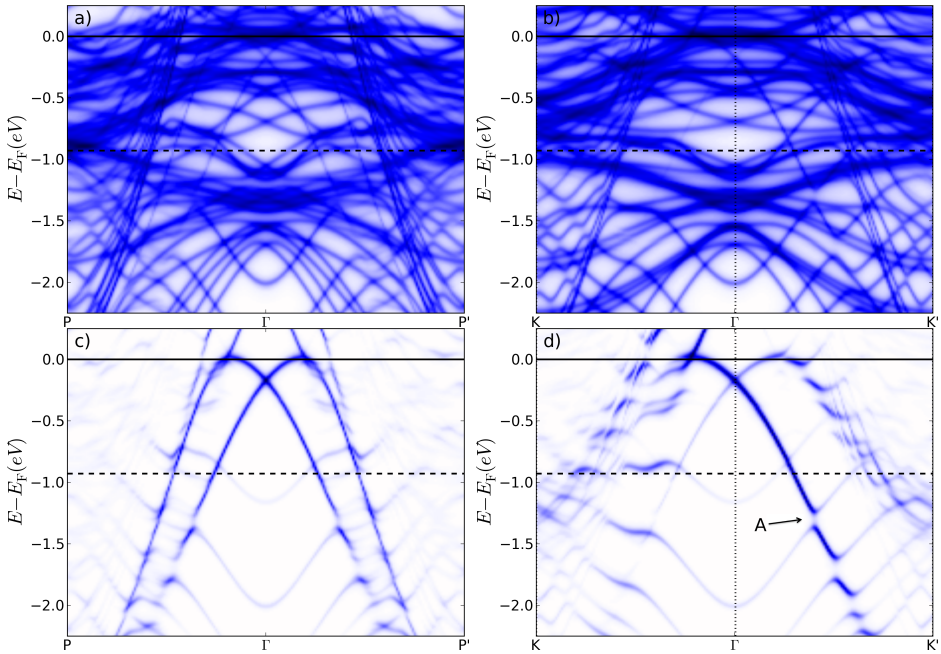

Figure 5.21.: (a,b) Spectral density of states for a Ag_2Bi-terminated Ag film grown on ferromagnetic Fe(110) along the two different k-paths shown in Fig. 5.22. (c,d) Corresponding local density of states on the Ag_2Bi layer. An example of asymmetric band-gap opening is marked by the letter A.

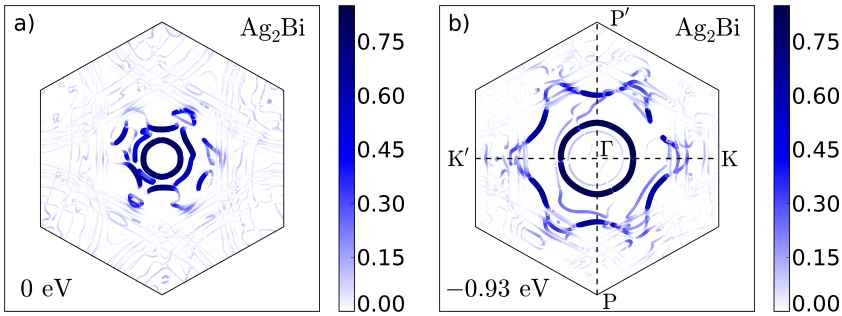

Figure 5.22.: (a) States at the Fermi energy and (b) 930 meV below the Fermi energy marked by the portion of their wave functions located on the Ag_2Bi layer.

served in Figs. 5.21c and 5.21d (dashed lines), both Rashba bands are present at this value of energy and their asymmetry along the K-Γ-K' path is large. Overall, the

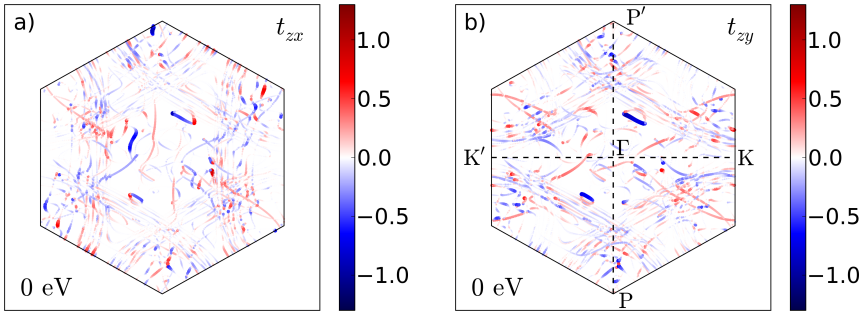

Figure 5.23.: Distribution of (a) $\mathcal{T}_z(\boldsymbol{k})\lambda_x(\boldsymbol{k})/|\boldsymbol{v}(\boldsymbol{k})|$ and (b) $\mathcal{T}_z(\boldsymbol{k})\lambda_y(\boldsymbol{k})/|\boldsymbol{v}(\boldsymbol{k})|$ in the Brillouin zone in units of $\hbar$. The Fermi energy is set to its true value.

distribution of the states in the Brillouin zone shown in Fig. 5.22b is very similar to the case of the Rashba model (Fig. 2.2b), i.e., it consists mainly of two bands of nearly circular shapes. However, the first principles electronic structure captures the fine details of the hybridization of the Rashba bands with the other states, which is not accessible by simple models.

5.3.2. Torkance at the true Fermi energy

We start by computing the torkance at the true Fermi energy using Eq. 4.128. We used the constant relaxation time approximation where the vector mean free path is given by $\boldsymbol{\lambda}(\boldsymbol{k}) = (2\Gamma/\hbar)\,\boldsymbol{v}(\boldsymbol{k})$ with $\Gamma = 25\,\text{meV}$ and $\boldsymbol{v}(\boldsymbol{k})$ the group velocity. We find two non-vanishing components of the torkance tensor $t_{zy} = -0.37\,\text{ea}_0$ and $t_{zx} = -0.18\,\text{ea}_0$. The distribution of the torkance in the Brillouin zone is shown in Fig. 5.23. Overall, we find that a very large number of bands contribute to the torkance. By comparison with Fig. 5.22a, we observe states with strong portion of the wave functions on the Ag_2Bi layer that yields a contribution to the torkance of large intensity but of limited surface. This suggests that the Rashba bands hybridize to some extent with the Fe states via the quantum well states of the Ag. However, this does not appear as the main mechanism giving rise to the SOT in that system, since the overall contributions from the other bands (the background torkance) in the Brillouin zone seem to dominate.

The position of the Fermi energy is usually dependent on the thickness of the layers and can also be varied by doping or gating the materials. Therefore, it is relevant to compute the SOT with the Fermi energy shifted into the Rashba bands to observe their effect on the magnetization dynamics. In the following section, we compute the SOT for 930 meV below Fermi energy, where we can capture the effect of the asymmetric Rashba bands.

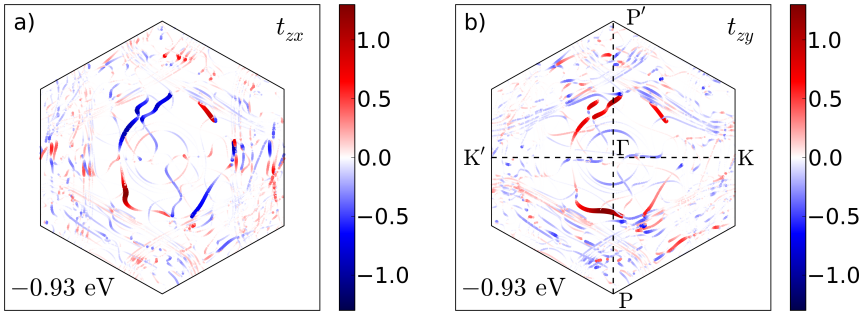

Figure 5.24.: Distribution of (a) $\mathcal{T}_z(\boldsymbol{k})\lambda_x(\boldsymbol{k})/|\boldsymbol{v}(\boldsymbol{k})|$ and (b) $\mathcal{T}_z(\boldsymbol{k})\lambda_y(\boldsymbol{k})/|\boldsymbol{v}(\boldsymbol{k})|$ in the Brillouin zone in units of $\hbar$. The Fermi energy is set 930 meV below its true value.

5.3.3. Torkance at a shifted Fermi energy

We show in Fig. 5.24 the distribution of the torkance in the Brillouin zone 930 meV below Fermi energy. Many bands contribute to the torkance, resulting in two non-vanishing components $t_{zy} = -0.69\,\mathrm{ea_0}$ and $t_{zx} = -0.29\,\mathrm{ea_0}$, which is roughly twice as much as at the true Fermi energy. Compared to the case at the true Fermi energy, there are a few bands with very high intensity, but their surface is now much larger. By comparison with Fig. 5.22b, we observe that these bands are not the Rashba bands, but rather bands that hybridize with the Rashba bands to some extent and are localized at roughly 15% on the Ag_2Bi layer. They yield positive and negative contributions to t_{zx}, which suggests a partial cancellation of different k-points for this component. Their contribution to t_{zy} is only positive so that a net effect of this band is expected for this component. However, the total torkance $t_{zy} = -0.69\,\mathrm{ea_0}$ is negative, which implies that the SOT is in fact dominated by the background torkance, originating from all other bands.

In order to bring deeper insight into the mechanisms giving rise to the torkance, we compare in Fig. 5.25 the layer-resolved torkance, spin flux and spin accumulation. The integrated values of the response coefficients over three different regions of the film are given in Table 5.6. The current-induced spin accumulation at the bottom of the film, i.e., on the Ag_2Bi side, is large and follows the Rashba symmetry $\chi_{xy} >> \chi_{xx}$ (see Eq. 2.8). The magnitude of the spin accumulation in the Fe is strongly reduced as compared to the Ag_2Bi side, due to the competition of the spin-orbit fields with the very strong exchange field in the ferromagnet. There, the response coefficients χ_{xy} and χ_{xx} do not respect the Rashba symmetry anymore, as the two coefficients $\chi_{xy} = 0.6 \times 10^{-8}\mu_\mathrm{B}(\mathrm{V/cm})$ and $\chi_{xx} = 0.3 \times 10^{-8}\mu_\mathrm{B}(\mathrm{V/cm})$ have the same order of magnitude.

Comparing for the Fe region the components of the torkance, $t_{zy} = -0.68\,\mathrm{ea_0}$ and

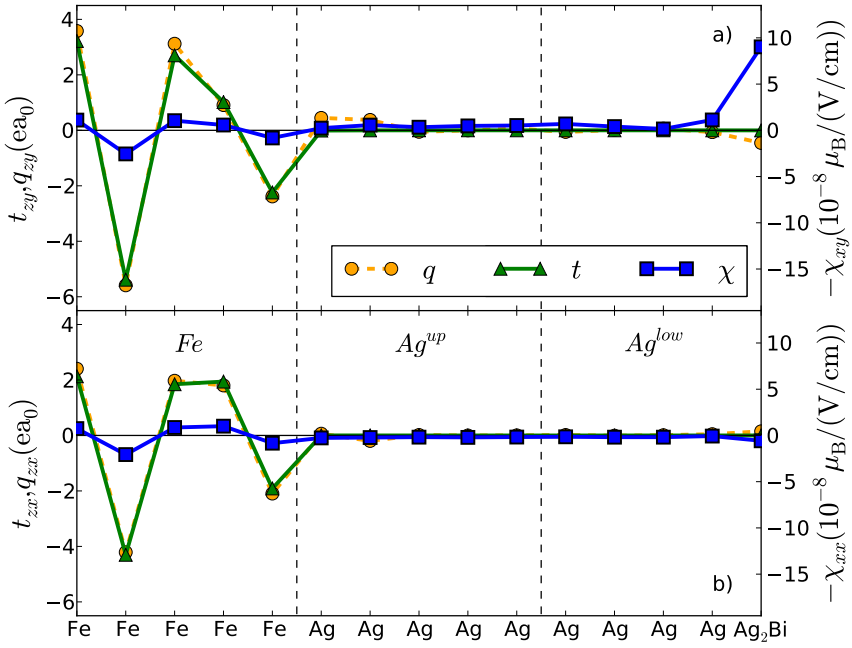

Figure 5.25.: Components of the atom-resolved response tensors for the torque $\boldsymbol{t}$, spin accumulation $\boldsymbol{\chi}$ and spin fluxes $\boldsymbol{q}$ in a Ag_2Bi-terminated Ag film grown on ferromagnetic Fe(110).

	χ_{xy}	χ_{xx}	t_{zy}	t_{zx}	q_{zy}	q_{zx}
Fe	0.6	0.3	−0.68	−0.29	−0.36	−0.13
Ag^{up}	−2.1	1.1	-0.01	0	0.83	−0.11
Ag^{low}	−11.4	1.2	0	0	−0.51	0.21

Table 5.6.: Integrated values of response coefficients for the spin accumulation (units of $10^{-8}\mu_B$(V/cm)), torque and spin fluxes (units of ea_0) over the regions defined in Fig. 5.25.

$t_{zx} = -0.29\,ea_0$, with the components of the spin flux response tensor, $q_{zy} = -0.36\,ea_0$ and $q_{zx} = -0.13\,ea_0$, we find that the spin flux taken from the substrate to the ferromagnet only explains roughly half of the computed SOT. Therefore, half of the SOT originates from the spin-orbit coupling in the ferromagnet itself. We compare now the spin fluxes computed in the different regions of the film to understand what is the origin of the spin currents that contribute to the computed torkance. We see in Table 5.6 that the spin fluxes in the Fe $q_{zy}(Fe) = -0.36\,ea_0$ and at the bottom of the film $q_{zy}(Ag^{\text{low}}) = -0.51\,ea_0$ have the same sign, which suggest that the part of

the torkance due to spin currents do not originate from the Ag_2Bi layer. Instead, the positive spin flux in the upper part the Ag film $q_{zy}(Ag^{\mathrm{up}}) = +0.83\,\mathrm{ea}_0$ suggests that it is the transfer of spin angular momentum from Ag atoms at the interface with Fe that is responsible for the spin current mediated part of the torkance. As for the q_{zx} spin flux components in the different regions, the respective signs suggests that there is a transfer of spin angular momentum from the Ag_2Bi layer to the Fe layer, which contributes to the computed torque. Overall, we conclude that the torque in the considered system originates from all three regions of the film and the use of simple models such as the Rashba model would not alone explain the computed torque.

5.4. SOTs in semiconductor-based thin films: example of Fe/Ge bilayers

In the past most studies of spin-orbit torques have been carried out on systems composed of a ferromagnetic layer deposited on a heavy metal substrate. This choice was motivated by the expectation that the strong spin-orbit coupling in the heavy metal substrate generates large current-induced spin currents injected into the ferromagnet. The large discrepancy between the spin flux flowing into the ferromagnet and the torkance observed in Sections 5.2 and 5.3 suggests that the spin-orbit coupling within the ferromagnet itself can also yield large contributions to the SOT. This provides a very different way of looking at spin-orbit torques in bilayers, where the spin-orbit fields felt by the electrons is an intrinsic property of the ferromagnetic layer and the substrate only acts as a perturbation that breaks inversion symmetry. In this picture the effect of the substrate is not in generating and injecting spin currents into the ferromagnet but rather in perturbing the orbitals of the adjacent ferromagnetic atoms.

In this section we compute the spin-orbit torques in Fe/Ge bilayers in the ferromagnetic and antiferromagnetic phases. Since bulk Ge is a semiconductor, we do not expect the substrate to be the source of large spin currents in that system. Instead, the SOT we are discussing in the following originates from the spin-orbit coupling within the Fe itself, while the effect of Ge is to break inversion symmetry by hybridization of the atoms seating at the interface.

5.4.1. SOTs in ferromagnetic Fe/Ge(111)

We show in Fig. 5.26 a unit cell of a 5-layer Fe film grown on 12 layers of Ge(111). The atomic coordinates are given in Table 5.7 along with the atomic magnetic moments. The electronic structure of the film has been computed using the Jülich KKR code with the VWN functional. We used an angular momentum cutoff of $l_{\max} = 3$ for the Green functions and the wave functions.

We show in Fig. 5.27 the states at the Fermi energy marked by the portion of their wave functions on three different regions of the film (Fe layers, 6 Ge layers closest

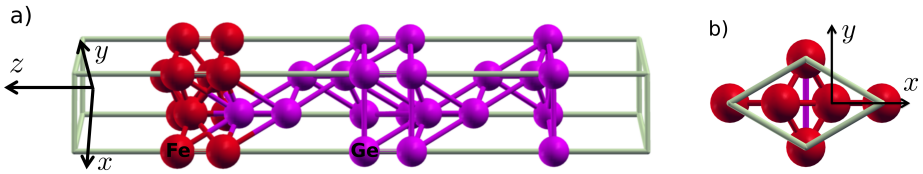

Figure 5.26.: (a) Side and (b) top view of 5 layers of Fe deposited on a Ge(111) film of 12 layers. We show the Fe and Ge atoms in red and violet respectively.

atom	x	y	z	μ_{at}	atom	x	y	z	μ_{at}
Fe	2.2956	0.0000	12.7984	2.79	Ge	0.0000	0.0000	2.4349	0.00
Fe	0.0000	0.0000	12.0515	2.22	Ge	0.0000	0.0000	0.0000	0.00
Fe	-2.2956	0.0000	11.4645	2.32	Ge	-2.2956	0.0000	-0.8116	0.00
Fe	2.2956	0.0000	10.3603	2.20	Ge	-2.2956	0.0000	-3.2465	0.00
Fe	0.0000	0.0000	9.6946	1.97	Ge	2.2956	0.0000	-4.0581	0.00
Ge	-2.2956	0.0000	8.9460	-0.06	Ge	2.2956	0.0000	-6.4930	0.00
Ge	-2.2956	0.0000	6.4885	0.03	Ge	0.0000	0.0000	-7.3046	0.00
Ge	2.2956	0.0000	5.6896	0.01	Ge	0.0000	0.0000	-9.7395	0.00
Ge	2.2956	0.0000	3.4392	0.00					

Table 5.7.: Computational details for the calculation of the electronic structure of the Fe/Ge(111) thin film: x, y and z Cartesian atomic coordinates (in units of Å) and atomic magnetic moments μ_{at} obtained within the Jülich KKR code (in units of μ_{B}). The direct Bravais vectors in Cartesian coordinates are defined by $\boldsymbol{a} = (3.443, -1.988, 0)$ and $\boldsymbol{b} = (3.443, 1.988, 0)$ (in units of Å).

to the interface and 6 Ge layers closest to the bottom of film). One can identify the bulk states of Ge close to the Γ point that spread over the entire Ge substrate, see Fig. 5.27. The surface state located roughly in the middle of the $\Gamma - K$ and $\Gamma - M$ paths is observed at the bottom of the film (Fig. 5.27c) but disappears on the side of the interface with Fe (Fig. 5.27b). All other bands are strongly localized on the Fe layers, as shown in Fig. 5.27a.

We compute the torkance using Eq. 4.128 for three different magnetization directions. We use in a first step the constant relaxation time approximation where the vector mean free path is given by $\boldsymbol{\lambda}(\boldsymbol{k}) = (2\Gamma/\hbar)\,\boldsymbol{v}(\boldsymbol{k})$ with $\Gamma = 25\,\text{meV}$ and $\boldsymbol{v}(\boldsymbol{k})$ the

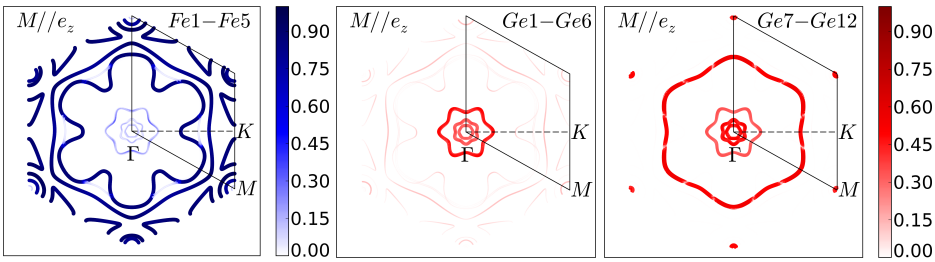

Figure 5.27.: States at the Fermi energy marked by the portion of their wave functions on different regions of the Fe/Ge(111) film: (a) Fe atoms, (b) 6 Ge atoms closest to the interface and (c) 6 Ge atoms at the bottom of the film.

group velocity. The torkance tensors for magnetization along $\hat{\boldsymbol{e}}_x$, $\hat{\boldsymbol{e}}_y$ and $\hat{\boldsymbol{e}}_z$ read

$$\boldsymbol{t}(\boldsymbol{M}//\hat{\boldsymbol{e}}_x) = \begin{bmatrix} 0 & 0 & 0 \\ 0 & 0 & 0 \\ 0.56 & 0 & 0 \end{bmatrix} \tag{5.4}$$

$$\boldsymbol{t}(\boldsymbol{M}//\hat{\boldsymbol{e}}_y) = \begin{bmatrix} 0 & 0 & 0 \\ 0 & 0 & 0 \\ 0 & 0.56 & 0 \end{bmatrix} \tag{5.5}$$

$$\boldsymbol{t}(\boldsymbol{M}//\hat{\boldsymbol{e}}_z) = \begin{bmatrix} -0.56 & 0 & 0 \\ 0 & -0.56 & 0 \\ 0 & 0 & 0 \end{bmatrix}. \tag{5.6}$$

The dependence of the torkance tensor on magnetization direction follows the cross product with the exchange field in the definition of the torque, see Eq. 2.12. This shows that the spin accumulation in that system is insensitive on magnetization direction. Overall, the computed values are of the same order of magnitude as in the case of the FePt/Pt film studied in Section 5.1. This demonstrates that the use of semiconductors instead of heavy metals as a substrate is a promising line of research for the development of SOT-based magnetic memories.

We show in Fig. 5.28 the contribution of different states to the torkance across the Brillouin zone. The bulk states do not appear to play an important role as their intersection with the Fermi energy is relatively small and the intensity of the torkance for these states is moderate. The surface state of Ge at the bottom of the film is hardly visible in Fig. 5.28, due to the spatial separation with the Fe layers. Overall, the torkance has large contributions from the Fe bands, but most of them seem to cancel partially. Only the last band crossing the $\Gamma - K$ path (marked by the letter R in Fig. 5.28) yields contributions of same sign for all k-points, in accordance with the sign of the total torkance tensors in Eqs. 5.4, 5.5 and 5.6. By visual integration of the torkance in Fig. 5.28, it seems to be this band that provides the largest contribution to the torkance.

We now investigate the influence of impurity scattering on the torkance by using Eq. 4.115 to compute the vector mean free path in the presence of Bi impurities. We show in Table 5.8 the torkance values obtained for an impurity concentration equal to 3% and a constant smearing of $\Gamma = 25\,\text{meV}$. We consider the case of Bi adatoms and replacement of Ge or Fe atoms by Bi atoms. We find that the torkance is very sensitive to the presence of Bi impurities inside (substitutional impurity) or on top of (adatom) the Fe layers but is not affected at all by the replacement of Ge atoms. This is in full agreement with Fig. 5.28, where we see that the torkance arises essentially from the Fe states.

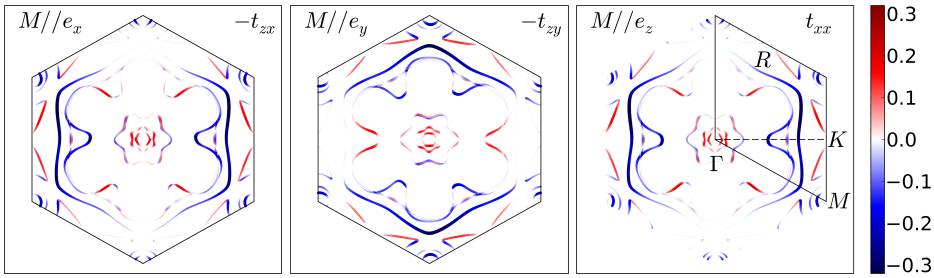

Figure 5.28.: Distribution of $-\mathcal{T}_z(\boldsymbol{k})\lambda_x(\boldsymbol{k})/|\boldsymbol{v}(\boldsymbol{k})|$, $-\mathcal{T}_z(\boldsymbol{k})\lambda_y(\boldsymbol{k})/|\boldsymbol{v}(\boldsymbol{k})|$ and $\mathcal{T}_x(\boldsymbol{k})\lambda_x(\boldsymbol{k})/|\boldsymbol{v}(\boldsymbol{k})|$ in the Brillouin zone in a ferromagnetic Fe/Ge(111) film for three different magnetization directions. Components of the torkance that are not shown vanish for the specified magnetization direction, see Eqs. 5.4, 5.5 and 5.6.

	CRTA	ad	Fe1	Fe2	Fe3	Fe4	Fe5	Ge1	Ge2	Ge3	Ge4
t_{xx}	0.56	0.47	0.47	0.45	0.48	0.44	0.41	0.56	0.56	0.56	0.56

Table 5.8.: Torkance values for a Fe/Ge(111) film in the presence of Bi adatoms (ad) and Bi substitutional impurities in different Fe and Ge layers. The value for the CRTA is given as a reference. The vector mean free path is computed from Eq. 4.115 with a concentration of impurity equal to 3% and $\Gamma = 25\,\text{meV}$.

We conclude that the SOT in Fe/Ge(111) films arise essentially from the spin-orbit coupling within the Fe itself. The effect of the Ge layer is to be understood as a way of breaking the inversion symmetry of the Fe layer by modification of the Fe orbitals at the interface. This stands in sharp contrast to the case of FePt/Pt films (Section 5.1), where the torque arises from a transfer of spin from the Pt to the ferromagnet.

5.4.2. SOTs in ferromagnetic Fe/Ge(001)

In systems with C_3 or C_4 symmetry, the part of the torkance tensor that is odd with respect to magnetization direction reduces to a single independent value $t_{xx} = t_{yy}$. The lack of C_3 or C_4 rotation symmetry axis in Ge(001) films allows for three independent components of the odd torkance t_{xx}, t_{yy} and $t_{xy} = t_{yx}$. We investigate in the following the impact of the stacking direction of Ge on the torkance of Fe/Ge(001) and Fe/Ge(111) films. We restrict our study to the case of out-of-plane magnetization, where the Fe/Ge(111) film exhibits C_3 symmetry but the Fe/Ge(001) film does not. The atomic coordinates are given in Table 5.9 along with the atomic magnetic moments. An illustration of a unit cell of the Fe/Ge(001) film is given in Fig. 5.29.

The torkance tensor computed within the CRTA approximation for the Fe/Ge(001)

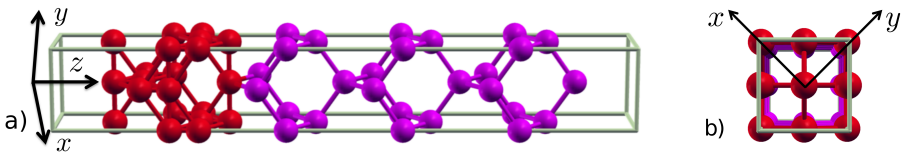

Figure 5.29.: (a) Side and (b) top view of 5 layers of Fe deposited on a Ge(001) film of 12 layers. We show the Fe and Ge atoms in red and violet respectively.

atom	x	y	z	μ_{at}	atom	x	y	z	μ_{at}
Fe	0.000	0.000	-11.312	2.93	Ge	0.000	2.828	-2.828	0.03
Fe	0.000	2.828	-11.312	2.93	Ge	-1.414	1.414	-1.414	0.00
Fe	1.414	1.414	-9.898	2.21	Ge	0.000	0.000	0.000	0.00
Fe	-1.414	1.414	-9.898	2.21	Ge	1.414	1.414	1.414	0.00
Fe	0.000	2.828	-8.484	2.29	Ge	0.000	2.828	2.828	0.00
Fe	0.000	0.000	-8.484	2.28	Ge	-1.414	1.414	4.242	0.00
Fe	-1.414	1.414	-7.070	2.12	Ge	0.000	0.000	5.656	0.00
Fe	1.414	1.414	-7.070	2.17	Ge	1.414	1.414	7.070	0.00
Fe	0.000	0.000	-5.656	2.18	Ge	0.000	2.828	8.484	0.00
Fe	0.000	2.828	-5.656	2.10	Ge	-1.414	1.414	9.898	0.00
Ge	1.414	1.414	-4.242	-0.05	Ge	0.000	0.000	11.312	0.00

Table 5.9.: Computational details for the calculation of the electronic structure of the Fe/Ge(001) thin film: x, y and z Cartesian atomic coordinates (in units of Å) and atomic magnetic moments μ_{at} obtained within the Jülich KKR code (in units of μ_{B}). The direct Bravais vectors in Cartesian coordinates are defined by $\boldsymbol{a} = (2.828, 2.828, 0)$ and $\boldsymbol{b} = (-2.828, 2.828, 0)$ (in units of Å).

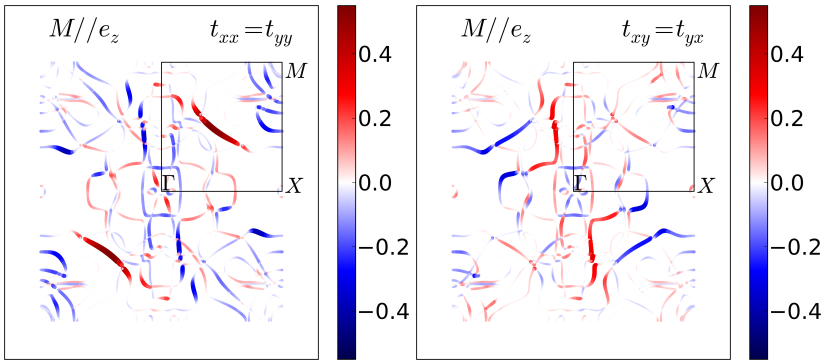

Figure 5.30.: Distribution of $\mathcal{T}_x(\boldsymbol{k})\lambda_x(\boldsymbol{k})/|\boldsymbol{v}(\boldsymbol{k})|$ and $\mathcal{T}_x(\boldsymbol{k})\lambda_y(\boldsymbol{k})/|\boldsymbol{v}(\boldsymbol{k})|$ in the Brillouin zone in a ferromagnetic Fe/Ge(001) film.

film reads[4]

$$\boldsymbol{t}(\boldsymbol{M}//\hat{\boldsymbol{e}}_z) = \begin{bmatrix} -0.15 & 0.08 & 0 \\ 0.08 & -0.15 & 0 \\ 0 & 0 & 0 \end{bmatrix},$$

where the relation $t_{xx} = t_{yy}$ is a consequence of the choice made for the x and y axis. Let us compare the torques induced by an electric field $\boldsymbol{E}^{\mathrm{S}} = E_0(\boldsymbol{e}_x/\sqrt{2} + \boldsymbol{e}_y/\sqrt{2})$ and $\boldsymbol{E}^{\mathrm{L}} = E_0(\boldsymbol{e}_x/\sqrt{2} - \boldsymbol{e}_y/\sqrt{2})$. The definition of the torkance (Eq. 2.2) yields the induced torques $\boldsymbol{T}^{\mathrm{S}} = -0.07\,T_0(\boldsymbol{e}_x/\sqrt{2}+\boldsymbol{e}_y/\sqrt{2})$ and $\boldsymbol{T}^{\mathrm{L}} = -0.23\,T_0(\boldsymbol{e}_x/\sqrt{2}-\boldsymbol{e}_y/\sqrt{2})$, with $T_0 = E_0\,\mathrm{e}a_0$. Therefore, the longitudinal torque induced by an electric field in Fe/Ge(001) varies by a factor of 3 depending on the direction of the electric field and is always much smaller than the torque $-0.56\,T_0$ induced by the same electric field in Fe/Ge(111). This has very strong implications for the experimental investigation of SOTs in Fe/Ge bilayers. In fact, our results suggest an extreme dependence of the SOT on the stacking direction and on the relative alignment of the electric field with the crystallographic axis.

5.4.3. SOTs in antiferromagnetic Fe/Ge(111)

Antiferromagnets have become very popular in the last few years in the spintronics community [72]. They have emerged as a potential replacement for ferromagnets in SOT-based magnetic memories with two main benefits: first, they do not induce stray fields, which are known to limit the scalability of magnetic memories; second, they have a much faster dynamics than ferromagnets. In the following, we apply our KKR formalism to compute the SOT exerted on each sublattice of an antiferromagnetic

[4]In order to construct a Fe film on top of Ge(001), it is necessary to include two Fe atoms per Fe layer and per unit cell. Therefore, there are twice as much Fe atoms per unit cell for Fe/Ge(001) than for Fe/Ge(111). In order to account for that difference, the torkance and torque values for the Fe/Ge(001) film have been divided by two.

atom	x	y	z	μ_{at}	atom	x	y	z	μ_{at}
Fe	0.000	0.000	9.488	2.65	Ge	0.000	2.296	-0.812	0.00
Fe	1.988	3.443	9.488	-2.65	Ge	1.988	5.739	-0.812	0.00
Ge	0.000	2.296	8.783	0.03	Ge	0.000	2.296	-3.247	0.00
Ge	1.988	5.739	8.783	-0.03	Ge	1.988	5.739	-3.247	0.00
Ge	0.000	2.296	6.374	0.00	Ge	0.000	4.591	-4.058	0.00
Ge	1.988	5.739	6.374	0.00	Ge	1.988	1.148	-4.058	0.00
Ge	0.000	4.591	5.584	0.00	Ge	0.000	4.591	-6.493	0.00
Ge	1.988	1.148	5.584	0.00	Ge	1.988	1.148	-6.493	0.00
Ge	0.000	4.591	3.181	0.00	Ge	0.000	0.000	-7.305	0.00
Ge	1.988	1.148	3.181	0.00	Ge	1.988	3.443	-7.305	0.00
Ge	0.000	0.000	2.399	0.00	Ge	0.000	0.000	-9.740	0.00
Ge	1.988	3.443	2.399	0.00	Ge	1.988	3.443	-9.740	0.00
Ge	0.000	0.000	0.000	0.00					
Ge	1.988	3.443	0.000	0.00					

Table 5.10.: Computational details for the calculation of the electronic structure of the antiferromagnetic Fe/Ge(111) thin film: x, y and z Cartesian atomic coordinates (in units of Å) and atomic magnetic moments μ_{at} obtained within the Jülich KKR code (in units of μ_{B}). The direct Bravais vectors in Cartesian coordinates are defined by $\boldsymbol{a} = (3.976, 0, 0)$ and $\boldsymbol{b} = (3.443, 6.886, 0)$ (in units of Å).

Fe monolayer deposited on 12 layers of Ge(111). The atomic coordinates are given in Table 5.10 along with the atomic magnetic moments. According to Ref. [72], the torque we obtain from the Boltzmann formalism does not have the desirable symmetry to switch antiferromagnets, as it is an odd function of the magnetization direction. However, it is relevant to consider the SOT acting on each sublattice as it gives a good indication of the strength of the spin-orbit fields.

The torkance tensors for sublattices A and B computed within the CRTA approximation read

$$\boldsymbol{t}^{\mathrm{A}} = \begin{bmatrix} -0.22 & 0 & 0 \\ 0 & -0.17 & 0 \\ 0 & 0 & 0 \end{bmatrix} \tag{5.7}$$

$$\boldsymbol{t}^{\mathrm{B}} = \begin{bmatrix} 0.22 & 0 & 0 \\ 0 & 0.17 & 0 \\ 0 & 0 & 0 \end{bmatrix} . \tag{5.8}$$

The symmetry of the torkance tensor is drastically modified by the antiferromagnetic order. As in the case of the ferromagnetic Fe/Ge(001) film, there is no C_3 symmetry that enforces $t_{xx} = t_{yy}$ anymore. Indeed, we find a large anisotropy of the longitudinal torkance, which varies by 30% depending on the direction of the electric field. The magnitude of the computed SOT is 2 or 3 times smaller than in ferromagnetic Fe/Ge(111) (Section 5.4.1) but as large as in ferromagnetic Fe/Ge(001) (Section 5.4.2).

The torques exerted on the two sublattices have equal magnitudes and opposite signs. We show in Fig. 5.31 the distribution of the torkance across the Brillouin zone for each sublattice. Comparing the t^A_{xx} and t^B_{xx} components, we find that each state contributes to the torkance with different signs on each sublattice. The same observation can be made for the t^A_{yy} and t^B_{yy} components. Because also the magnitudes of the torkance differs between the two sublattices, we find that most of the states yield a finite contribution to the torkance. However, the total torkance obtained by integration of the state-resolved torkance vanishes, as shown by the opposite signs of $\boldsymbol{t}^{\mathrm{A}}$ and $\boldsymbol{t}^{\mathrm{B}}$, see Eqs. 5.7 and 5.8.

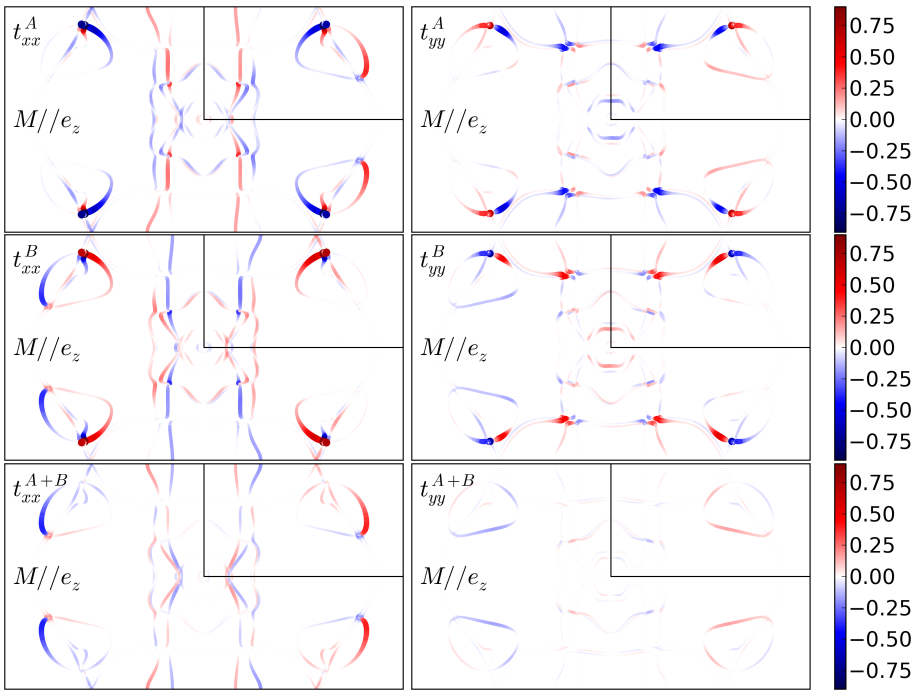

Figure 5.31.: Distribution of $\mathcal{T}_x(\boldsymbol{k})\lambda_x(\boldsymbol{k})/|\boldsymbol{v}(\boldsymbol{k})|$ and $\mathcal{T}_y(\boldsymbol{k})\lambda_y(\boldsymbol{k})/|\boldsymbol{v}(\boldsymbol{k})|$ in the Brillouin zone for each sublattice of an antiferromagnetic Fe/Ge(111) film.

To summarize, we find in antiferromagnetic Fe/Ge bilayers a SOT acting on individual sublattices of similar order of magnitude as in ferromagnetic Fe/Ge bilayers. Our results suggest that semiconductor-based heterostructures such as Fe/Ge bilayers might also be promising candidates for the development of antiferromagnetic memory devices.

6 Conclusion

In summary, the first principles methods developed in this work provide an accurate and efficient way of computing intrinsic and extrinsic spin-orbit torques in ferromagnetic systems.

The main accomplishment of this thesis is the implementation in the Jülich KKR code of a formalism for the extrinsic spin-orbit torques. The impurity-induced transition rates are computed from first principles and its influence on transport properties is treated within the Boltzmann formalism. The formalism provides a way to compute spin-orbit torques in complex ferromagnetic heterostructures beyond the conventional constant relaxation time approximation.

Taking FePt/Pt and Co/Cu thin films as examples, a pronounced dependence of the SOT on the specific types of scattering has been demonstrated. In the case of FePt/Pt bilayers, the presence of disorder at surfaces and interfaces crucially modifies the net torque acting on the magnetization. If the distribution of defects are such that they preferentially suppress the surface contributions to the torque, a significant and unexpected increase of the net torque was observed. In the case of Co/Cu bilayers, the doping with various types of impurities was found to be a powerful mean for engineering the torque in such systems. Astonishingly, a sign change of the torque can be achieved when Co/Cu thin films are doped with Ir impurities.

Motivated by recent experimental results, the developed formalism has been applied to the investigation of spin-orbit torques in a Ag_2Bi-terminated Ag film grown on ferromagnetic Fe(110). The analysis of the spin fluxes and the Fermi surface decomposition of the torkance tensor coefficients clearly rules out that the torque exerted on the Fe originates solely from the spin-orbit coupling in the Ag_2Bi layer. Instead, the total torque exerted on the magnetization appears to have three different components, arising from the spin-orbit coupling in the Fe itself, at the Fe/Ag interface and at the Ag_2Bi surface.

The large spin-orbit torque predicted in Fe/Ge bilayers within this work suggests that semiconductor substrates might be a promising alternative to heavy metals for electrically switchable magnetic devices. The drastic influence of the stacking direc-

tion and the large anisotropy predicted by our formalism provides important guidelines for future experiments. We also computed the spin-orbit torques acting on each sublattice of an antiferromagnetic Fe/Ge bilayer and found a large anisotropy of the sublattice-resolved torkance tensor.

As a part of this work, also the spin-orbit torques induced by thermal gradients have been investigated. We found that the corresponding response coefficients are large enough for the phenomena to be observed experimentally.

A Perspectives: Kubo formalism for the torque in KKR

We have presented in Section 4 a KKR formalism to investigate the impurity-driven spin-orbit torques within the semi-classical theory of transport. A possible extension of our work is to go beyond the Boltzmann response by using the Kubo formalism for the torque [19], which was used in Section 3 within the FLAPW method. One of the advantage of the KKR method is its ability to treat impurity scattering in a rigorous manner. Therefore, an implementation of the Kubo formula in the KKR code would pave the way for a linear response theory that goes beyond the constant relaxation time approximation used in Section 3. Even though this development goes beyond the scope of this thesis, we discuss in this appendix a possible way to achieve it.

The Kubo formula for the torkance reads

$$\begin{aligned}
\mathrm{t}_{ij}^{\mathrm{I(a)}} &= \frac{e}{hN} \ \mathrm{Tr}\langle \mathcal{T}_i G^{\mathrm{R}}(\varepsilon_F) v_j G^{\mathrm{A}}(\varepsilon_F)\rangle, \\
\mathrm{t}_{ij}^{\mathrm{I(b)}} &= -\frac{e}{hN} \Re\mathrm{Tr}\langle \mathcal{T}_i G^{\mathrm{R}}(\varepsilon_F) v_j G^{\mathrm{R}}(\varepsilon_F)\rangle, \\
\mathrm{t}_{ij}^{\mathrm{II}} &= \frac{e}{hN} \int_{-\infty}^{\varepsilon_F} d\varepsilon \ \Re\mathrm{Tr}\langle \mathcal{T}_i G^{\mathrm{R}}(\varepsilon) v_j \frac{dG^{\mathrm{R}}(\varepsilon)}{d\varepsilon} - \mathcal{T}_i \frac{dG^{\mathrm{R}}(\varepsilon)}{d\varepsilon} v_j G^{\mathrm{R}}(\varepsilon)\rangle,
\end{aligned} \tag{A.1}$$

where we have introduced the number of unit cells N to normalize the torque to a single unit cell.

It is essential to evaluate Eq. A.1 to have a practical implementation of the velocity operator $\boldsymbol{v}$ in the KKR formalism. A possible implementation is to use the α-matrix as discussed in Section 4.3.4.

The retarded Green function in KKR is given by Eq. 4.37. This expression can be generalized to the case of multiple atoms in the unit cell by

$$\begin{aligned}
G^{\mathrm{R}}(\boldsymbol{r} + \boldsymbol{R}_\mu + \boldsymbol{R}_n, \boldsymbol{r'} + \boldsymbol{R}_{\mu'} + \boldsymbol{R}_{n'}, \varepsilon) = \delta_{nn'}\delta_{\mu\mu'} \overset{o}{G}{}^{\mathrm{R}}_{\mu}(\boldsymbol{r}, \boldsymbol{r'}, \varepsilon) \\
+ \sum_{\Lambda\Lambda'} R^{\mu}_{\Lambda}(\boldsymbol{r}, \varepsilon) G^{\mathrm{R},nn'}_{\Lambda\Lambda',\mu\mu'}(\varepsilon) \bar{R}^{\mu'}_{\Lambda'}(\boldsymbol{r'}, \varepsilon).
\end{aligned} \tag{A.2}$$

The advanced Green function G^{A} is connected to the retarded Green function G^{R} by the relation

$$G^{\mathrm{A}}(\boldsymbol{r'}+\boldsymbol{R}_{\mu'}+\boldsymbol{R}_{n'},\boldsymbol{r}+\boldsymbol{R}_{\mu}+\boldsymbol{R}_{n}) = [G^{\mathrm{R}}(\boldsymbol{r}+\boldsymbol{R}_{\mu}+\boldsymbol{R}_{n},\boldsymbol{r'}+\boldsymbol{R}_{\mu'}+\boldsymbol{R}_{n'})]^{\dagger}. \quad \text{(A.3)}$$

It is convenient to expand the advanced Green function according to

$$\begin{aligned} G^{\mathrm{A}}(\boldsymbol{r'}+\boldsymbol{R}_{\mu'}+\boldsymbol{R}_{n'},\boldsymbol{r}+\boldsymbol{R}_{\mu}+\boldsymbol{R}_{n},\varepsilon) &= \delta_{nn'}\delta_{\mu\mu'}\overset{o}{G}{}^{\mathrm{A}}_{\mu}(\boldsymbol{r'},\boldsymbol{r},\varepsilon) \\ &\quad + \sum_{\Lambda\Lambda'}[\bar{R}^{\mu'}_{\Lambda'}(\boldsymbol{r'})]^{\dagger}(G^{\mathrm{A},n'n}_{\Lambda'\Lambda,\mu'\mu})[R^{\mu}_{\Lambda}(\boldsymbol{r})]^{\dagger}, \end{aligned} \quad \text{(A.4)}$$

because Eq. A.3 gives a direct relation between the retarded and advanced structural Green functions:

$$\begin{aligned} [\bar{R}^{\mu'}_{\Lambda'}(\boldsymbol{r'})]^{\dagger}G^{\mathrm{A},n'n}_{\Lambda'\Lambda,\mu'\mu}[R^{\mu}_{\Lambda}(\boldsymbol{r})]^{\dagger} &= \left[R^{\mu}_{\Lambda}(\boldsymbol{r},\varepsilon)G^{\mathrm{R},nn'}_{\Lambda\Lambda',\mu\mu'}(\varepsilon)\bar{R}^{\mu'}_{\Lambda'}(\boldsymbol{r'},\varepsilon)\right]^{\dagger} \\ &= [\bar{R}^{\mu'}_{\Lambda'}(\boldsymbol{r'},\varepsilon)]^{\dagger}(G^{\mathrm{R},nn'}_{\Lambda\Lambda',\mu\mu'}(\varepsilon))^{*}[R^{\mu}_{\Lambda}(\boldsymbol{r},\varepsilon)]^{\dagger}, \end{aligned} \quad \text{(A.5)}$$

where $G^{\mathrm{A},n'n}_{\Lambda'\Lambda,\mu'\mu} = (G^{\mathrm{R},nn'}_{\Lambda\Lambda',\mu\mu'}(\varepsilon))^{*}$ can be directly identified as the conjugate transpose of the retarded Green function.

Inserting Eq. A.2 into Eq. A.1 yields for the $t^{\mathrm{I(b)}}$ component of the torkance tensor

$$\begin{aligned} t^{\mathrm{I(b)}}_{ij} = &-\frac{e}{hN}\sum_{n\mu}\int_{V_{\mu}}d\boldsymbol{r}\int_{V_{\mu}}d\boldsymbol{r'}\ \Re\mathrm{Tr}\langle\mathcal{T}_{i\mu}(\boldsymbol{r})\overset{o}{G}{}^{\mathrm{R}}{}_{\mu}(\boldsymbol{r},\boldsymbol{r'})v_j\overset{o}{G}{}^{\mathrm{R}}{}_{\mu}(\boldsymbol{r'},\boldsymbol{r})\rangle \\ &-\frac{e}{hN}\sum_{nn'}\sum_{\mu\mu'}\sum_{\Lambda\Lambda'\Lambda''\Lambda'''}\int_{V_{\mu}}d\boldsymbol{r}\int_{V_{\mu'}}d\boldsymbol{r'} \\ &\Re\mathrm{Tr}\langle\mathcal{T}_{i\mu}(\boldsymbol{r})R^{\mu}_{\Lambda}(\boldsymbol{r})G^{\mathrm{R},nn'}_{\Lambda\Lambda',\mu\mu'}\bar{R}^{\mu'}_{\Lambda'}(\boldsymbol{r'})v_jR^{\mu'}_{\Lambda''}(\boldsymbol{r'})G^{\mathrm{R},n'n}_{\Lambda''\Lambda''',\mu'\mu}\bar{R}^{\mu}_{\Lambda'''}(\boldsymbol{r})\rangle \end{aligned} \quad \text{(A.6)}$$

The first and second terms in the previous equation can be identified respectively as on-site and off-site terms. The on-site term involves only the single site Green function and can be computed independently for each atomic potential. The off-site term corresponds to the multiple scattering part that implies the structural Green function.

We first discuss the off-site term of the $t^{\mathrm{I(b)}}$ component of the torkance tensor. The invariance of the trace by cyclic permutation in Eq. A.6 allows us to move $\bar{R}^{\mu}_{\Lambda'''}(\boldsymbol{r})$ to the front of the trace, which yields

$$\begin{aligned} \mathrm{t}^{\mathrm{I(b),off}}_{ij} = &-\frac{e}{hN}\sum_{nn'}\sum_{\mu\mu'}\sum_{\Lambda\Lambda'}\sum_{\Lambda''\Lambda'''}\int_{V_{\mu}}d\boldsymbol{r}\int_{V_{\mu'}}d\boldsymbol{r'} \\ &\Re\mathrm{Tr}\langle\bar{R}^{\mu}_{\Lambda'''}(\boldsymbol{r})\mathcal{T}_{i\mu}(\boldsymbol{r})R^{\mu}_{\Lambda}(\boldsymbol{r})G^{\mathrm{R},nn'}_{\Lambda\Lambda',\mu\mu'}\bar{R}^{\mu'}_{\Lambda'}(\boldsymbol{r'})v_jR^{\mu'}_{\Lambda''}(\boldsymbol{r'})G^{\mathrm{R},n'n}_{\Lambda''\Lambda''',\mu'\mu}\rangle. \end{aligned} \quad \text{(A.7)}$$

We introduce the matrices $\widetilde{\mathfrak{T}}_i^{\mathrm{I(b)}}$ and $\widetilde{v}_j^{\mathrm{I(b)}}$ whose elements are defined by

$$\widetilde{\mathfrak{T}}^{\mu,\mathrm{I(b)}}_{\Lambda\Lambda',i} = \int_{V_\mu} d\boldsymbol{r}\ \bar{R}^\mu_\Lambda(\boldsymbol{r})\mathcal{T}_{i\mu}(\boldsymbol{r})R^\mu_{\Lambda'}(\boldsymbol{r}), \tag{A.8}$$

$$\widetilde{v}^{\mu,\mathrm{I(b)}}_{\Lambda\Lambda',j} = \int_{V_\mu} d\boldsymbol{r}\ \bar{R}^\mu_\Lambda(\boldsymbol{r})v_{j\mu}R^\mu_{\Lambda'}(\boldsymbol{r}). \tag{A.9}$$

This allows us to rewrite Eq. (A.7) in the much more concise way

$$\mathrm{t}^{\mathrm{I(b),off}}_{ij} = -\frac{e}{hN}\sum_{nn'} \Re\mathrm{Tr}\langle\widetilde{\mathfrak{T}}_i^{\mathrm{I(b)}}G^{\mathrm{R}}_{nn'}\widetilde{v}_j^{\mathrm{I(b)}}G^{\mathrm{R}}_{n'n}\rangle. \tag{A.10}$$

In order to overcome the summation over the many unit cells, we introduce the Fourier transform of the Green functions $G^R(\boldsymbol{k})$, so that

$$G^{\mathrm{R}}_{nn'} = \frac{1}{\mathcal{S}_{\mathrm{BZ}}}\int_{\mathrm{BZ}} d\boldsymbol{k}\ G^{\mathrm{R}}(\boldsymbol{k})e^{-i\boldsymbol{k}\cdot(\boldsymbol{R}_n-\boldsymbol{R}_{n'})}. \tag{A.11}$$

Using the relation $(\sum_n e^{-i(\boldsymbol{k}-\boldsymbol{k'})\cdot\boldsymbol{R}_n})(\sum_{n'} e^{-i(\boldsymbol{k}-\boldsymbol{k'})\cdot\boldsymbol{R}_{n'}}) = \delta(\boldsymbol{k}-\boldsymbol{k'})N$ leads to the final expression

$$\mathrm{t}^{\mathrm{I(b),off}}_{ij} = -\frac{e}{h\mathcal{S}^2_{\mathrm{BZ}}}\int_{\mathrm{BZ}} d\boldsymbol{k}\ \Re\mathrm{Tr}\langle\widetilde{\mathfrak{T}}_i^{\mathrm{I(b)}}G^{\mathrm{R}}(\boldsymbol{k})\widetilde{v}_j^{\mathrm{I(b)}}G^{\mathrm{R}}(\boldsymbol{k})\rangle. \tag{A.12}$$

Using the expansion of the advanced Green function given by Eq. A.4, we obtain the off-site term of the $t^{\mathrm{I(a)}}$ torkance tensor

$$\mathrm{t}^{\mathrm{I(a),off}}_{ij} = \frac{eN}{h\mathcal{S}^2_{\mathrm{BZ}}}\int_{\mathrm{BZ}} d\boldsymbol{k}\ \mathrm{Tr}\langle\widetilde{\mathfrak{T}}_i^{\mathrm{I(a)}}G^{\mathrm{R}}(\boldsymbol{k})\widetilde{v}_j^{\mathrm{I(a)}}G^{\mathrm{A}}(\boldsymbol{k})\rangle, \tag{A.13}$$

where the matrix elements of $\widetilde{\mathfrak{T}}_i^{\mathrm{I(a)}}$ and $\widetilde{v}_j^{\mathrm{I(a)}}$ are given by

$$\widetilde{\mathfrak{T}}^{\mu,\mathrm{I(a)}}_{\Lambda\Lambda',i} = \int_{V_\mu} d\boldsymbol{r}\ [R^\mu_\Lambda(\boldsymbol{r})]^\dagger\mathcal{T}_{i\mu}(\boldsymbol{r})R^\mu_{\Lambda'}(\boldsymbol{r}), \tag{A.14}$$

$$\widetilde{v}^{\mu,\mathrm{I(a)}}_{\Lambda\Lambda',j} = \int_{V_\mu} d\boldsymbol{r}\ \bar{R}^\mu_\Lambda(\boldsymbol{r})v_{j\mu}[\bar{R}^\mu_{\Lambda'}(\boldsymbol{r})]^\dagger. \tag{A.15}$$

Because the off-site terms of the Kubo formula are the ones that carry the effect of the spin currents, they should be sufficient to compute the torque that arises from the spin Hall effect. One advantage of a KKR implementation of the Kubo formula over a FLAPW implementation is that there is no conceptual difficulty to include the effect of impurity scattering on the transport properties. This can be done by defining a disordered Green function $G^{\mathrm{R/A}}_{\mathrm{dis}}$ connected to the clean Green function $G^{\mathrm{R/A}}$ by a Dyson equation:

$$G^{\mathrm{R/A}}_{\mathrm{dis}} = G^{\mathrm{R/A}} + G^{\mathrm{R/A}}\ \Sigma\ G^{\mathrm{R/A}}_{\mathrm{dis}}, \tag{A.16}$$

where the self-energy Σ can be connected to the impurity-induced transition rates $P_{\boldsymbol{kk'}}$ (Eq. 4.66) in the dilute limit. This would probably include the effect of impurity skew-scattering on the spin-orbit torque in a satisfying manner.

Bibliography

[1] W. Zhao, Y. Zhang, T. Devolder, J. Klein, D. Ravelosona, C. Chappert, and P. Mazoyer, "Failure and reliability analysis of STT-MRAM", Microelectronics Reliability **52**, 1848 –1852 (2012).

[2] G. Prenat, K. Jabeur, P. Vanhauwaert, G. D. Pendina, F. Oboril, R. Bishnoi, M. Ebrahimi, N. Lamard, O. Boulle, K. Garello, J. Langer, B. Ocker, M. C. Cyrille, P. Gambardella, M. Tahoori, and G. Gaudin, "Ultra-Fast and High-Reliability SOT-MRAM: From Cache Replacement to Normally-Off Computing", IEEE Transactions on Multi-Scale Computing Systems **2**, 49–60 (2016).

[3] A. Chernyshov, M. Overby, X. Liu, J. K. Furdyna, Y. Lyanda-Geller, and L. P. Rokhinson, "Evidence for reversible control of magnetization in a ferromagnetic material by means of spin-orbit magnetic field", Nature Phys. **5**, 656 –659 (2009).

[4] I. M. Miron, T. Moore, H. Szambolics, L. D. Buda-Prejbeanu, S. Auffret, B. Rodmacq, S. Pizzini, J. Vogel, M. Bonfim, A. Schuhl, and G. Gaudin, "Fast current-induced domain-wall motion controlled by the Rashba effect", Nature Mater. **10**, 419 –423 (2011).

[5] I. Mihai Miron, G. Gaudin, S. Auffret, B. Rodmacq, A. Schuhl, S. Pizzini, J. Vogel, and P. Gambardella, "Current-driven spin torque induced by the Rashba effect in a ferromagnetic metal layer", Nature Mater. **9**, 230–234 (2010).

[6] A. Manchon and S. Zhang, "Theory of spin torque due to spin-orbit coupling", Phys. Rev. B **79**, 094422 (2009).

[7] I. Garate and A. H. MacDonald, "Influence of a transport current on magnetic anisotropy in gyrotropic ferromagnets", Phys. Rev. B **80**, 134403 (2009).

[8] I. M. Miron, K. Garello, G. Gaudin, P.-J. Zermatten, M. V. Costache, S. Auffret, S. Bandiera, B. Rodmacq, A. Schuhl, and P. Gambardella, "Perpendicular switching of a single ferromagnetic layer induced by in-plane current injection", Nature **476**, 189 –193 (2011).

[9] L. Liu, C.-F. Pai, Y. Li, H. W. Tseng, D. C. Ralph, and R. A. Buhrman, "Spin-Torque Switching with the Giant Spin Hall Effect of Tantalum", Science **336**, 555–558 (2012).

[10] L. Liu, O. J. Lee, T. J. Gudmundsen, D. C. Ralph, and R. A. Buhrman, "Current-Induced Switching of Perpendicularly Magnetized Magnetic Layers Using Spin Torque from the Spin Hall Effect", Phys. Rev. Lett. **109**, 096602 (2012).

[11] Y. K. Kato, R. C. Myers, A. C. Gossard, and D. D. Awschalom, "Observation of the Spin Hall Effect in Semiconductors", Science **306**, 1910–1913 (2004).

[12] J. Sinova, S. O. Valenzuela, J. Wunderlich, C. H. Back, and T. Jungwirth, "Spin Hall effects", Rev. Mod. Phys. **87**, 1213–1260 (2015).

[13] P. M. Haney, H.-W. Lee, K.-J. Lee, A. Manchon, and M. D. Stiles, "Current induced torques and interfacial spin-orbit coupling: Semiclassical modeling", Phys. Rev. B **87**, 174411 (2013).

[14] V. Edelstein, "Spin polarization of conduction electrons induced by electric current in two-dimensional asymmetric electron systems", Solid State Communications **73**, 233–235 (1990).

[15] K.-W. Kim, S.-M. Seo, J. Ryu, K.-J. Lee, and H.-W. Lee, "Magnetization dynamics induced by in-plane currents in ultrathin magnetic nanostructures with Rashba spin-orbit coupling", Phys. Rev. B **85**, 180404 (2012).

[16] L. Berger, "Emission of spin waves by a magnetic multilayer traversed by a current", Phys. Rev. B **54**, 9353–9358 (1996).

[17] J. Slonczewski, "Current-driven excitation of magnetic multilayers", J. Magn. Magn. Mater. **159**, L1 –L7 (1996).

[18] T. L. Gilbert, "A phenomenological theory of damping in ferromagnetic materials", IEEE Transactions on Magnetics **40**, 3443–3449 (2004).

[19] F. Freimuth, S. Blügel, and Y. Mokrousov, "Spin-orbit torques in Co/Pt(111) and Mn/W(001) magnetic bilayers from first principles", Phys. Rev. B **90**, 174423 (2014).

[20] A. Manchon and S. Zhang, "Theory of nonequilibrium intrinsic spin torque in a single nanomagnet", Phys. Rev. B **78**, 212405 (2008).

[21] T. Tanaka, H. Kontani, M. Naito, T. Naito, D. S. Hirashima, K. Yamada, and J. Inoue, "Intrinsic spin Hall effect and orbital Hall effect in $4d$ and $5d$ transition metals", Phys. Rev. B **77**, 165117 (2008).

[22] D. Xiao, Y. Yao, Z. Fang, and Q. Niu, "Berry-Phase Effect in Anomalous Thermoelectric Transport", Phys. Rev. Lett. **97**, 026603 (2006).

[23] F. Freimuth, S. Blügel, and Y. Mokrousov, "Berry phase theory of Dzyaloshinskii–Moriya interaction and spin–orbit torques", J. Phys.: Cond. Matter **26**, 104202 (2014).

[24] J. Weischenberg, F. Freimuth, S. Blügel, and Y. Mokrousov, "Scattering-independent anomalous Nernst effect in ferromagnets", Phys. Rev. B **87**, 060406 (2013).

[25] S.-g. Cheng, Y. Xing, Q.-f. Sun, and X. C. Xie, "Spin Nernst effect and Nernst effect in two-dimensional electron systems", Phys. Rev. B **78**, 045302 (2008).

[26] X. Liu and X. Xie, Solid State Communications **150**, 471 (2010).

[27] K. Tauber, M. Gradhand, D. Fedorov, and I. Mertig, Phys. Rev. Lett. **109**, 026601 (2012).

[28] S. Wimmer, D. Ködderitzsch, K. Chadova, and H. Ebert, Phys. Rev. B **88**, 201108(R) (2013).

[29] M. P. Marder, *Condensed Matter Physics* (Wiley, New York, 2000).

[30] W. Kohn and L. J. Sham, "Self-Consistent Equations Including Exchange and Correlation Effects", Phys. Rev. **140**, A1133–A1138 (1965).

[31] S. H. Vosko, L. Wilk, and M. Nusair, "Accurate spin-dependent electron liquid correlation energies for local spin density calculations: a critical analysis", Canadian Journal of Physics **58**, 1200–1211 (1980).

[32] J. P. Perdew, K. Burke, and M. Ernzerhof, "Generalized Gradient Approximation Made Simple", Phys. Rev. Lett. **77**, 3865–3868 (1996).

[33] J. C. Slater, "Wave Functions in a Periodic Potential", Phys. Rev. **51**, 846–851 (1937).

[34] P. Kurz, "Non-collinear magnetism at surfaces and in ultrathin films", PhD thesis (RWTH Aachen, 2000).

[35] N. Marzari and D. Vanderbilt, "Maximally localized generalized Wannier functions for composite energy bands", Phys. Rev. B **56**, 12847–12865 (1997).

[36] A. A. Mostofi, J. R. Yates, Y.-S. Lee, I. Souza, D. Vanderbilt, and N. Marzari, "wannier90: A tool for obtaining maximally-localised Wannier functions", Computer Physics Communications **178**, 685 –699 (2008).

[37] I. Souza, N. Marzari, and D. Vanderbilt, "Maximally localized Wannier functions for entangled energy bands", Phys. Rev. B **65**, 035109 (2001).

[38] F. Freimuth, Y. Mokrousov, D. Wortmann, S. Heinze, and S. Blügel, "Maximally localized Wannier functions within the FLAPW formalism", Phys. Rev. B **78**, 035120 (2008).

[39] P. M. Haney, H.-W. Lee, K.-J. Lee, A. Manchon, and M. D. Stiles, "Current-induced torques and interfacial spin-orbit coupling", Phys. Rev. B **88**, 214417 (2013).

[40] F. Freimuth, S. Blügel, and Y. Mokrousov, "Direct and inverse spin-orbit torques", Phys. Rev. B **92**, 064415 (2015).

[41] G. Géranton, F. Freimuth, S. Blügel, and Y. Mokrousov, "Spin-orbit torques in $L1_0 - \mathrm{FePt/Pt}$ thin films driven by electrical and thermal currents", Phys. Rev. B **91**, 014417 (2015).

[42] S. Lowitzer, D. Ködderitzsch, and H. Ebert, "Coherent Description of the Intrinsic and Extrinsic Anomalous Hall Effect in Disordered Alloys on an *Ab Initio* Level", Phys. Rev. Lett. **105**, 266604 (2010).

[43] Y. Niimi, M. Morota, D. H. Wei, C. Deranlot, M. Basletic, A. Hamzic, A. Fert, and Y. Otani, "Extrinsic Spin Hall Effect Induced by Iridium Impurities in Copper", Phys. Rev. Lett. **106**, 126601 (2011).

[44] Y. Niimi, Y. Kawanishi, D. H. Wei, C. Deranlot, H. X. Yang, M. Chshiev, T. Valet, A. Fert, and Y. Otani, "Giant Spin Hall Effect Induced by Skew Scattering from Bismuth Impurities inside Thin Film CuBi Alloys", Phys. Rev. Lett. **109**, 156602 (2012).

[45] M. Gradhand, D. V. Fedorov, P. Zahn, and I. Mertig, "Extrinsic Spin Hall Effect from First Principles", Phys. Rev. Lett. **104**, 186403 (2010).

[46] M. Gradhand, D. V. Fedorov, P. Zahn, and I. Mertig, "Spin Hall angle versus spin diffusion length: Tailored by impurities", Phys. Rev. B **81**, 245109 (2010).

[47] S. Lowitzer, M. Gradhand, D. Ködderitzsch, D. V. Fedorov, I. Mertig, and H. Ebert, "Extrinsic and Intrinsic Contributions to the Spin Hall Effect of Alloys", Phys. Rev. Lett. **106**, 056601 (2011).

[48] D. Ködderitzsch, K. Chadova, and H. Ebert, "Linear response Kubo-Bastin formalism with application to the anomalous and spin Hall effects: A first-principles approach", Phys. Rev. B **92**, 184415 (2015).

[49] K. Garello, I. M. Miron, C. O. Avci, F. Freimuth, Y. Mokrousov, S. Blügel, S. Auffret, O. Boulle, G. Gaudin, and P. Gambardella, "Symmetry and magnitude of spin-orbit torques in ferromagnetic heterostructures", Nature Nanotech. **8**, 587 (2013).

[50] C. O. Avci, K. Garello, C. Nistor, S. Godey, B. Ballesteros, A. Mugarza, A. Barla, M. Valvidares, E. Pellegrin, A. Ghosh, I. M. Miron, O. Boulle, S. Auffret, G. Gaudin, and P. Gambardella, "Fieldlike and antidamping spin-orbit torques in as-grown and annealed Ta/CoFeB/MgO layers", Phys. Rev. B **89**, 214419 (2014).

[51] G. Géranton, B. Zimmermann, N. H. Long, P. Mavropoulos, S. Blügel, F. Freimuth, and Y. Mokrousov, "Spin-orbit torques and spin accumulation in FePt/Pt and Co/Cu thin films from first principles: The role of impurities", Phys. Rev. B **93**, 224420 (2016).

[52] J. Korringa, Physica **13**, 392 (1947).

[53] W. Kohn and N. Rostoker, "Solution of the Schrödinger Equation in Periodic Lattices with an Application to Metallic Lithium", Phys. Rev. **94**, 1111–1120 (1954).

[54] T. H. Dupree, Ann. Phys. (N. Y.) **15**, 63 (1961).

[55] F. S. Ham and B. Segall, "Energy Bands in Periodic Lattices¯Green's Function Method", Phys. Rev. **124**, 1786–1796 (1961).

[56] G. J. Morgan, "Bloch waves and scattering by impurities", Proceedings of the Physical Society **89**, 365 (1966).

[57] J. L. Beeby, Proc. Roy. Soc. London **Ser. A302**, 113 (1967).

[58] B. Drittler, "KKR-Greensche Funktionsmethode für das volle Zellpotential", PhD thesis (Forschungszentrum Jülich, 1991).

[59] D. S. G. Bauer, "Development of a relativistic full-potential first-principles multiple scattering Green function method applied to complex magnetic textures of nano structures at surfaces", PhD thesis (RWTH Aachen, 2013).

[60] R Zeller, "Multiple-scattering solution of Schrodinger's equation for potentials of general shape", Journal of Physics C: Solid State Physics **20**, 2347 (1987).

[61] K. Tauber, D. V. Fedorov, M. Gradhand, and I. Mertig, "Spin Hall and spin Nernst effect in dilute ternary alloys", Phys. Rev. B **87**, 161114 (2013).

[62] S. Heers, "Effect of spin-orbit scattering on transport properties of low-dimensional dilute alloys", PhD thesis (RWTH Aachen, 2011).

[63] B. Zimmermann, P. Mavropoulos, N. H. Long, C.-R. Gerhorst, S. Blügel, and Y. Mokrousov, "Fermi surfaces, spin-mixing parameter, and colossal anisotropy of spin relaxation in transition metals from *ab initio* theory", Phys. Rev. B **93**, 144403 (2016).

[64] R. V. Chepulskii and W. H. Butler, "Ab initio magnetocrystalline anisotropy at nanoscale: The case of FePt", Applied Physics Letters **100**, 142405 (2012).

[65] M. M. Soares, H. C. N. Tolentino, M. De Santis, A. Y. Ramos, and J. C. Cezar, "Highly anisotropic epitaxial L10 FePt on Pt(001)", Journal of Applied Physics **109**, 07D725 (2011).

[66] S. Imada, A. Yamasaki, S. Suga, T. Shima, and K. Takanashi, "Perpendicular magnetization of L10-ordered FePt films in the thinnest limit", Applied Physics Letters **90**, 132507 (2007).

[67] See `http://www.flapw.de`.

[68] L. Zhong, M. Kim, X. Wang, and A. J. Freeman, "Overlayer-induced anomalous interface magnetocrystalline anisotropy in ultrathin Co films", Phys. Rev. B **53**, 9770–9775 (1996).

[69] C. Carbone, P. Moras, P. M. Sheverdyaeva, D. Pacilé, M. Papagno, L. Ferrari, D. Topwal, E. Vescovo, G. Bihlmayer, F. Freimuth, Y. Mokrousov, and S. Blügel, "Asymmetric band gaps in a Rashba film system", Phys. Rev. B **93**, 125409 (2016).

[70] C. R. Ast, J. Henk, A. Ernst, L. Moreschini, M. C. Falub, D. Pacilé, P. Bruno, K. Kern, and M. Grioni, "Giant Spin Splitting through Surface Alloying", Phys. Rev. Lett. **98**, 186807 (2007).

[71] M. B. Jungfleisch, W. Zhang, J. Sklenar, W. Jiang, J. E. Pearson, J. B. Ketterson, and A. Hoffmann, "Interface-driven spin-torque ferromagnetic resonance by Rashba coupling at the interface between nonmagnetic materials", Phys. Rev. B **93**, 224419 (2016).

[72] J. Železný, H. Gao, K. Výborný, J. Zemen, J. Ma šek, A. Manchon, J. Wunderlich, J. Sinova, and T. Jungwirth, "Relativistic Néel-Order Fields Induced by Electrical Current in Antiferromagnets", Phys. Rev. Lett. **113**, 157201 (2014).

List of Publications

[B1] G. Géranton, F. Freimuth, S. Blügel, and Y. Mokrousov, "Spin-orbit torques in $L1_0$ – FePt/Pt thin films driven by electrical and thermal currents", Phys. Rev. B **91**, 014417 (2015).

[B2] G. Géranton, B. Zimmermann, N. H. Long, P. Mavropoulos, S. Blügel, F. Freimuth, and Y. Mokrousov, "Spin-orbit torques and spin accumulation in FePt/Pt and Co/Cu thin films from first principles: The role of impurities", Phys. Rev. B **93**, 224420 (2016).

List of Figures

2.1. Illustration of the STT, SHE-SOT and Rashba SOT 18
2.2. Band structure and Fermi surface of the Rashba Hamiltonian 21

3.1. Flowchart of the parallelized WANNIER90 programm 38
3.2. Benchmark of the parallelized WANNIER90 code for a film calculation with 23 atoms per unit cell 39

4.1. Illustration of the Voronoi construction and system of coordinates used in the KKR formalism 46

5.1. Illustration of 2 layers of $L1_0$-FePt oriented along the [001]-direction and terminated with Fe atoms (Fe/Pt/Fe/Pt/Fe) deposited on Pt(001) 68
5.2. Even and odd torkances in $L1_0$-$FePt^2/Pt^N$ as a function of disorder strength 70
5.3. Even and odd torkances as a function of the Fermi energy in $L1_0$-FePt/Pt thin films 71
5.4. Band structures of $L1_0$-$FePt^2/Pt^6$ and $L1_0$-$FePt^2/Pt^{18}$ thin films . . . 72
5.5. Even and odd thermal torkances as a function of the Fermi energy in $L1_0$-FePt/Pt thin films 74
5.6. Zero-temperature response coefficients for the torque, the spin accumulation and the spin fluxes in $L1_0$-FePt/Pt 76
5.7. Expectation values of the atom-resolved spin operator for the states at the Fermi surface of FePt/Pt 77
5.8. Expectation values of the atom-resolved torque operator for the states at the Fermi surface of FePt/Pt 77
5.9. Expectation values of the atom-resolved spin flux operator for the states at the Fermi surface of FePt/Pt 78
5.10. Distribution of $\langle \mathcal{T}_x \rangle_{\boldsymbol{k}} \lambda_x(\boldsymbol{k})/|\boldsymbol{v}(\boldsymbol{k})|$ in the Brillouin zone in FePt/Pt film 80
5.11. Distribution of $\langle -\boldsymbol{\sigma}_{y,\mathrm{FePt}} \rangle_{\boldsymbol{k}}\, \lambda_x(\boldsymbol{k})/|\boldsymbol{v}(\boldsymbol{k})|$ in the Brillouin zone in FePt/Pt film 80
5.12. Response coefficients of the spin accumulation and torque for a FePt/Pt film with different types of disorder 82
5.13. Effective fields and total torkance as a function of impurity concentration in FePt/Pt 82
5.14. Illustration of the unit cell of one layer of Co deposited on six layers of Cu(111) 83

5.15. Zero temperature response coefficients for the torque, the spin accumulation and the spin fluxes in Co/Cu 85
5.16. Fermi surface contributions to the torkance in Co/Cu for different impurity types 87
5.17. Distribution of $\langle -\boldsymbol{\sigma}_{y,\mathrm{Co}} \rangle_{\boldsymbol{k}} \, \lambda_x(\boldsymbol{k})/|\boldsymbol{v}(\boldsymbol{k})|$ in the Brillouin zone in Co/Cu film 87
5.18. Room temperature response coefficient of the spin accumulation and torkance in Co/Cu in the presence of Bi, Ir, C and N impurities . . . 88
5.19. Effective magnetic fields and total torkances in Co/Cu as a function of concentrations of Bi, Ir, C and N impurities 89
5.20. Illustration of the unit cell of a Ag_2Bi-terminated Ag(111) film grown on ferromagnetic Fe(110) 90
5.21. Spectral density of states for a Ag_2Bi-terminated Ag film grown on ferromagnetic Fe(110) 93
5.22. Portion of the wave functions located on the Ag_2Bi layer 93
5.23. Torkance at the Fermi surface of a Fe/Ag/Ag_2Bi film 94
5.24. Torkance 930 meV below the Fermi energy in a Fe/Ag/Ag_2Bi film . . 95
5.25. Atom-resolved response tensors for the torque, spin accumulation and spin fluxes in a Ag_2Bi-terminated Ag film grown on ferromagnetic Fe(110). 96
5.26. Illustration of 5 layers of Fe deposited on a Ge(111) film of 12 layers . 98
5.27. States at the Fermi energy marked by the portion of their wave functions on different regions of the Fe/Ge(111) film 99
5.28. Distribution of $\boldsymbol{\mathcal{T}}(\boldsymbol{k})\boldsymbol{\lambda}(\boldsymbol{k})/|\boldsymbol{v}(\boldsymbol{k})|$ in the Brillouin zone in a ferromagnetic Fe/Ge(111) film 101
5.29. Illustration of 5 layers of Fe deposited on a Ge(001) film of 12 layers . 102
5.30. Distribution of $\boldsymbol{\mathcal{T}}(\boldsymbol{k})\boldsymbol{\lambda}(\boldsymbol{k})/|\boldsymbol{v}(\boldsymbol{k})|$ in the Brillouin zone in a ferromagnetic Fe/Ge(001) film 103
5.31. Distribution of $\boldsymbol{\mathcal{T}}(\boldsymbol{k})\boldsymbol{\lambda}(\boldsymbol{k})/|\boldsymbol{v}(\boldsymbol{k})|$ in the Brillouin zone in an antiferromagnetic Fe/Ge(111) film 105

Acknowledgements

First of all I would like to express my sincere gratitude to Prof. Dr. Yuriy Mokrousov for supervising this thesis and for his scientific guidance. It has been an honour and a pleasure for me to conduct my research in your group during these years.

I want to thank Prof. Dr. Stefan Blügel for giving me the opportunity to work at the Peter Grünberg Institute and Institute for Advanced Simulation. I am also very grateful for the many motivating discussions we had during my PhD.

Special thanks to Dr. Frank Freimuth for our countless discussions about spin-orbit torques and physics in general. Your scientific support during these years is priceless.

I want to thank Dr. Nguyen H. Long for sharing his knowledge of the KKR method and for always having an open door for me.

I am very grateful to Dr. Bernd Zimmermann for teaching me the use of the Jülich KKR codes and for the careful proof-reading of the KKR part of this thesis.

I thank Dr. Phivos Mavropoulos for giving me the opportunity to attend his lessons on scattering theory and for sharing with me his profound knowledge of the KKR method.

Thanks to Philipp Rüßmann for the help with Python and many other programming related issues. Thanks also for sharing the rides to Forschungszentrum!

I am grateful to Dr. Ashis Kumar Nandy for sharing with me his expertise in Fe/Ge thin films and for providing the relaxed coordinates of the Fe/Ge(111) bilayers used in this thesis.

I am also deeply indebted to all my colleagues from the Peter Grünberg Institute for their help and support. I would like to mention a few specifically: Julen Ibanez Azpiroz for initiating me to *Euskal kultura* and for his good and timely advices; Juba Bouaziz for his help with personal issues; Marta Gibertini for the positive atmosphere she spreads around her; Ute Winklers for her priceless support regarding administrative issues.

Band / Volume 128
Self-purifying $La_{2/3}Sr_{1/3}MnO_3$ epitaxial films: Observation of surface precipitation of Mn_3O_4 particles for excess Mn ratios
A. Steffen (2016), 154 pp
ISBN: 978-3-95806-162-0

Band / Volume 129
Strain and electric field mediated manipulation of magnetism in $La_{(1-x)}Sr_xMnO_3/BaTiO_3$ heterostructures
M. Schmitz (2016), VI, 141 pp
ISBN: 978-3-95806-164-4

Band / Volume 130
High-Throughput Live-Cell Imaging for Investigations of Cellular Heterogeneity in *Corynebacterium glutamicum*
S. Helfrich (2016), xvi, 217 pp
ISBN: 978-3-95806-167-5

Band / Volume 131
Laser-Induced Ultrafast Electron- and Spin-Dynamics in the Electronic Band Structure of Co(001)
M. A. Plötzing (2016), ii, 109, XXXIV pp
ISBN: 978-3-95806-168-2

Band / Volume 132
Robot-Assisted Phenotyping of Genome-Reduced *Corynebacterium glutamicum* Strain Libraries to Draft a Chassis Organism
S. Unthan (2016), 122 pp
ISBN: 978-3-95806-169-9

Band / Volume 133
Characterization of amino acid ammonia lyases & aminomutases for the production of chiral α- and β-amino acids
A. Dreßen (2016), ix, 112 pp
ISBN: 978-3-95806-176-7

Band/Volume 134
7th Georgian-German School and Workshop in Basic Science
Kacharava, A. (Ed.) erscheint nur als CD (2016)
ISBN 978-3-95806-179-8

Band / Volume 135
Crystal growth and scattering studies on two ferrites
S. Adiga (2016), iv, 150 pp
ISBN: 978-3-95806-183-5

Band / Volume 136
Manipulating the Structural and Electronic Properties of Epitaxial $NaNbO_3$ Films via Strain and Stoichiometry
B. Cai (2016), VI, 114 pp
ISBN: 978-3-95806-185-9

Band / Volume 137
Surface Potential of Metallic Surfaces and Self-Assembling Organic Monolayers in Various Electrolytes
J. Wang (2016), ii, 58 pp
ISBN: 978-3-95806-188-0

Band / Volume 138
Ab initio investigation of hybrid molecular-metallic interfaces as a tool to design surface magnetic properties for molecular spintronics
R. Friedrich (2016), 277 pp
ISBN: 978-3-95806-194-1

Band / Volume 139
Topological Matter – Topological Insulators, Skyrmions and Majoranas
Lecture Notes of the 48th IFF Spring School 2017
27 March – 07 April 2017, Jülich, Germany
ed. by S. Blügel, Y. Mokrousov, T. Schäpers, Y. Ando (2017), ca 1000 pp
ISBN: 978-3-95806-202-3

Band / Volume 140
In situ studies of the growth and oxidation of complex metal oxides by pulsed laser deposition
C. Xu (2017), iv, 159 pp
ISBN: 978-3-95806-204-7

Band / Volume 141
Intrinsic and extrinsic spin-orbit torques from first principles
G. Géranton (2017), 122 pp
ISBN: 978-3-95806-213-9

Weitere ***Schriften des Verlags im Forschungszentrum Jülich*** unter
http://wwwzb1.fz-juelich.de/verlagextern1/index.asp

Schlüsseltechnologien/
Key Technologies
Band/Volume 141
ISBN 978-3-95806-213-9

JÜLICH
FORSCHUNGSZENTRUM